uOttawa

L'Université canadienne
Canada's university

FACULTÉ DES ÉTUDES SUPÉRIEURES ET POSTOCTORALES

uOttawa

L'Université canadienne
Canada's university

FACULTY OF GRADUATE AND POSDOCTORAL STUDIES

Laura Allison Giroux

AUTEUR DE LA THÈSE / AUTHOR OF THESIS

M.Sc. (Earth Sciences)

GRADE / DEGREE

Department of Earth Sciences

FACULTÉ, ÉCOLE, DÉPARTEMENT / FACULTY, SCHOOL, DEPARTMENT

Magnetic Subfabrics of the Whistle Offset Dyke and Embayment, Sudbury Impact Structure, Sudbury, Ontario

TITRE DE LA THÈSE / TITLE OF THESIS

Keith Benn

DIRECTEUR (DIRECTRICE) DE LA THÈSE / THESIS SUPERVISOR

CO-DIRECTEUR (CO-DIRECTRICE) DE LA THÈSE / THESIS CO-SUPERVISOR

EXAMINATEURS (EXAMINATRICES) DE LA THÈSE / THESIS EXAMINERS

A. Flower

C. Samson

Gary W. Slater

LE DOYEN DE LA FACULTÉ DES ÉTUDES SUPÉRIEURES ET POSTDOCTORALES /
DEAN OF THE FACULTY OF GRADUATE AND POSTDOCORAL STUDIES

# MAGNETIC SUBFABRICS OF THE WHISTLE OFFSET DYKE AND EMBAYMENT, SUDBURY IMPACT STRUCTURE, SUDBURY, ONTARIO

By
LAURA ALLISON GIROUX

Thesis submitted to the
Faculty of Graduate & Postdoctoral Studies
In partial fulfillment of the requirements for the
M.Sc. degree in the Earth Sciences

OTTAWA-CARLETON GEOSCIENCE CENTRE
AND
UNIVERSITY OF OTTAWA
OTTAWA, CANADA

*Your file Votre référence*
*ISBN: 0-494-11281-6*
*Our file Notre référence*
*ISBN: 0-494-11281-6*

**Acknowledgements**

I would like to thank Dr. Keith Benn for his supervision and support of the research. Many thanks are also extended to FNX Mining Company Inc. and INCO Ltd. for access to their properties on the Whistle Offset dyke, and for providing paper maps and the required safety training. Gordon Morrison and Judd Fee are thanked for their introduction to the Norman property. Richard Ernst and Ken Buchan of the Geological Survey of Canada are thanked for their lessons in thermal demagnetization. Lewis Ling and Peter Jones at Carleton University are thanked for their instruction and guidance in the use of the scanning electron microscope. I would also like to acknowledge Dr. Keiko Hattori for allowing me access to her microscope and use of her digital camera for the reflected light photomicrographs. The research was supported by Discovery and Equipment grants awarded to Keith Benn by the Natural Sciences and Engineering Research Council of Canada.

**Abstract**

Quartz-diorite Offset dykes from the 1850 Ma Sudbury Impact Structure stem from the Sudbury Igneous Complex (SIC) and extend into the footwall rocks in radial and concentric patterns with respect to the SIC. The dykes formed by emplacement of magma derived from the impact melt body into radial and concentric fractures generated in the country rock by the hypervelocity meteorite impact. The NE-striking Whistle Offset dyke extends from the northeast corner of the SIC, and is connected to the SIC by the Whistle embayment structure. A suite of oriented specimens was collected from 20 sites in the Whistle Offset dyke and the embayment, in order to determine the emplacement flow pattern within the dyke, the embayment, and the hosted massive sulfide deposits. The emplacement flow pattern was studied by using magnetic anisotropy measurements in order to infer the petrofabrics, and the subfabrics, defined by different mineral populations. The magnetic anisotropy methods included the anisotropy of magnetic susceptibility (AMS), the anisotropy of anhysteretic remanence (AAR) and the anisotropy of partial anhysteretic remanence (ApAR). The complex magnetic mineralogy of the sample suite was examined using measurements of partial anhystertic remanence (pAR) acquisition, alternating-field demagnetization and thermal demagnetization, in addition to petrographic and scanning electron microscope (SEM) studies. The subfabrics which are interpreted to record the flow pattern in the Whistle Offset dyke, are defined by low coercivity coarse-grained magnetite, interpreted to be of primary igneous origin. The fabrics are suggestive of lateral (horizontal) injection of the magma and subsequent sinking of molten massive sulfide bodies through the still unsolidified dyke. Sinking of the massive sulfides is recorded by moderately plunging to vertical magnetic lineations. Steeply plunging lineations elsewhere in the Offset dykes may also indicate the presence of sunken massive sulfides in the subsurface.

**Résumé**

Les filons de quartz-diorite de la Structure d'impact de Sudbury, datant de 1850 Ma, s'étendent du Complexe igné de Sudbury (CIS) aux roches de l'éponte inférieure de manière concentrique et radiale. Les filons étaitent injectées, comme magma, en fractures verticales engendrées par l'impact aérolithique dans la roche-mère. La filon Whistle s'étend du nord-est coin du CIS et est jointe au CIS par le Whistle 'embayment'. L'anisotropie de la susceptibilité magnétique (AMS), l'anisotopie anhystérétique de la rémanence (AAR) et l'anisotopie anhystérétique partielle de la rémanence (ApAR) magnétique étaitent utilisées comme méthodes d'acquisition de la pétrofabrication des roches pour comprendre les mécanismes d'emplacement des filons et des dépôts de sulfure massif. La minéralogie complexe des roches était examinée avec les mesures de l'acquisition anhystérétique partielle de la rémanence, le désaimantation anhystérétique de la rémanence, la désaimantation thermalle, la pétrographie, et le SEM. Les linéations et foliations magnétiques qui donnent la direction d'écoulement igné sont contôlées par les gros grains de magnétite primaire. L'extrapolation des resultats indique que l'écoulement igné était horizontal du sud-ouest au nord-est. La plongée escarpée des linéations de magnétite dans les dépôts de sulfure massif indique l'affaissement du sulfure massif dans les roches des filons.

Table of Contents

List of Tables

List of Figures

List of Acronyms Used

AAR – anisotropy of anhysteretic remanence
AF – alternating field
AR – anhysteretic remanence
AMS – anisotropy of magnetic susceptibility
ApAR – anisotropy of partial anhysteretic remanence
DF – direct field
GSC – Geological Survey of Canada
MD – multi domain
pAR – partial anhysteretic remanence
PDF – planar deformation features
PGE – platinum group element
SD – single domain
SEM – scanning electron microscope
SIC – Sudbury Igneous Complex

## Chapter 1: Introduction

The 1850 ± 3 Ma (Krogh, et al., 1984) Sudbury Impact Structure, located in northern Ontario, is one of the largest and best preserved terrestrial impact structures. The Sudbury Impact Structure is also one of the largest Ni-Cu-PGE mining camps in the world. The magmatic and hydrothermal systems of the Sudbury Igneous Complex (SIC) and the related Offset dykes have been continuously exploited for well over a century and continue to be the main focus of mineral exploration and exploitation. The Offset dykes (Coleman, 1903) are radial and concentric quartz diorite dykes that stem from embayment structures in the SIC, and are thought to have been emplaced as a partially molten melt-crystal suspension into fractures generated in the country rock by the hypervelocity impact (Grant and Bite, 1984). The locations of the principal Offset dykes are indicated in Fig. 2.1.

Studies of the emplacement of the Offset dykes are of interest in furthering our understanding of the cratering processes that occurred during the formation of the Sudbury Impact Structure. Such studies may also lead to a better understanding of the origin of the economically important Ni-Cu-PGE (platinum group element) deposits. The origin of the Ni-Cu-PGE deposits, which are hosted by the Offset dykes, remains somewhat controversial (Pattison, 1979; Grant and Bite, 1984; Lightfoot and Farrow, 2002).

The emplacement of the Offset dykes is investigated in this study through the use of magnetic anisotropy measurements on oriented samples. The measurements allow documentation and interpretation of the mineral preferred orientations (i.e. fabrics) in the dykes. In a previous study of the Copper Cliff Offset dyke (Fig. 2.1) the anisotropy of magnetic susceptibility (AMS) fabrics of the quartz diorite were measured, shedding new light on the evolution of the impact crater during its formation. The study led to the

reinterpretation of the Copper Cliff Offset as a melt filled transfer fault that accommodated displacements during the crater modification stage collapse of the crater rim walls (Scott and Benn, 2001; 2002).

The aim of this study is to attain a better understanding of the emplacement of the quartz diorite Offset dykes and their hosted massive sulfide deposits by focusing on the magnetic anisotropy fabrics of the Whistle Offset dyke. The Whistle Offset is located within Norman Township, approximately 30-km north-northeast of Sudbury. It stems radially from the northeast corner of the SIC (Fig. 2.1). The principal lithologies that make up the Whistle Offset dyke were sampled. The lithologies include leucocratic breccia (a quartz dioritic matrix with mafic and granitic inclusions), inclusion-free amphibole-quartz diorite and massive sulfide. Norite from the embayment, that physically links the Whistle Offset dyke to the Sudbury Impact Structure, was also sampled. Petrographic and SEM investigations show that the paramagnetic and ferromagnetic mineralogy of the samples is complex, in part due to a greenschist-grade static metamorphic overprint. Evidence is also documented for replacement of magnetite crystals by later sulfide minerals, within sulfide-rich breccias and massive sulfides.

Three magnetic anisotropy methods were employed in an attempt to isolate the primary magnetic fabric of the Whistle Offset dyke, i.e. the fabric that is interpreted to record flow during its emplacement. The anisotropy of magnetic susceptibility (AMS), the anisotropy of anhysteretic remanence (AAR) and the partial AAR (ApAR) were all measured for the sample suite in order to determine the preferred orientations of different mineral populations, in samples collected from 20 sites within the dyke and the embayment. Fabric results are used to interpret flow patterns within the dyke and the mechanism by which the dyke, and the massive sulfide bodies it hosts, were emplaced.

*1.1. Goals and methods*

The primary goal of this study is to isolate magnetic anisotropy fabrics for the Whistle Offset dyke that can be interpreted to represent primary petrofabrics, that is, the mineral preferred orientations that formed during emplacement of the Whistle Offset dyke and of the hosted massive sulfide ores. The magnetic mineralogy in the sample suite was studied using a scanning electron microscope (SEM) as well as both reflected and incident light microscopy, as documentation of the ore minerals and their textures was a secondary goal. The complexity of the magnetic mineralogy, which is partly due to a greenschist-grade static metamorphic overprint, led to the investigation of the magnetic subfabric of coarse-grained magnetites and titanomagnetites. The coarse-grained Fe-oxides are interpreted to represent a primary mineral fraction that was in suspension within the impact melts during emplacement of the embayment and the Offset dyke. The fabric of Fe-oxides therefore provides information on flow during emplacement.

Demagnetization (both thermal and alternating field (AF)) and acquisition of anhysteretic remanence were used to identify samples that contain a hard coercivity fraction of ferromagnetic minerals, made up of fine-grained magnetite and titanomagnetite of probable metamorphic origin, plus pyrrhotite and hematite. The anisotropy of magnetic susceptibility (AMS), the anisotropy of anhysteretic remanence (AAR) and the anisotropy of partial AR (ApAR) were all measured for the sample suite. Consideration of the three different anisotropies and of the AR demagnetization and acquisition data shows that where the hard magnetic fraction is absent or not abundant, the AMS provides the most efficient method for measuring the magnetic subfabric of the soft fraction of coarse grained magnetite. Where the hard fraction is present, the ApAR was used to isolate the magnetic subfabric of the low coercivity, coarse-grained magnetite fraction.

The AMS and ApAR measurements allowed the preserved coarse-grained magnetite and titanomagnetite subfabric pattern to be mapped, permitting interpretation of the flow pattern during dyke and sulfide emplacement. The interpretations of the derived flow pattern are mainly consistent with an emplacement model that was previously inferred from detailed lithological mapping (Lightfoot, et al., 1997; Murphy and Spray, 2002). The magnetic fabric maps show lateral flow during emplacement of the Whistle Offset dyke, followed by foundering and sinking of the high density massive sulfides, prior to the final freezing of the host noritic and quartz dioritic rocks. Steeply plunging magnetic lineations associated with sinking of the massive sulfides may provide useful indications of other ore bodies in the subsurface. Well-defined magnetic lineations in the cumulate-textured norites of the embayment may also indicate emplacement flow, or possibly gravity slumping of the unconsolidated cumulates.

The results of this study demonstrate that a map of the emplacement flow fabrics can be constructed by employing multiple magnetic anisotropy methods that isolate subfabrics defined by different populations of minerals. In particular, this allows for the isolation of the subfabric of the coarse-grained magnetite and titanomagnetite crystals in several rock types that have been subjected to static greenschist-grade metamorphism. The resulting subfabric maps are interpreted in terms of emplacement flow of the Whistle Offset dyke. Combined with petrographic and SEM observations, measured magnetic anisotropies were also used to infer possible origins for the massive sulfide mineralization.

### *1.2. Structure of the Thesis*

The reader will first be introduced to the geological setting, including a description of the Sudbury Impact Structure and the related quartz diorite Offset dykes. A more detailed

description is provided of the Whistle Offset dyke and embayment, the field area for this study. The results of incident and reflected light petrographic studies are discussed in terms of the different rock types that make up the Whistle Offset dyke and the embayment, which physically connects the Offset dyke to the Sudbury Igneous Complex. The opaque mineralogy of the different rock types is further documented and discussed with reference to the SEM study. The methods employed for the anisotropy of magnetic susceptibility (AMS), anisotropy of anhysteretic remanence (AAR) magnetization and anisotropy of partial anhysteretic remanence (ApAR) magnetization measurements is then described including the fundamental differences between the techniques. The alternating field demagnetization, partial anhysteretic remanence (pAR) acquisition and the thermal demagnetization techniques, which were employed to test the magnetic responses of the rocks, are also explained. The results are first presented in terms of the magnetic responses of the sample suite. The magnetic fabric results of the AMS, AAR and ApAR techniques are then presented and compared in the context of the magnetic response tests. In the discussion, the sources of the AMS, AAR and ApAR will be discussed in detail as well as the significance of the results to the interpretation and development of an emplacement model. The results and interpretations presented in the thesis have also been submitted to a refereed journal for review.

## Chapter 2: Geological Setting

### *2.1. Sudbury Impact Structure*

The 1850 ± 3 Ma (Krogh, et al., 1984) Sudbury Impact Structure is one of the largest preserved meteorite impact sites identified on Earth. The multi-ring meteorite impact structure is located at 81° 11'W, 46° 36'N, on the boundary between the Superior and Southern tectonic provinces of the Canadian Shield, in northern Ontario (Fig. 2.1). The Superior Province rocks consist of greenstones, granitoids, and gneiss of Late Archean ages. The Southern Province rocks consist of Early Proterozoic metavolcanic and metasedimentary formations belonging to the Huronian Supergroup. Impact target rocks also include the 2.3 Ga quartz monzonite Creighton and Murray Plutons to the south of the structure and 2.15 Ga intrusive Nipissing metagabbro and diabase rocks which form sills emplaced within the southern Superior Province.

The apparent centre of the impact structure is the approximately 30 x 60 km Sudbury Igneous Complex (SIC) (Fig. 2.1). The SIC is interpreted as a differentiated crystallized impact melt body, originally sheet-like (Grieve et al., 1991; Deutsch et al., 1995; Therriault et al., 2002) or funnel shaped (Cowan, 1999) in three dimensions, derived from Precambrian crustal target rocks and possibly from the underlying mantle (Grieve et al., 1991). The SIC consists of four main units. From the bottom to top they are the basal contact sublayer represented by a mineralized xenolith-bearing norite, an overlying mafic and felsic norite unit, a quartz-gabbro unit, and an upper granophyre unit (Naldrett and Hewins, 1984). The Whitewater Group, which includes impact fallback breccia and overlying argillite and siltstone, rests upon the SIC (Fig. 2.1). The outer zone around the SIC consists of fractured,

**Figure 2.1.** Geological map of the Sudbury Impact Structure showing locations of the principal Offset dykes. Modified after Scott and Benn (2001).

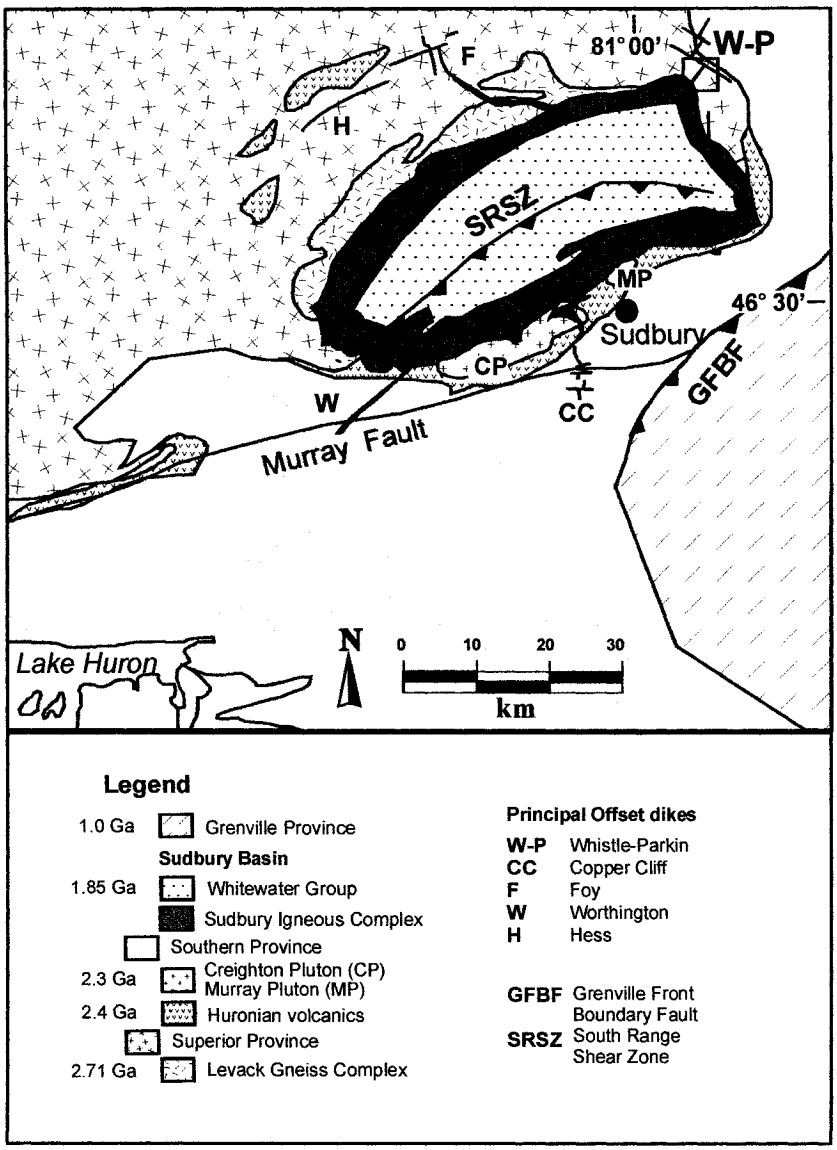
81° 00'
W-P
F
H
SRSZ
MP
46° 30'
Sudbury
CP
CC
GFBF
W
Murray Fault
Lake Huron
N
0
10
20
30
km
Legend
1.0 Ga
Grenville Province
Sudbury Basin
1.85 Ga
Whitewater Group
Sudbury Igneous Complex
Southern Province
2.3 Ga
Creighton Pluton (CP)
Murray Pluton (MP)
2.4 Ga
Huronian volcanics
Superior Province
2.71 Ga
Levack Gneiss Complex
Principal Offset dikes
W-P Whistle-Parkin
CC Copper Cliff
F Foy
W Worthington
H Hess
GFBF Grenville Front Boundary Fault
SRSZ South Range Shear Zone

Fig. 2.1

locally brecciated and partially melted footwall rocks which were deformed by the shock of the impact.

Associated with the magmatic and hydrothermal systems of the SIC are the quartz diorite Offset dykes. The Offset dykes stem mostly radially from embayment structures, which are connected to the SIC, and less commonly are found concentric to the SIC. The locations of the principal Offset dykes are indicated in Fig. 2.1.

The current elliptical shape of the structure is attributed to northwesterly vergent thrusting during the Penokean orogenic event which resulted in the northwest-southeast shortening of the SIC and Sudbury Basin (Boerner et al., 2000). Metamorphism in the Sudbury area appears to postdate the emplacement of the 1.85 Ga SIC but it is unknown if the deformation is related to the early-stage (1870-1820 Ma) or the late-stage (1740-1700 Ma) events of the Penokean Orogeny. The Penokean event also resulted in the South Range shear zone (SRSZ in Fig. 2.1). To the southeast of the Grenville Front Boundary Fault (Fig. 2.1), further overprinting and obliteration of impact features occurred during the Grenville orogeny (~1.0 Ga). The original diameter of the Sudbury Impact Structure is thought to have been 200 to 280 km (Grieve et al., 1991; Butler, 1994; Deutsch et al., 1995).

Mineralization in the Sudbury structure consists typically of pyrrhotite, pentlandite, chalcopyrite, pyrite and titanium-poor magnetite. Economic sulfide mineralization occurs in three main settings: the sublayer, the footwall rocks and the Offset dykes. Individual ore deposits within the (up to 100-meter thick) sublayer are commonly zoned with copper/nickel ratios are usually being lowest in the sublayer and increasing outwards into the footwall rocks. Footwall deposits occur as zones of sulfide mineralization in the form of stringers, veins, massive sheets and/or disseminated sulfides. The deposits are thought to have formed from sulfide-rich melts that migrated from the base of the sublayer into the footwall rocks

(Dressler, 1984). Hydrothermal processes in the footwall may have led to later remobilization of some metals within the deposits (Farrow and Watkinson, 1997). Mineralization of the Offset dyke deposits occurs as disseminated to massive sulfides. Massive sulfide bodies are often found along the contacts of the dykes and are often rimmed by a halo of disseminated sulfides (Dressler, 1984).

*2.2. The Sudbury Structure as an impact crater*

Impact craters are classified as either simple or complex based on their morphology and associated structures. Simple craters (Fig. 2.2a) are smaller craters (< 4-km diameter on Earth) with a raised circular rim and a near-parabolic profile. The interior slope of the crater is steepest near the rim and decreases smoothly towards the centre. The crater is partially filled by a breccia lens; allocthonous material exhibiting some shock metamorphism (Pilkington and Grieve, 1992).

Complex craters are much larger (> 10-20 km diameter on the moon's surface and > 4-km on Earth), but have a shallower depth to diameter ratio than simple craters. Complex crater formation involves an initial downward displacement and excavation of the target rocks as a transient crater is formed. Subsequent rebounding of the cavity floor produces a central structural uplift (SU) or central peak. Crater modification continues as the transient cavity rim collapses resulting in the development of shallower structures, compared to simple craters, with a faulted rim zone and flat floor (Fig. 2.2b). The highly shocked breccia and impact melts that did not escape during the collapse cover the flat crater floor (Pilkington and Grieve, 1992).

Multi-ringed basins are a specific type of complex crater. The multiring basins represent the largest craters identified on the moon and are characterized by the development

**Figure 2.2.** Schematic cross-sections of impact structures. **(2.2A)** A simple crater. D = diameter of the crater, da = apparent depth, dt = true depth of crater. Adapted from Pilkington and Grieve 1992). **(2.2B)** A complex crater. SU = amount of structural uplift. Adapted from Pilkington and Grieve (1992). **(2.2C)** The Sudbury Structure immediately after formation. Adapted from Grieve et al. (1991).

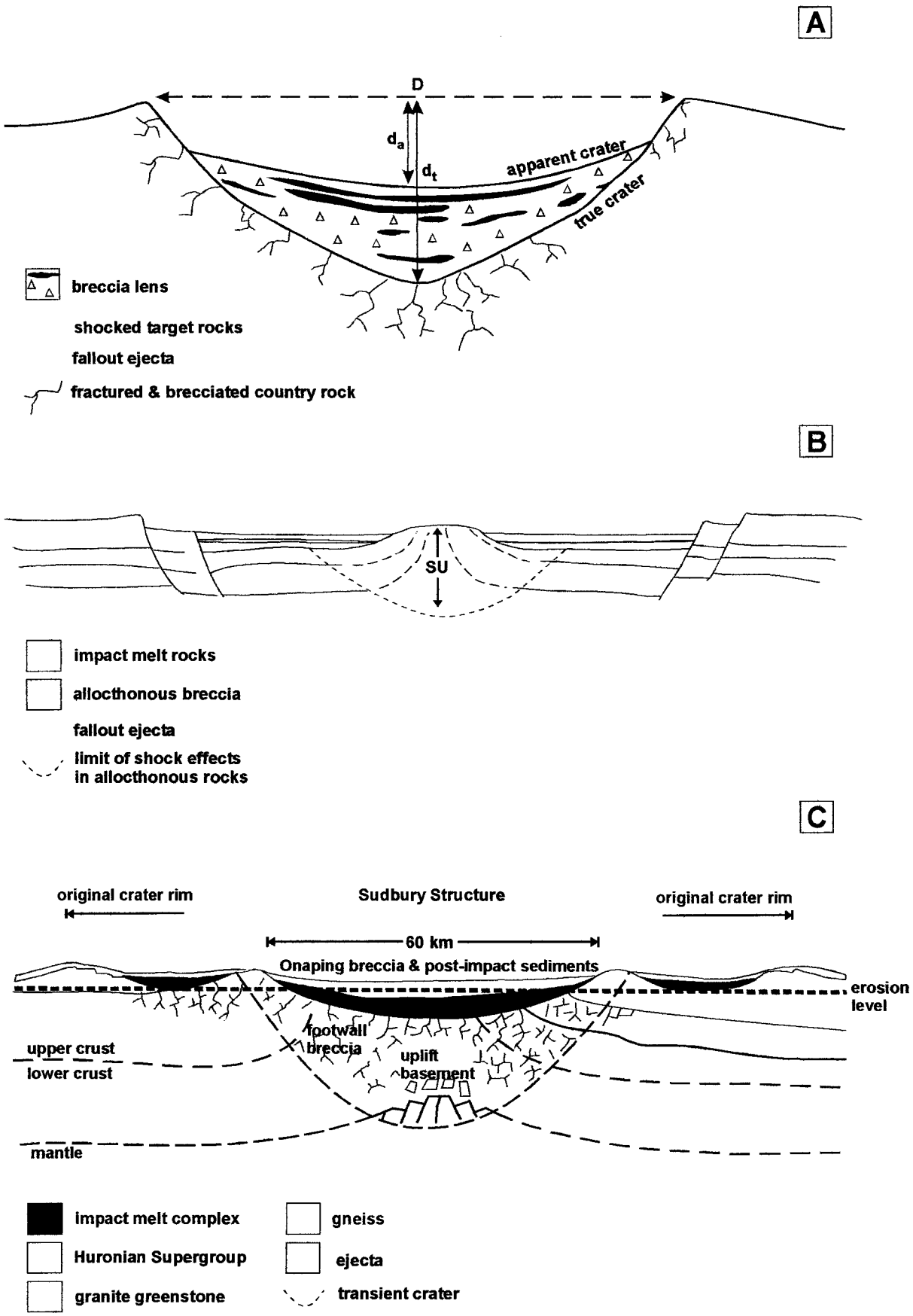
A
D
$d_a$
$d_t$
apparent crater
true crater
breccia lens
shocked target rocks
fallout ejecta
fractured & brecciated country rock
B
SU
impact melt rocks
allocthonous breccia
fallout ejecta
limit of shock effects
in allocthonous rocks
C
original crater rim
Sudbury Structure
original crater rim
60 km
Onaping breccia & post-impact sediments
erosion
level
footwall
breccia
uplift
basement
upper crust
lower crust
mantle
impact melt complex
Huronian Supergroup
granite greenstone
gneiss
ejecta
transient crater

Fig. 2.2

of one or more 'annular' rings beyond the primary crater rim (Melosh, 1989). Multi-ringed basins on Earth have been identified based on their size and not the presence of annular rings, as any definitive annular ring escarpments have been removed by erosion.

Dietz (1964) was the first to suggest an impact origin for the Sudbury structure, likening the SIC to a lunar mare basin. Evidence for and acceptance of an impact origin grew with the subsequent discovery of shatter cones (Guy-Bray and Staff, 1966) and planar deformation features (PDFs) in the Onaping Formation (French, 1967), and in the North Range of the SIC (Dressler, 1984). More recently impact diamonds where identified in breccias of the Onaping Formation (Masaitis et al., 2000). Finally, a kinematic reconstruction of the pre-deformation shape of the currently oval-shaped Sudbury structure by Roest and Pilkington (1994) showed that it could have originally had the circular shape of an impact structure.

The Sudbury structure is considered to be at least a two-ring multi-ring impact basin (Fig. 2.2c) (Grieve et al., 1991). Multi-ring basins in impact craters as large as Sudbury consist of a central-peak rim that surrounds the melt sheet and an annular melt sheet past the peak-rim (Grieve et al., 1991). There is no remaining evidence of the central-peak in the Sudbury structure. This is likely due to several kilometers of erosion during and following the Penokean Orogeny, which may have also removed an annular melt sheet as well as any topographic expression of the central-peak rim (Grieve et al., 1991).

The classification of the Sudbury structure as a multi-ring basin is based primarily on the size of the structure. The formation of shatter cones at 20 km beyond the outer limit of the SIC suggests that the transient cavity is greater than 100 km in diameter (Pilkington and Grieve, 1992). Although most evidence of rings would have been obliterated during post-impact tectonism, Spray and Thompson (1995) identified sub-concentric zones of intense

pseudotachylyte development to the north of the SIC. These concentrated subconcentric zones may be related to the development of ring faults, or 'superfaults' (Spray, 1997), in the target rocks during modification of the multi-ring basin (Thompson and Spray, 1996; Scott and Spray, 1999).

*2.3. Quartz Diorite Offset dykes*

Two sets of quartz diorite Offset dykes are documented in the Sudbury Impact Structure. One is a set of radial dykes that stem from the norite and/or sublayer of the SIC and extend into the Archean and Proterozoic footwall rocks. The radial dykes have vertical dips and are linked to the main mass of the SIC through funnel-shaped, sublayer-filled embayment structures. The other set consists of dykes that are concentric, and parallel to the base of the igneous complex; the concentric dykes are not contiguous with the SIC in map view (Fig. 2.1). The dykes are composed mainly of quartz diorite. They were referred to as Offset dykes by Coleman (1903) due to the dykes being subsequently offset along late-stage faults. The term Offset dykes is now widely used in the literature. The twelve documented Offset dykes are classified into three different types: radial (Foy, Whistle-Parkin, Copper Cliff, Worthington, Ministic), concentric (Manchester, Hess, Kirkwood, Frood-Stobie and Vermilion), and discontinuous (Maclennan, Creighton). Five of the principal Offset dykes are shown in Fig. 2.1.

Three main petrographic types of quartz diorite are recognized within the Offsets: orthopyroxene (hypersthene)-, clinopyroxene- and amphibole-biotite- quartz diorites (Grant and Bite, 1984). Amphibole-biotite quartz diorite is the most common type. A marked increase in grain size is common from the margin inwards of quartz diorite pods and dykes (Grant and Bite, 1984).

One interpretation of the origin of the Offset dykes is that they were injected into radial and concentric fractures that were generated in the country rock by the hypervelocity impact (Pattison, 1979; Grant and Bite, 1984). An alternative interpretation is that the Offset dykes represent impact melt that flowed downward from the base of the overlying Sudbury Igneous Complex melt body, into steeply dipping pipes leading into the fractures (Lightfoot et al., 2001; Lightfoot and Farrow, 2002). Recent magnetic anisotropy studies of the Copper Cliff Offset dyke indicate that it acted as a melt-lubricated transfer fault during collapse of the transient cavity (Scott and Benn, 2001; Scott and Benn, 2002). Uranium-lead dating on the Foy Offset suggests contemporaneous formation of the impact melts and the emplacement of the Offset dykes (Ostermann et al., 1996). The average chemical composition of the quartz diorite in most of the Offset dykes is equivalent to the bulk composition of the SIC, indicating that the Offset dykes were emplaced prior to any significant differentiation of the impact melt sheet (Thompson, 1935; Lightfoot and Farrow, 2002). The composition of the Hess Offset, one of the concentric dykes, is closer to the composition of the felsic norite component of the SIC, rather than to the bulk composition of the SIC, indicating that the Hess Offset was emplaced during fractionation of the impact melt sheet (Wood and Spray, 1998).

### *2.4. The Whistle Offset dyke*

The Whistle Offset dyke (Fig. 2.3) is one of the radial Offsets. The dyke is located approximately 30 km north-northeast of Sudbury (Fig. 2.1), in the Norman Township. The Whistle Offset is considered by many researchers to be the first of three principal displaced segments, which make up the Whistle-Parkin Offset dyke (Fig. 2.1). The Whistle Offset dyke extends from the Sudbury Igneous Complex into footwall Archean granitoid rocks. It is

**Figure 2.3.** Detailed geological map of the Whistle embayment and Offset dyke. Modified after Lightfoot et al. (1997).

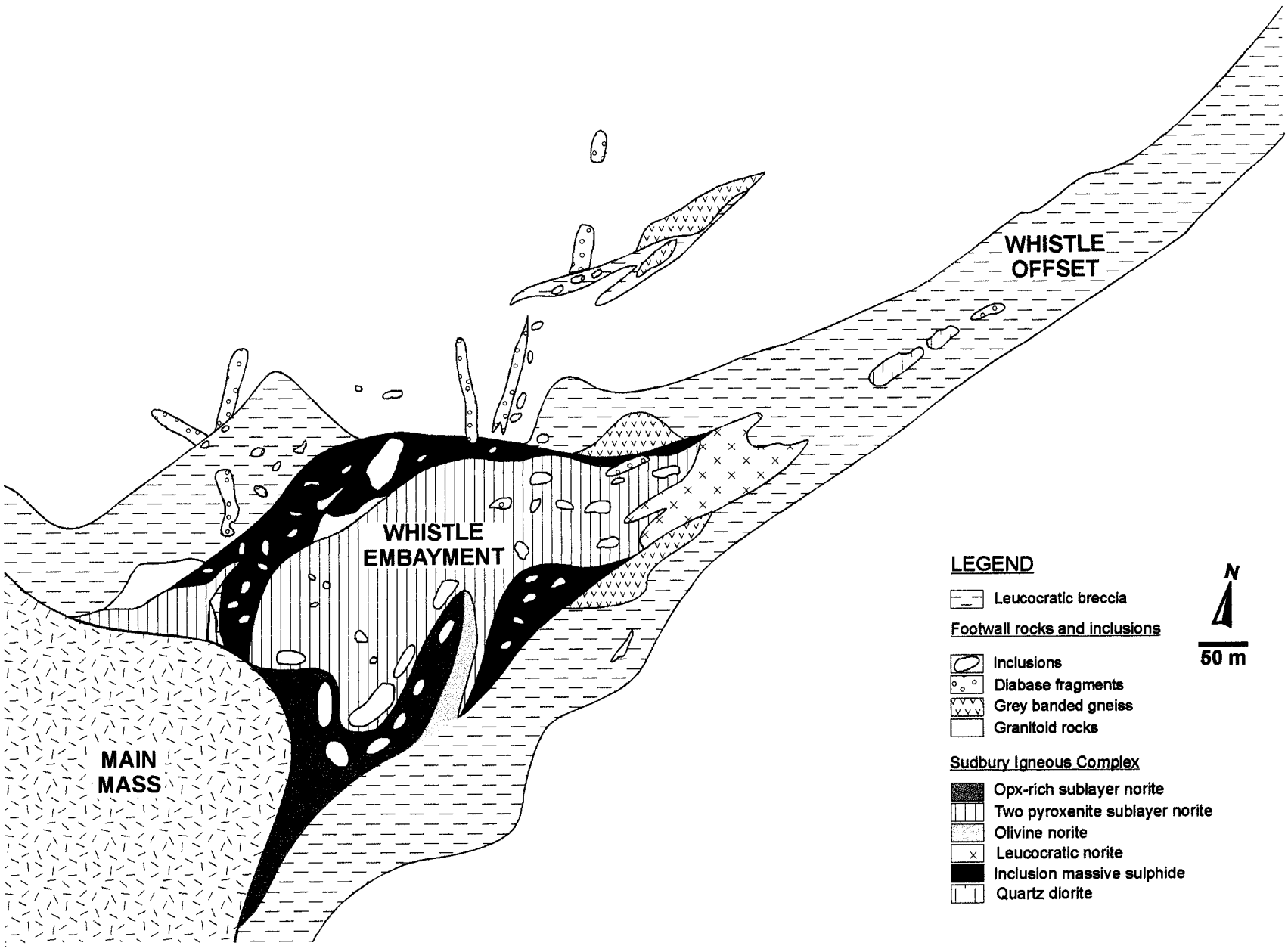
WHISTLE
OFFSET
WHISTLE
EMBAYMENT
MAIN
MASS
LEGEND
Leucocratic breccia
Footwall rocks and inclusions
Inclusions
Diabase fragments
Grey banded gneiss
Granitoid rocks
Sudbury Igneous Complex
Opx-rich sublayer norite
Two pyroxenite sublayer norite
Olivine norite
Leucocratic norite
Inclusion massive sulphide
Quartz diorite
N
50 m

Fig. 2.3

physically connected to the base of the SIC by the Whistle embayment; a 500 x 350-m wide, 1-km thick funnel-shaped norite body (Pattison, 1979; Lightfoot et al., 1997). The embayment then narrows to a width of 30 to 50 m at the transition into the dyke. This transition corresponds with the lateral change from the more mafic two-pyroxene sublayer norite to a more plagioclase-rich leucocratic norite. Where it is most proximal to the embayment, the Whistle Offset dyke is 100 to 150 m wide. More distally, approaching the Post Creek fault zone, it narrows to a width of 15 to 20 m (Fig. 2.3). The Whistle Offset extends for approximately 2 km before being offset from the Parkin Offset by the Post Creek fault zone (PCFZ) (Murphy and Spray, 2002). The PCFZ displaced the Parkin Offset dyke 2-km to the northwest. At approximately 6-km from the SIC, the Parkin dyke is offset by the Milnet Mine fault zone, displacing the dyke approximately 250 m to the northwest.

Pattison (1979) made the only systematic description of the Whistle embayment prior to commencement of mining operations. Pattison's borehole data and pyroxene microprobe analyses along the length of the Whistle embayment and proximal Offset showed an enrichment of iron and silica from the core of the funnel shaped embayment outward.

A more recent geological and geochemical study of the embayment (Lightfoot et al., 1997) showed that the igneous-textured sublayer matrix is geochemically unlike the main mass norites, quartz gabbros and granophyres of the SIC. The authors suggest that the composition of the sublayer could be modelled by a mixture of local country-rock granitoids (~10%), main mass mafic norite (~20%) and diabase (~70%) and suggested a model in which the melting of target rocks produced an initially felsic melt sheet full of mafic fragments. Fragments then sank to the base of the melt sheet in crater, becoming concentrated and partly melted to produce the sublayer. Massive sulfides would have also

accumulated at the base of the overlying melt sheet and, due to their high density, would have sunk into the unsolidified Whistle Offset (Lightfoot et al., 1997).

Murphy and Spray (2002) studied the relationships of, and variations within, different lithologies of the Whistle-Parkin Offset dyke system and proposed a multistage emplacement model beginning with the forceful lateral injection of the clast-bearing rocks into the impact-generated radial fracture. Inclusion-poor quartz diorite and massive sulfides then sank downwards from the overlying melt-sheet during the early crater modification stage. Faulting during late-stage transient cavity collapse then offset the Whistle and Parkin dyke segments.

Contact style mineralization within the Whistle embayment structure supported open pit mining operations from 1988 to 1991 and later from 1994 to 1998. The Whistle Mine, operated by Inco Ltd., produced 5.71 million tons of ore and over 7 million tons of waste rock. The inclusion-rich pyrrhotite ore graded 2 to 3 wt % Ni, >0.2 wt % Cu and <500 ppb Pt + Pd (Lightfoot et al., 1997). Recent exploration by FNX Mining Ltd. has renewed interest in the Norman property and the Whistle Offset. The North deposit, a massive sulfide zone exposure up to 3 m wide assayed at almost 30% Cu, 3% Ni and 30 grams of total precious metals per ton, has been discovered in the distal portion of the Offset dyke known as the North Zone Deposit (FNX 2003).

## Chapter 3: Rock Types and Petrography

Samples were collected at 20 sites on the Norman property, which covers the length of the Whistle Offset. Cores for magnetic measurements were collected at each site using a portable rock drill and oriented with a magnetic compass. Samples from clast-rich rock types were taken with care to sample principally from the rock matrix. The 25-mm diameter cores were each cut into 1 to 5 specimens, each 22-mm long, depending on the length and quality of the core, for a total of 210 specimens. Sample sites are indicated in Figure 3.1.

Three sites were sampled in the Whistle embayment, which links the Whistle Offset dyke to the main mass of the Sudbury Igneous Complex. The samples were taken from the sublayer norite unit. A leucocratic norite unit extends from the two-pyroxene sublayer norite unit of the SIC outwards into the leucocratic breccia of the proximal portion of the Whistle Offset. One leucocratic norite site was sampled as well as six sites in the leucocratic breccia in the most proximal portion of the Whistle Offset to the embayment (Fig. 3.2A). Ten more sites were sampled within the distal portion of the Whistle Offset dyke (Fig. 3.2B), including six sulfide-rich sites from the North Zone deposit, two leucocratic breccia sites, and a mafic norite and an amphibole-quartz diorite site.

Samples show evidence of varying degrees of static greenschist-grade metamorphic overprint. This is most evident as the chloritization of mafic silicate minerals including biotite, amphibole and pyroxene. Chlorite and epidote veins are also present, and the feldspars are variably altered to sericite.

The ability to sample line traverses across the proximal Offset and the embayment was hindered by ongoing reclamation efforts for the non-operational Whistle pit mine, which is located within the Whistle embayment. This meant that parts of the property were

**Figure 3.1.** Sampling locations for the Whistle embayment, the proximal Whistle Offset dyke and the North Zone. Base map provided by FNX Mining Company Ltd.

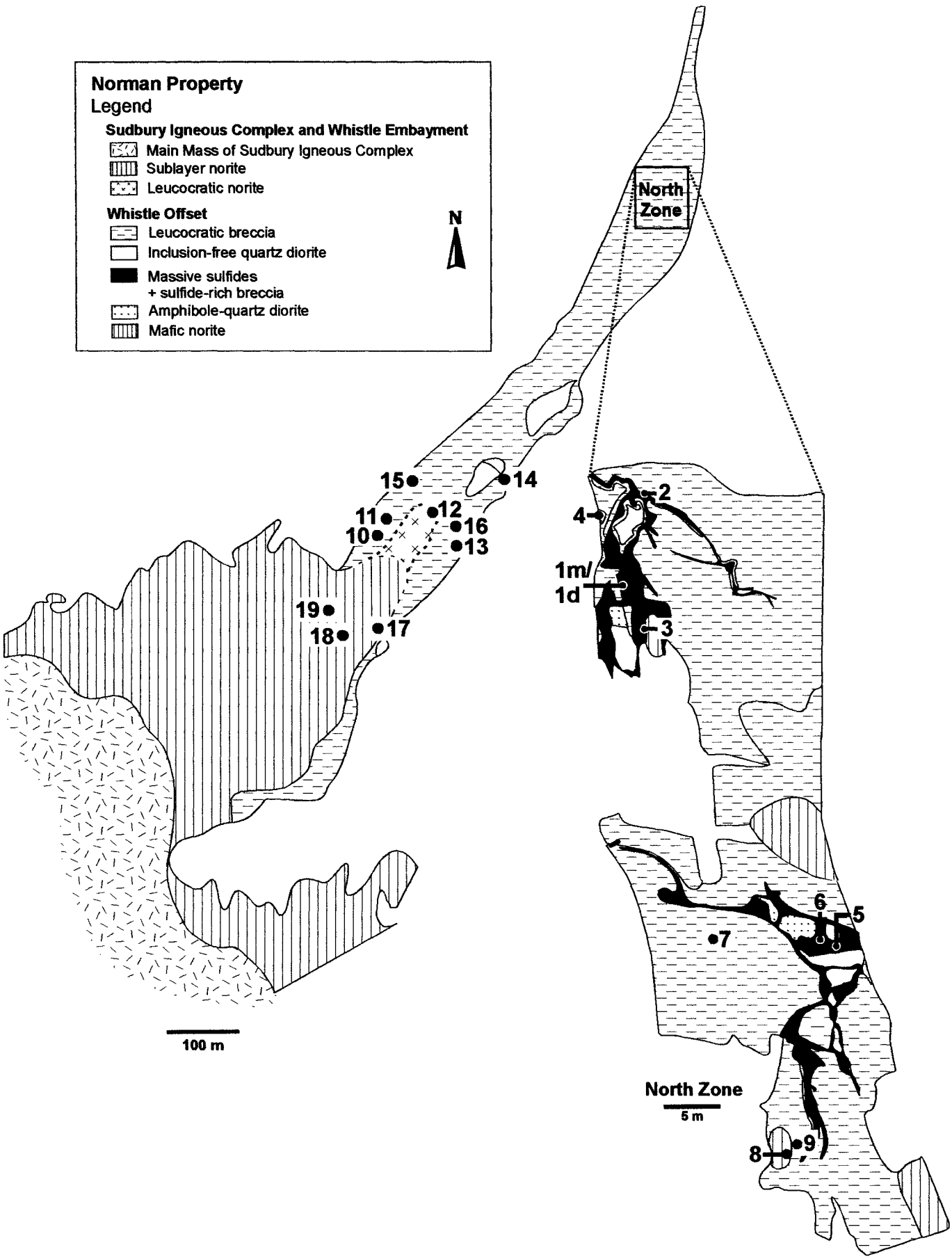
Norman Property
Legend
Sudbury Igneous Complex and Whistle Embayment
Main Mass of Sudbury Igneous Complex
Sublayer norite
Leucocratic norite
Whistle Offset
Leucocratic breccia
Inclusion-free quartz diorite
Massive sulfides
+ sulfide-rich breccia
Amphibole-quartz diorite
Mafic norite
N
North Zone
15
14
11
12
16
10
13
19
18
17
2
4
1m/
1d
3
100 m
6
5
7
North Zone
5 m
8
9

Fig. 3.1.

**Table 3.1.** Mineral and texture abbreviations. List of mineral abbreviations expanded from Kretz (1983).

Table 3.1.
**mineral name abbreviations**

| | |
|---|---|
| Ag-Te | silver telluride |
| Am | amphibole |
| Bi-Pd | bismuth palladium |
| Bi-Te | bismuth telluride |
| Bt | biotite |
| Chl | chlorite |
| Ccp | chalcopyrite |
| Cpx | clinopyroxene |
| Ep | epidote |
| Gn | galena |
| Hbl | hornblende |
| Kfs | potassium feldspar |
| Mag | magnetite |
| Mcn | michenerite |
| Opx | orthopyroxene |
| Pn | Pentlandite |
| Pl | plagioclase |
| Po | pyrrhotite |
| Py | pyrite |
| Qtz | quartz |
| Ti-Mag | titanomagnetite |

**textural term abbreviations**

| | |
|---|---|
| gran | granophyric |
| mic | micrographic |

**Figure 3.2.** Field photos from the Whistle embayment and Whistle Offset dyke. **(3.2A)** Whistle embayment and proximal Offset. **(3.2B)** North Zone of the Whistle Offset (distal Offset). **(3.2C)** Extensive jointing of the leucocratic breccia in the proximal Offset. **(3.2D)** Shear zones at the margins of the Offset dyke. **(3.2E)** A gneissic xenolith in brecciated footwall rocks.

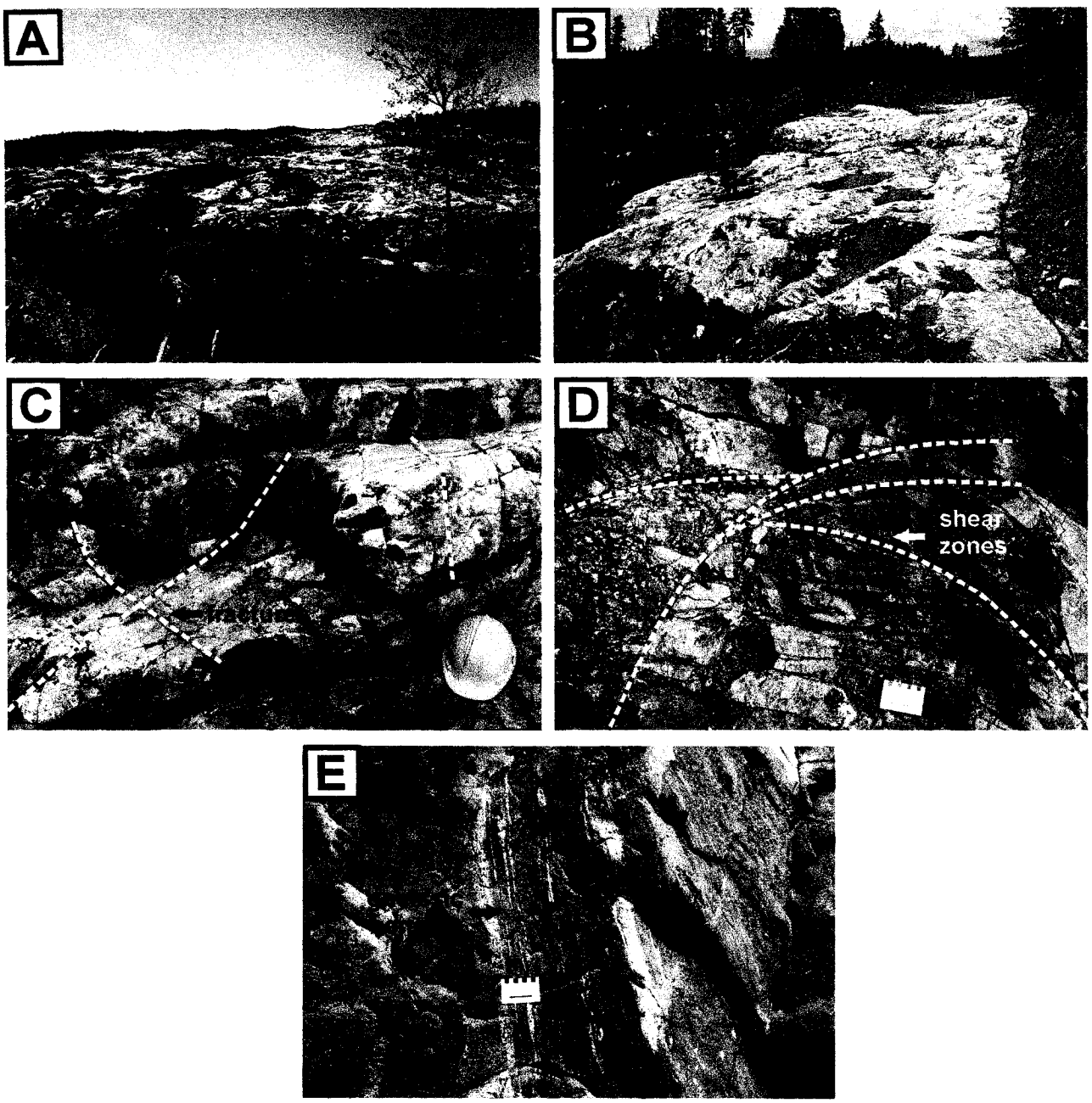


Fig. 3.2.

inaccessible, either due to work being under progress, or due to cover by overburden rock or soil piles. Extensive jointing within the embayment and proximal Offset (Fig. 3.2C) and localized deformation (Fig. 3.2D) along the margins of the Offset also limited the possible sampling locations.

Bordering the Offset and the distal part of the embayment was a footwall breccia zone. The zone is located between the leucocratic breccia and the granitoid footwall rocks, and is not differentiated in the mapping from the other footwall rocks. The breccia contains gneissic xenoliths and other clastic material up to 1-metre in length (Fig. 3.2E).

*3.1. (Two-pyroxene) Sublayer norite*

Samples were collected from three sites within the Whistle embayment, in the two-pyroxene sublayer norite (hereafter referred to as simply 'sublayer norite') unit (sites 17-19) (Fig. 3.3A). The medium- to coarse-grained, relatively un-metamorphosed, hypidiomorphic, equigranular norite specimens (Fig. 3.3B) are composed of 30-60% plagioclase, 10-30% ortho- and clinopyroxene (fig. 3.3C), <10% biotite plus a variable amount of quartz and potassium-feldspar and up to 3% magnetite. Cumulates of rounded pyroxene crystals are common (Fig. 3.3D), but not observed at all sites.

Samples are inclusionless, although fresh melanonorite and olivine-melanonorite inclusions have been identified within the same unit by other authors (Lightfoot et al., 1997). No veining is evident.

Albite twinning (Fig. 3.4A) is common in plagioclase crystals with only minor amounts of sericitization. In sample WL18A, several plagioclase crystals preserve oscillatory zonation. The preservation of igneous mineralogy and textures demonstrates that the rock has

**Figure 3.3.** Photomicrographs and field photos of the noritic rock types from the Whistle embayment and dyke. See Table 3.1 for mineral and textural term abbreviations. **(3.3A)** Field photo of sublayer norite (site WL18). Scale card is 9 cm wide; arrow points North. **(3.3B)** Photomicrograph of the sublayer norite. **(3.3C)** Clinopyroxene with albite and magnetite. **(3.3D)** Cumulates of orthopyroxene with intercumulus biotite and plagioclase in sublayer norite.

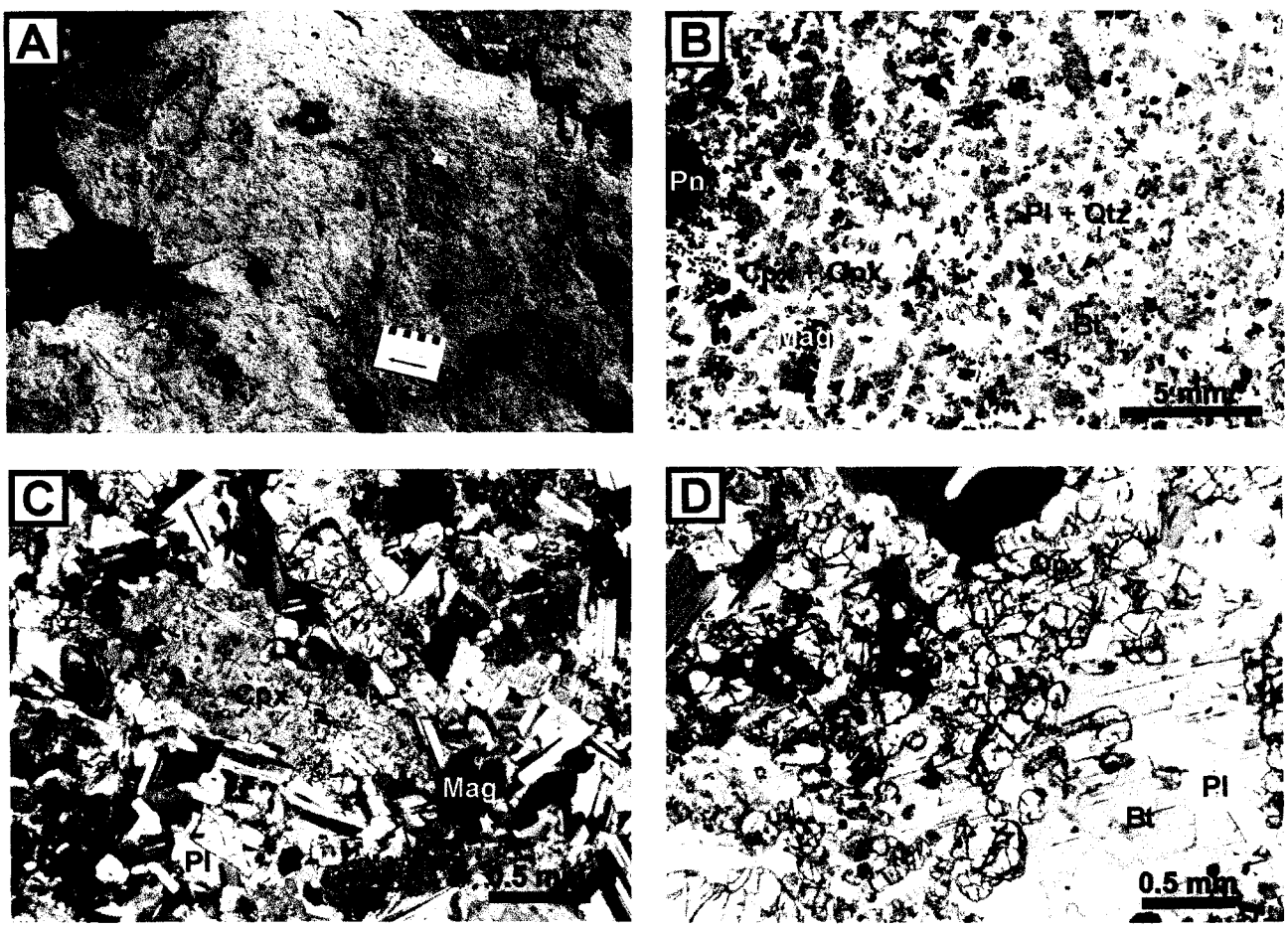


Fig. 3.3.

**Figure 3.4.** Photomicrographs of sublayer norite samples from the Whistle embayment. **(3.4A)** Preservation of igneous textures in sublayer norite; amphibole (Am) plus albite. **(3.4B)** Magnetite rimmed by chloritized biotite with quartz. **(3.4C)** Photomicrograph of leucocratic norite. **(3.4D)** Photomicrograph of mafic norite.

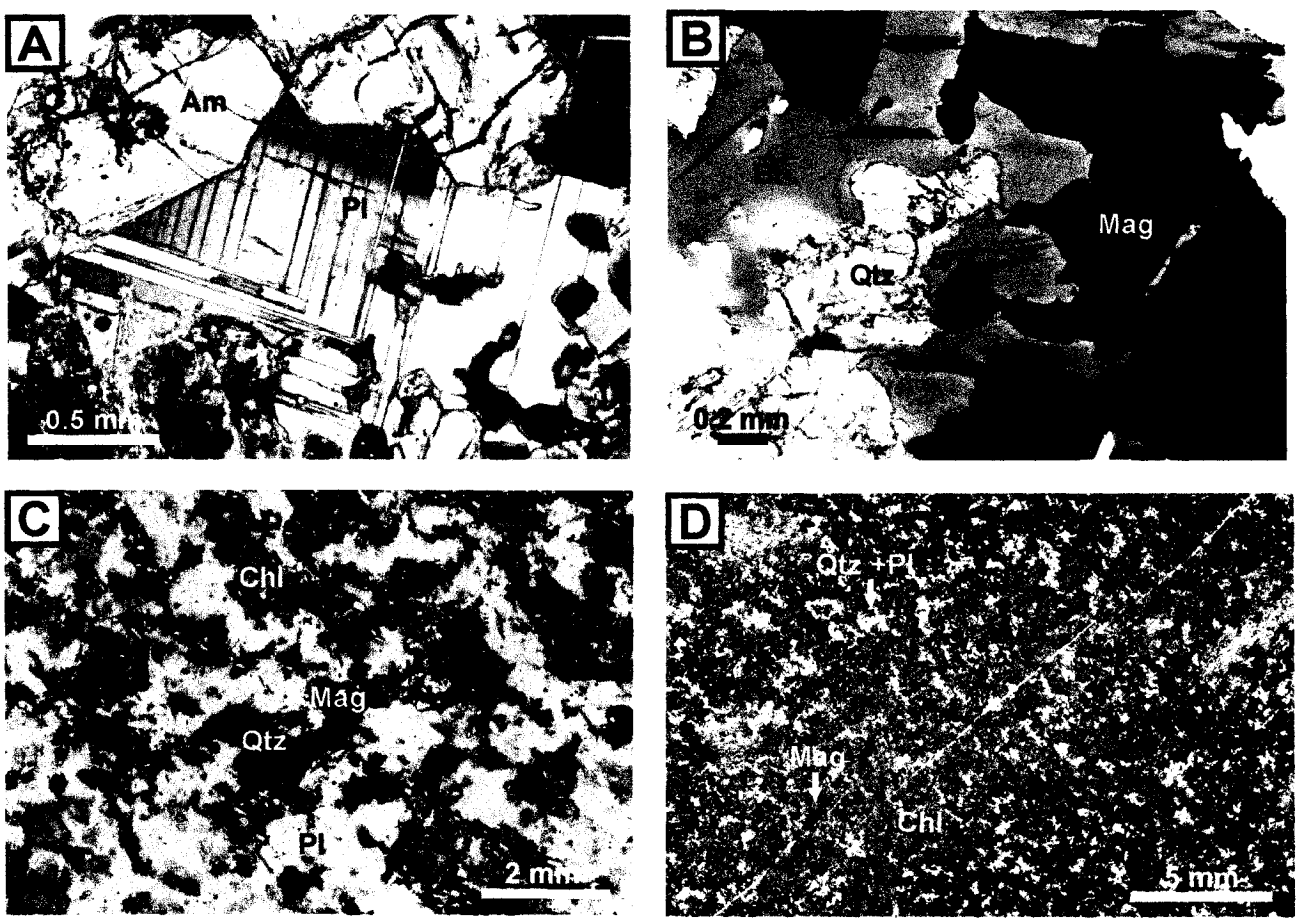
A
Am
Pl
0.5 mm
B
Mag
Qtz
0.2 mm
C
Chl
Mag
Qtz
Pl
2 mm
D
Qtz +Pl
Mag
Chl
5 mm

Fig. 3.4.

been neither metamorphosed nor tectonically deformed following its solidification. There is only minor chlorite replacement of some biotite and pyroxene crystals.

Sulfide blebs, which may include magnetite, are abundant in the thin sections and core samples. Disseminated magnetite is also fairly abundant. The coarse-grained magnetite crystals are often rimmed by biotite (Fig. 3.4B), which has been replaced by brown chlorite.

*3.2. Leucocratic norite*

The leucocratic norite (site WL12) (Fig. 3.4C), described by Lightfoot et al. (1997), is a coarse-grained, quartz-rich (30%) rock containing inclusions of the host lithologies. Specimens are strongly metamorphosed with the mafic minerals, biotite and pyroxene, being largely replaced by chlorite. The norite contains up to 15 %, typically coarse-grained, magnetite.

There is a bimodal grain size distribution with the plagioclase and quartz being very fine-grained and the mafic minerals being much coarser grained. The fine-grained plagioclase, which shows albite twinning, is likely secondary in origin having replaced the coarser primary albite. Fine-grained plagioclase is partially replaced by sericite. A high degree of greenschist-grade static metamorphism has overprinted most of the inclusions making them difficult to identify at the thin section scale. No veins were found within the samples.

There is a weak foliation defined by fine-grained rounded and elongated quartz crystals, which wrap around coarse-grained magnetite crystals. The coarse-grained magnetite, up to 1.0-mm in size, is often brecciated by the surrounding silicate minerals and there is a very strong association of magnetite with the mafic minerals. Magnetite is not found within the fine-grained groundmass of plagioclase and quartz.

*3.3. Mafic norite*

Samples were also collected from a mafic norite (site WL8) (Fig. 3.4D) within the distal section of the dyke. The fine-grained norite is strongly metamorphosed, with the pyroxenes and amphiboles (40-60%) being almost entirely replaced by chlorite. The mafic norite, which may be a xenolith, also contains 20-30% sericitized feldspars, 10% quartz, and 5-10% magnetite. The extreme chloritization of the samples is much more extensive than for any of the other sites in the North Zone. The mafic norite is much finer-grained than the sublayer and leucocratic norites. No twinning was observed in the feldspar crystals, as they are too fine-grained. Mineralogy is fairly evenly distributed with the exception of a few large sericite masses in one section (WL8C). There are no inclusions or evidence of veining in the samples. All crystals are anhedral with the exception of some coarse-grained magnetite crystals. There appears to be a bimodal distribution of grain size for magnetite between the coarse-grained (0.1-0.5 mm) and finer-grained (0.05-mm) magnetite.

*3.4. Leucocratic breccia*

The principal rock type sampled is leucocratic breccia (WL10,11,13-16), also referred to in the literature as footwall breccia (Lightfoot et al., 1997) or radial breccia (Murphy and Spray, 2004). The fine-grained (<2.0-mm), typically dark grey, breccia matrix is a quartz diorite (although potassium feldspar is locally present). The matrix consists of 30-40% partially sericitized feldspar, 20-30% quartz, and 20-40% biotite plus amphibole and pyroxene, variably replaced by chlorite. There does not appear to be much variation in the degree of metamorphism between sites. The magmatic breccia contains varying amounts of angular to sub-rounded mafic and granitic clasts (Fig. 3.5A-C). The feldspars within granitic

**Figure 3.5.** Photomicrographs and field photos from the proximal Whistle dyke. **(3.5A, 3.5B)** Field photographs showing angular to sub-rounded mafic and granitic clasts in leucocratic breccia. **(3.5C)** Photomicrograph of a mafic norite clast in leucocratic breccia. **(3.5D)** Typical blebby sulfides. **(3.5E)** A quartz and feldspar vein with micrographic intergrowth and acicular magnetite inclusions.

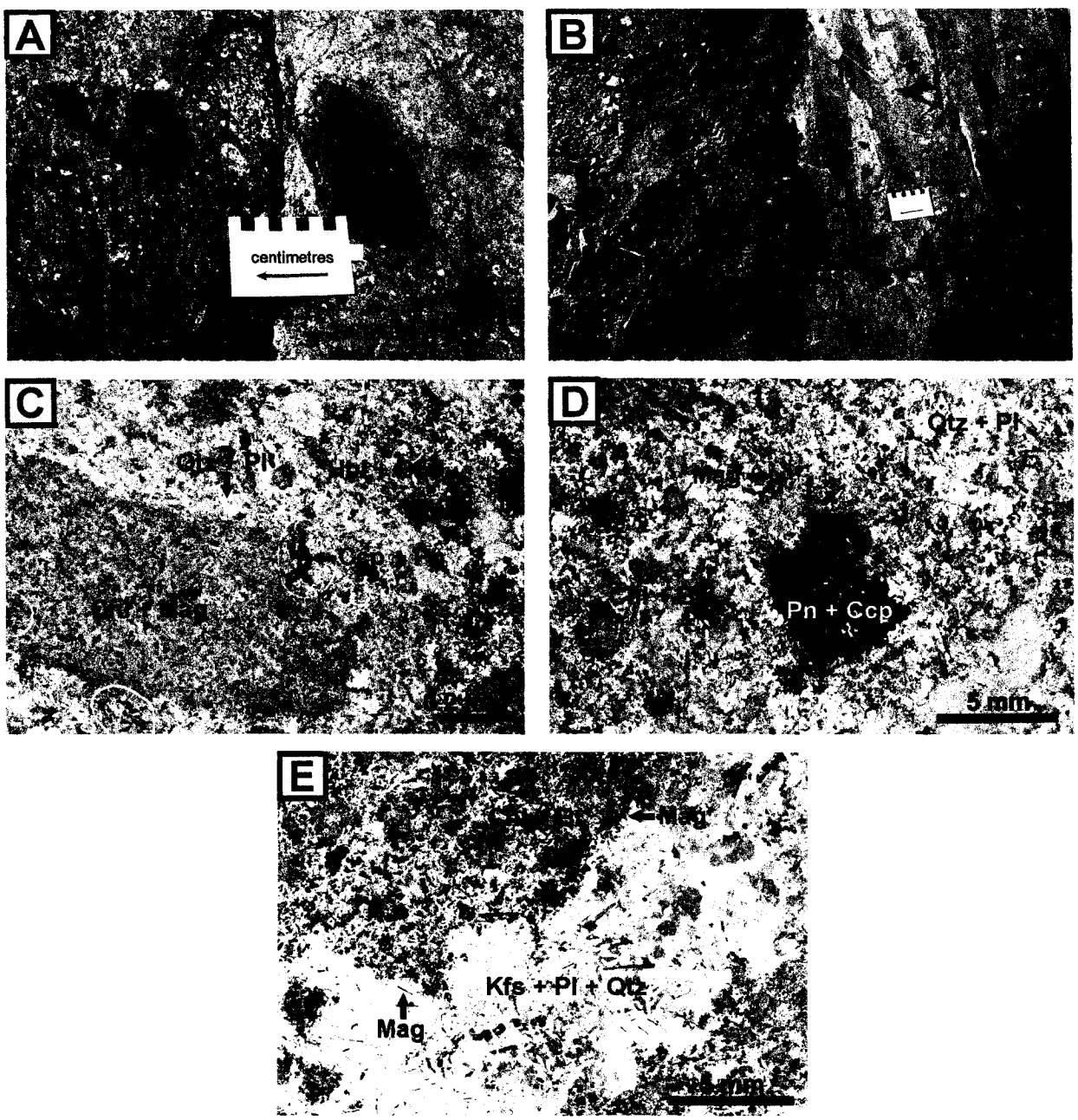


Fig. 3.5.

clasts are partly replaced by sericite. Sample WL11A contains a clast that is highly metamorphosed and is similar in texture and composition to the mafic norite samples (Fig. 3.5C). The 0.5- by 1.5-cm rounded clast is most like a fine-grained meta-norite, finer-grained than matrix, more abundant in coarse-grained magnetite than matrix. WL11A is also the only leucocratic breccia sample for which pyrrhotite was identified. The leucocratic breccia was also sampled (sites WL7, WL9) near the North Zone deposit within a section of the Offset stripped by FNX Mining Ltd. during the summer of 2002.

Veins of epidote or chlorite or epidote-chlorite are present in some sections and sulfides are present in blebby (up to 5 mm wide) (Fig. 3.5D) and disseminated forms. Magnetite is both disseminated, where associated with mafic silicate minerals, and present in sulfide blebs. A quartz-feldspar vein in WL9D (Fig. 3.5E) contains acicular magnetite crystals. Micrographic intergrowths of quartz and potassium-feldspar are common in the vein, while plagioclase is partially replaced by sericite. Cumulates of radiating sericitized plagioclase laths among intercumulate quartz in samples WL11A and WL13A resemble the textures of plagioclase laths in the spherulitic textured amphibole quartz diorite (site WL4) described below.

*3.5. (Spherulitic) Amphibole-quartz diorite*

The amphibole-quartz diorite, site WL4, is composed of 15-30% radiating clusters of acicular green amphibole (Figs. 3.6A,B) and radiating clusters of plagioclase laths (20-30%). Acicular amphibole crystals are up to 2.0-cm long and are pseudomorphed after pyroxene. The radiating amphibole clusters produce 'spherulites' up to 4.0-cm wide. A few hexagonal shaped pyroxene crystals are preserved that are only partially replaced by amphibole, whereas other pyroxene crystals are entirely replaced by amphibole. Amphibole and biotite

**Figure 3.6.** Photomicrographs and field photos from the Whistle dyke of amphibole-quartz diorite. **(3.6A)** Field photograph of spherulitic amphiboles in amphibole diorite. Arrow points to radiating cluster of amphibole crystals. **(3.6B)** Acicular amphiboles and plagioclase laths. **(3.6C)** Epidote and chlorite in vein with inclusions of quartz. **(3.6D)** Granophyric and micrographic intergrowths with plagioclase laths in amphibole-quartz diorite.

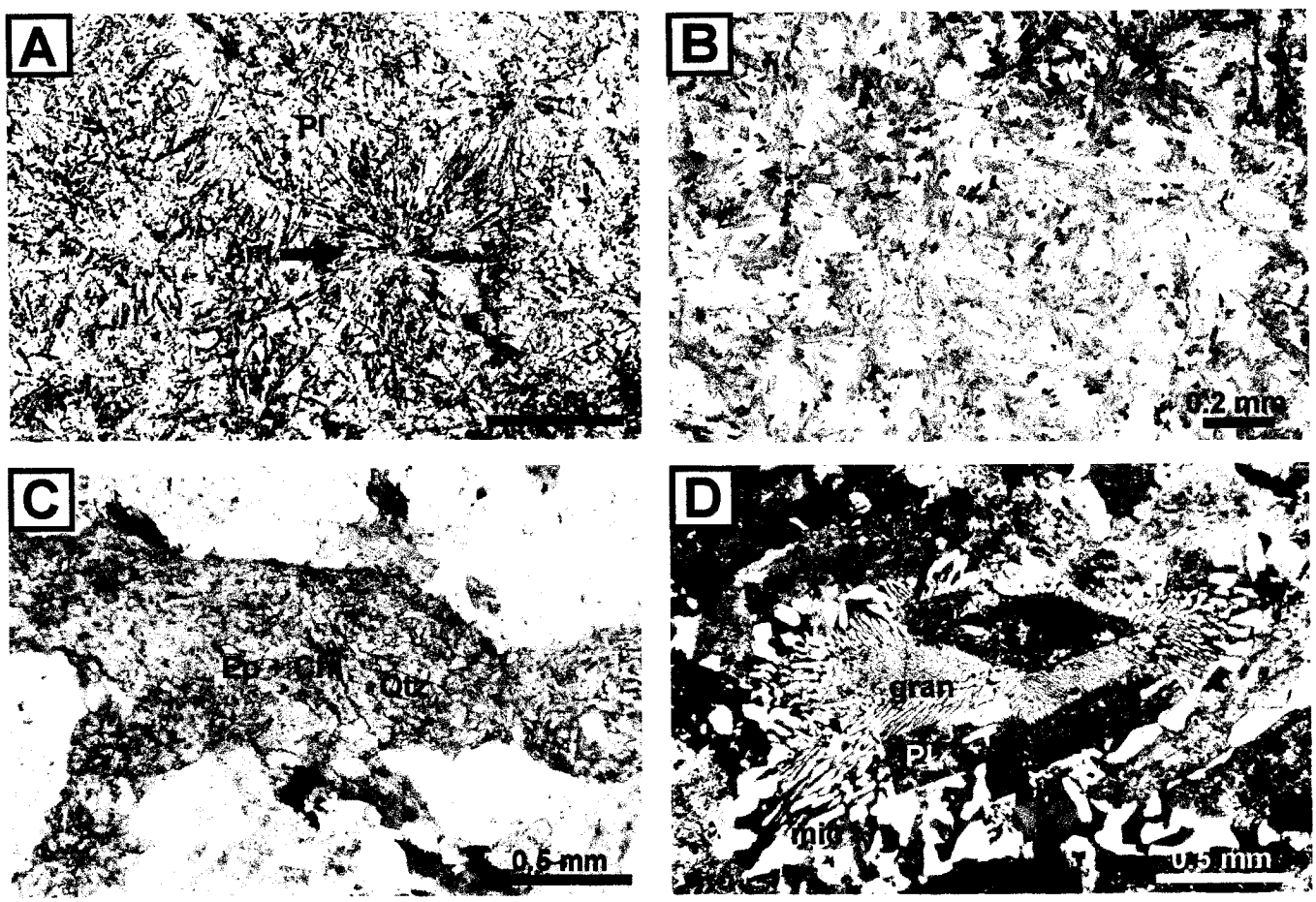


Fig. 3.6.

(<5%) are extensively chloritized and veins of epidote and chlorite are common (Fig. 3.6C), indicating a high degree of static greenschist-grade metamorphism. Plagioclase laths are variably altered to sericite ± minor epidote. Granophyric and micrographic intergrowths of quartz and potassium feldspar are also well preserved (Fig. 3.6D). The formation of similar micrographic and granophyric intergrowths in the Sudbury Igneous Complex is thought to have resulted from a sudden drop in water pressure in the magmatic system (Therriault et al., 2002). Quartz comprises up to 10% of the samples. Albite exsolution lamellae are observed in some potassium feldspar crystals. Opaque minerals, likely magnetite, have a platy to acicular habit and make up approximately 1-2% of the rock and are strongly associated with the mafic minerals.

The inclusion free amphibole-quartz diorite is similar to the 'spherulitic' quartz diorites described along the margins of the Copper Cliff Offset dyke (Grant and Bite, 1984).

*3.6. Massive sulfides*

Massive sulfides (WL1m,5,6) (Fig. 3.7A) and a sulfide-rich breccia (WL1d,2,3) of the chalcopyrite-rich North Zone deposit, are exposed at surface in the distal portion of the Whistle Offset dyke. The sampled massive sulfides of the North Zone deposit are composed of 70-85% chalcopyrite, 5-10% magnetite, 3-10% pentlandite, 1-5% pyrrhotite, ± minor pyrite, arsenopyrite, millerite, galena, hematite and titanomagnetite. Inclusions of quartz crystals, showing moderate undulose extinction, are present in some specimens. The massive sulfides will be described in greater detail in Chapter 4.

**Figure 3.7.** Photomicrographs and field photos from the Whistle dyke of massive chalcopyrite and sulfide breccia. **(3.7A)** Field photo of massive sulfide North Zone deposit. **(3.7B, 3.7C)** Disseminated versus sharp contacts between leucocratic breccia and chalcopyrite in sulfide-rich breccia. **(3.7D)** Photomicrograph of intergrowth of chlorite pseudomorphing biotite and chalcopyrite in sulfide-rich breccia.

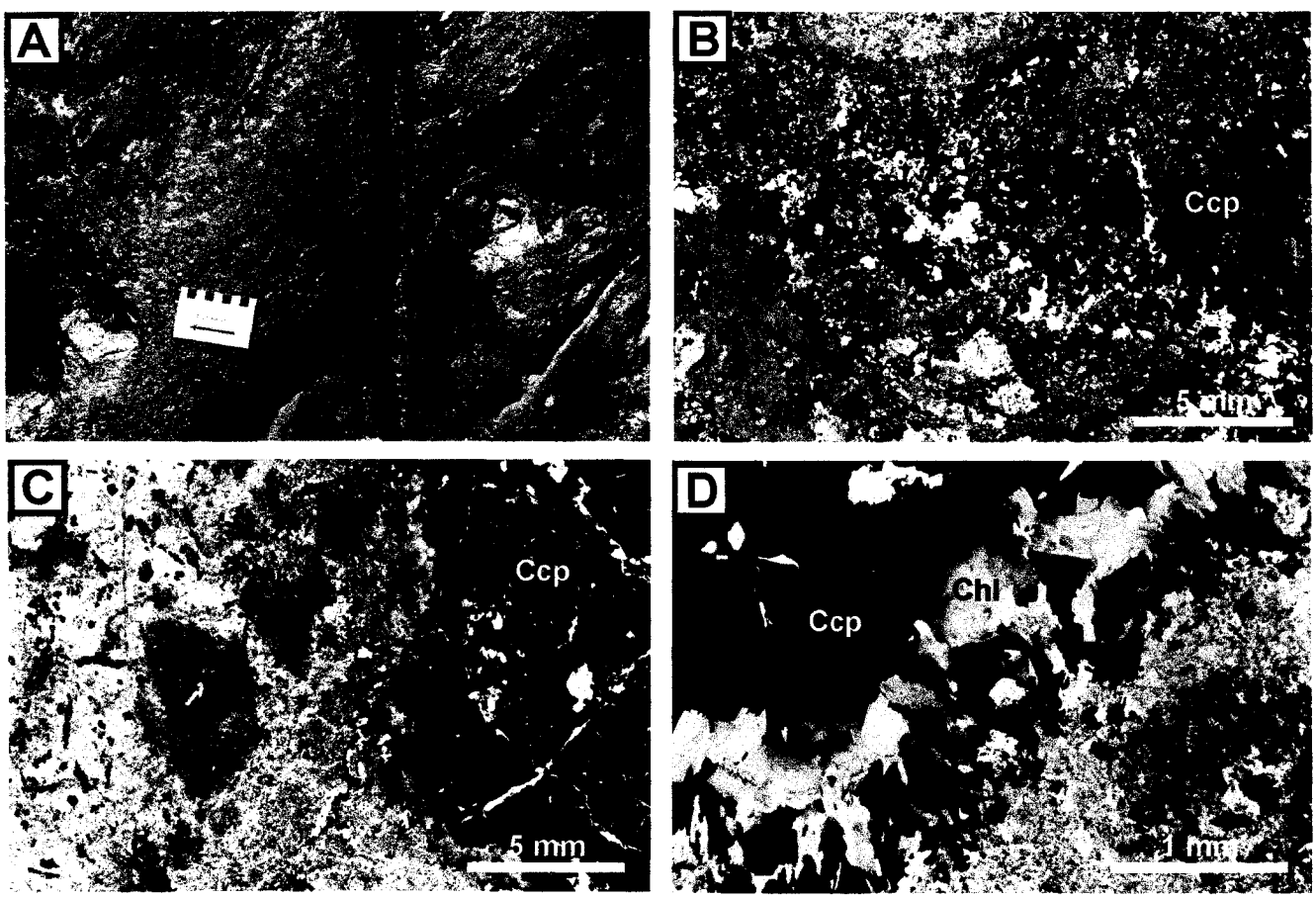


Fig. 3.7.

*3.7. Sulfide-rich breccia*

A sulfide-rich breccia (Figs. 3.7B,C) occurs at the contact between the massive sulfide body and the host leucocratic breccia rocks, and is interpreted to represent mechanical and chemical interaction between the sulfide melt and host silicate rock. Samples collected from the breccia are considered as a separate rock type from the massive sulfides due to differences in their magnetic properties, which will be described later. Intergrowths of chlorite pseudomorphs of biotite, and chalcopyrite (Fig. 3.7D) are common at the transition between chalcopyrite inclusions in the silicate matrix and the more massive chalcopyrite. The breccia comprises of anywhere from 10-90% chalcopyrite. Sulfide-rich breccia specimens (sites WL1m and WL2) typically contain less than 1% magnetite, while specimens from site WL3 contain up to 15% magnetite. Cumulates of subhedral to euhedral orthopyroxene crystals are present as inclusions in the chalcopyrite. The orthopyroxene crystals are relatively unaltered compared to the inclusions of amphiboles and biotite, which are replaced by chlorite to varying degrees. Anhedral quartz inclusions show resorption textures along their edges, and undulose extinction. Plagioclase is being altered to sericite, but some albite twinning is preserved. Masses of sericite may represent the complete replacement of granitic clastic material included in the chalcopyrite. Inclusions of the host leucocratic breccia occasionally contain chlorite +/- minor quartz and magnetite veins.

## Chapter 4: Opaque Mineralogy

The opaque mineralogy of the sample suite was investigated using reflected-light microscopy as well as the scanning electron microscope (SEM) at Carleton University. Particular attention was paid to the sulfide-rich rocks of the North Zone deposit, in order to identify potential carriers of magnetic remanence. The SEM and petrographic observations reveal that mineralization within the North Zone deposit consists of massive chalcopyrite ± pyrrhotite, pentlandite, pyrite, arsenopyrite, galena, millerite, magnetite, titanomagnetite and hematite. Platinum-group metals were also identified in some samples using SEM. Mineralization elsewhere in the dyke and within the embayment consists of blebby and disseminated sulfides and magnetite. By far the most abundant ferromagnetic phases observed in the sample suite were magnetite and titanomagnetite.

### *4.1. Sulfides*

The SEM and petrographic observations reveal that sulfide mineralization within the North Zone deposit typically consists of chalcopyrite ± pyrrhotite, pentlandite, pyrite, arsenopyrite, galena and millerite. Chalcopyrite ($CuFeS_2$) is the principal sulfide mineral in the North Zone deposit. It is also present as small blebs dispersed throughout the leucocratic breccia and noritic samples. Coarse-grained pentlandite ($(Fe,Ni)_9S_8$) and pyrite (FeS) crystals are found in the sulfide deposit as well as in the sublayer norite (Fig. 4.1A) and commonly contain flames or lamellae intergrowths of chalcopyrite or millerite (NiS). Euhedral cubic crystals of pyrite are often rimmed with fine-grained silicates. Pyrrhotite ($Fe_{1-x}S$), as well as pentlandite, pyrite and arsenopyrite (FeAsS), form partial or complete rims around magnetite ($Fe_3O_4$) as the sulfide minerals form at the expense of the magnetite. Fine-grained galena

**Figure 4.1.** Backscatter SEM images and reflected-light photomicrographs from the Whistle dyke. **(4.1A)** SEM image of magnetite and titanomagnetite (Ti-Mag) in blebby pyrite (py)-chalcopyrite intergrowth in norite. **(4.1B)** SEM image of galena crystal with a second phase of bismuth telluride in a chalcopyrite groundmass in massive sulfide. **(4.1C)** Photomicrograph of magnetite rimmed by pyrrhotite in chalcopyrite matrix in a massive sulfide sample. See Table 3.1 for mineral and textural term abbreviations. **(4.1D)** SEM image of brecciated magnetite crystals within massive chalcopyrite. **(4.1E)** SEM image of brecciated magnetite crystal with titanomagnetite along the contacts in leucocratic norite. **(4.1F)** SEM image of magnetite and titanomagnetite along cleavages of hornblende (hbl) crystal in sublayer norite.

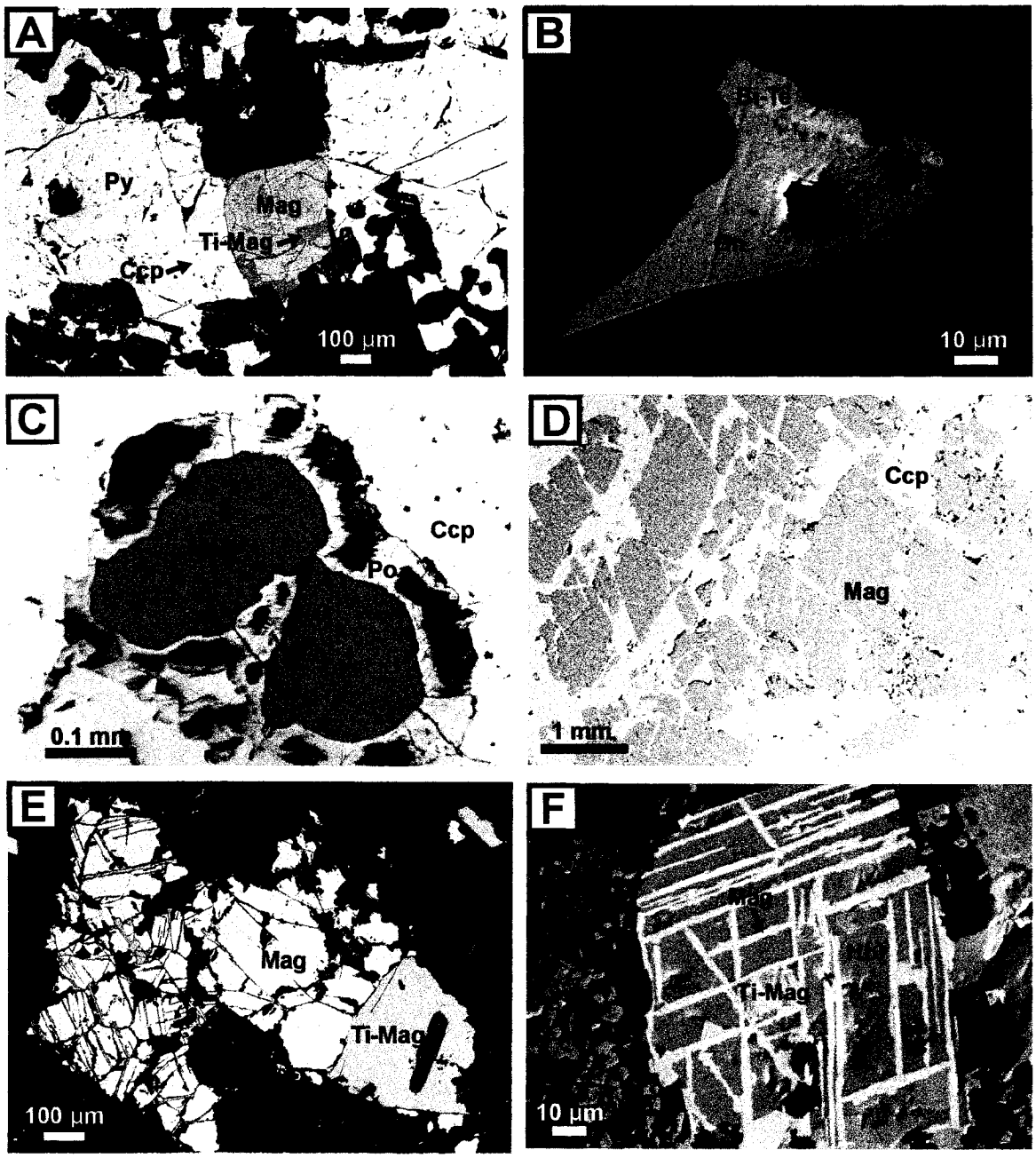
A
Py
Mag
Ti-Mag
Ccp
100 µm
B
10 µm
C
Ccp
Po
0.1 mm
D
Ccp
Mag
1 mm
E
Mag
Ti-Mag
100 µm
F
Ti-Mag
10 µm

Fig. 4.1.

(PbS) crystals (Fig. 4.1B) are dispersed throughout the sulfide-rich samples from the North Zone.

*4.2. Iron-titanium oxides*

Two generations of magnetite are present in the dyke rocks. The first generation is represented by coarse-grained magnetite that is interpreted to be of primary origin. Sulfide phases, most commonly pyrrhotite (Fig. 4.1C), but also pyrite and pentlandite, form rims on the coarse-grained magnetite. Within the massive chalcopyrite, brecciation of magnetite crystals was observed (Fig. 4.1D). Resorption textures along the edges of brecciated magnetite crystals indicate partial dissolution by the sulfide-rich melt. Rare cassiterite ($SnO_2$) also forms along the contact between the adjacent brecciated magnetite crystals shown in Fig. 4.1D. Fracturing of coarse-grained magnetite was also seen in the leucocratic norite specimens (Fig. 4.1E) with titanomagnetite forming along the fractures. Alignments of rounded magnetite crystals were observed in hand samples and thin sections of several massive sulfide specimens. Rounded coarse-grained crystals are also present as inclusions in sulfide blebs within the norites (Fig. 4.1A) and leucocratic breccia specimens. The textures in Figs. 4.1C,D,E are consistent with the sulfides forming subsequent to the magnetite crystals, supporting the interpretation that the magnetite crystals in that sample are xenocrysts from the host lithologies. Those observations are consistent with emplacement of the massive sulfide after emplacement of the other magmas (Murphy and Spray, 2002).

Fine-grained secondary magnetite and titanomagnetite ($Fe(Fe,Ti)_2O_4$) have partly replaced mafic silicate minerals along cleavages (e.g. hornblende in Fig. 4.1F). In a single norite specimen, a myrmekite- or symplectite-like replacement texture is defined by titanomagnetite in very fine-grained silicate alteration product (Fig. 4.2A). This texture

**Figure 4.2.** Backscatter SEM images. **(4.2A)** Symplectite-like intergrowth of titanomagnetite in a fine-grained silicate matrix in sublayer norite. **(4.2B)** Titanomagnetite exsolution in a magnetite crystal in sublayer norite. **(4.2C)** Magnetite exsolution lamellae in a heart-shaped titanomagnetite crystal. Heart is surrounded by magnetite crystals in the leucocratic norite sample. **(4.2D)** Coarse-grained magnetite crystal in sublayer norite showing crosshatched pattern. **(4.2E)** Michenerite crystal surrounded by a silver telluride mineral phase in a chalcopyrite groundmass in a sulfide-rich breccia. **(4.2F)** Palladium-bismuth mineral with a silver-rich rim in a sulfide-rich breccia sample.

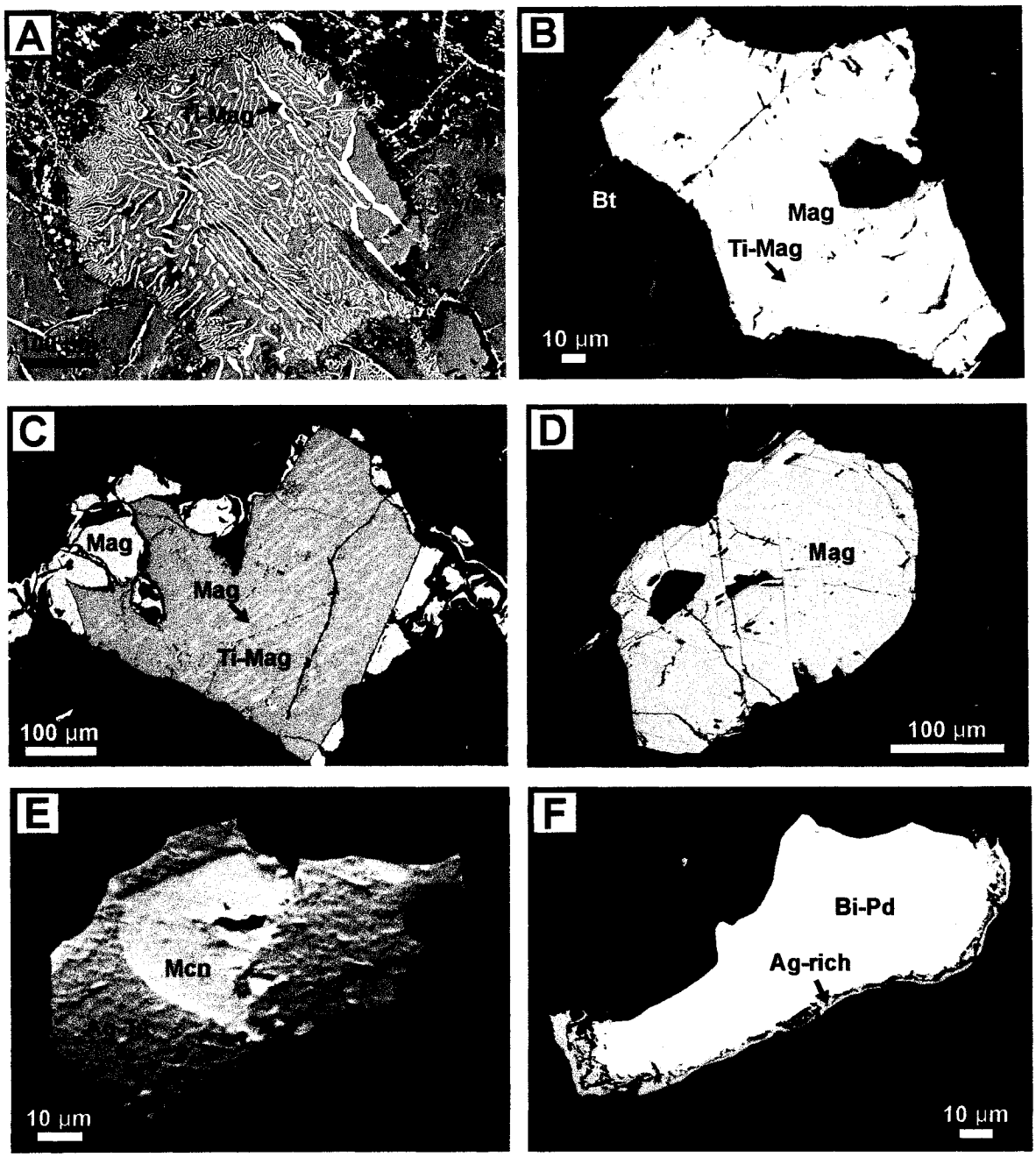
A
Ti-Mag
B
Bt
Mag
Ti-Mag
10 μm
C
Mag
Mag
Ti-Mag
100 μm
D
Mag
100 μm
E
Mcn
10 μm
F
Bi-Pd
Ag-rich
10 μm

Fig. 4.2.

possibly formed during cooling of the rocks. Coarse magnetite crystals may also have lamellar oxyexsolutions of titanomagnetite such as in the crystal in a norite specimen shown in Fig. 4.2B. Fine exsolution lamellae of magnetite were observed in a heart-shaped titanomagnetite crystal (Fig. 4.2C). Magnetite crystals surround the titanomagnetite heart with titanomagnetite possible representing eutectoid replacement by the secondary phase. Veins of magnetite and sulfides in some massive sulfide samples are indicative of some remobilization during metamorphism. Late-stage silicate veins are also found in some samples. The coarse-grained single-domain magnetite is most common in the massive sulfide and norite sites. A typical coarse-grained magnetite crystal, with a faint crosshatched pattern in backscatter images of a sublayer norite specimen, is shown in Fig. 4.2D.

Fine-grained hematite ($Fe_2O_3$) is found in sulfide-rich breccia and massive sulfide, making up less than 0.1% of the samples.

*4.3. Platinum-group and other precious-metal minerals*

Platinum-group and other precious-mineral metals are present as trace minerals in the massive sulfide and sulfide-rich breccia samples. The metals were identified using SEM. In a sulfide-rich breccia sample, a michenerite ((Pd,Pt)BiTe) crystal enclosed in a second silver telluride phase was identified (Fig. 4.2E). Within the same thin section a palladium bismuth mineral (possibly froodite) with an Ag-rich rim was identified (Fig. 4.2F). Silver-rich michenerite and bismuth phases were also present. Fig. 4.1B shows a galena crystal with a second bismuth telluride phase occurring in a massive sulfide sample. The contact between the two phases is not well defined. A single silver-bismuth selenide (Ag,Bi,Se) crystal as well as an arsenide, sperrylite ($PtAs_2$), included in a pentlandite crystal, were identified in a massive sulfide section.

## Chapter 5: Methodology of the magnetic study

Magnetic properties of the samples were measured at the Magnetics Research Facility for Tectonic Studies (MRFTS) at the University of Ottawa and at the Geological Survey of Canada (Ottawa). Representative thin sections from each of 20 sampling sites were studied petrographically, using transmitted and incident light sources. Selected samples were further investigated using the SEM at Carleton University, in Ottawa. The petrographic and SEM investigations allowed us to identify the principal carriers of magnetic susceptibility and of magnetic remanence. The ferromagnetic (*s.l.*) mineralogy was further investigated using acquisition of anhysteretic remanence and demagnetization of anhysteretic remanence. Subsequently, the anisotropy of magnetic susceptibility (AMS), the anisotropy of anhysteretic remanence (AAR) and the anisotropy of partial anhysteretic remanence (ApAR) magnetization were measured for the 210 oriented specimens. The magnetic anisotropy techniques allowed the preferred orientations of paramagnetic and ferromagnetic crystals within samples collected from the Whistle Offset to be measured. These mineral fabrics may record the symmetry of flow of rocks or magma thereby recording the emplacement of the Offsets and the sulfide deposits they host. The AAR technique was used to isolate the magnetic fabrics of the ferromagnetic minerals in the dyke rocks. Ferromagnetic minerals are stable remanence carriers as they are able to retain a magnetization after the removal of a magnetic field (Tarling and Hrouda 1993). Since paramagnetic and diamagnetic minerals do not carry a remanent magnetization, their orientations can only be measured using their susceptibilities in the presence of an applied magnetic field. The AMS technique measures the magnetic susceptibilities of specimens in the presence of a magnetic field allowing the AMS of paramagnetic and diamagnetic minerals, as well as the ferromagnetic minerals, to be

measured. The use of both the AAR and the AMS techniques allows for the discrimination between the fabrics formed only by ferromagnetic minerals and the bulk fabrics formed by all Fe-rich minerals (McCabe et al., 1985).

Rocks are said to be magnetically anisotropic if the strength of their magnetic properties is dependent on the orientation of the specimen within the applied field. A rock would be said to be magnetically isotropic if the strength of the magnetization were constant in the rock irrespective of the orientation of the specimen within the field (Tarling and Hrouda, 1993). The two main factors controlling the natural magnetic anisotropy of rocks are the shape alignment of ferromagnetic grains and the lattice alignment of crystals with crystalline anisotropies (Hrouda, 1982). Shape anisotropies determine the AMS and AAR in certain minerals such as magnetite. They arise because the alignment of the electron spins by an applied field creates north and south magnetic poles at opposite points on the surface of each grain. In non-symmetrically shaped grains the resulting forces are reduced when the surface poles are furthest apart. The induced magnetization is preferentially oriented in such a way as to minimize the area where magnetization is perpendicular to the surface (Jackson, 1991). The AMS of most minerals is determined by crystalline anisotropies (i.e. crystal structure), which also control grain shape. Crystalline anisotropies arise in crystals when electron spins align more easily along a specific direction due to the action of lattice forces on the electron-spin configurations. The magnetic susceptibility in an applied field is controlled by these directions (Hrouda, 1982).

### *5.1. Anisotropy of Magnetic Susceptibility (AMS)*

The low-field magnetic susceptibilities of the 10.8 $cm^3$ cylindrical specimens was measured at room temperature using an AGICO (Czech Republic) high precision KLY-2

Kappabridge instrument. Susceptibilities were measured using a 15-orientation scheme and the AMS was calculated from the measurements using the ANISO20 software delivered with the KLY-2 instrument. The AMS is a second order tensor (K) relating the intensity of the applied magnetic field (H) to the resulting magnetic moment (M = K*H). The tensor is geometrically represented as an ellipsoid with the principal axes corresponding to the maximum ($K_1$), intermediate ($K_2$) and minimum ($K_3$) magnetic susceptibilities. In general, the maximum susceptibility axis ($K_1$) is oriented parallel to the mineral lineation while the minimum susceptibility axis ($K_3$) is oriented perpendicular to the mineral foliation. Within magmatic flow planes in dyke rocks, $K_1$ is therefore close to the flow line while $K_3$ is sub-perpendicular to the flow plane (Rochette et al., 1991). The average AMS ellipsoid was calculated for each sampling site using the Jelinek tensor-averaging method (Jelinek, 1978). The anisotropy of magnetic susceptibility is a widely utilized method and has previously been used to study another Offset dyke in the Sudbury camp (Scott and Benn, 2001; Scott and Benn, 2002), as well as in the North and East Ranges of the Sudbury Igneous Complex (Cowan, 1999).

Several scalar parameters are utilized in the analysis of AMS data. The average susceptibility is given by $K_{av} = (K_1 + K_2 + K_3)/3$, and $P = K_1 / K_3$ is the degree of anisotropy. The value of $T = [2(\ln K_2 - \ln K_3) / (\ln K_1 - \ln K_3)] - 1$ describes the shape of the susceptibility ellipsoid, where T =1 for purely oblate ellipsoids, T = -1 for purely prolate ellipsoids, and T = 0 for neutral triaxial ellipsoids. Taken together, the values of $L = K_1/K_2$ and $F = K_2/K_3$ also describe the shape of the AMS ellipsoid. L and F are analogous to the parameters that are plotted on the well-known Flinn diagram for finite strain state and represent the eccentricity of the ellipsoid based on the magnetic lineation (L) and foliation (F) respectively.

The three principal axes of the AMS ellipsoid are parallel to the shape and/or crystallographic preferred orientations defined by all iron-rich ferromagnetic and paramagnetic minerals in the rock (Borradaile and Henry, 1997). The AMS thus provides a bulk petrofabric with contributions from all of the ferromagnetic (*s.l.*) and paramagnetic iron-rich minerals. The individual influence of different mineral grains on the AMS is dependent on both the inherent susceptibility and concentration of those grains (Fig. 5.1). The paramagnetic and ferromagnetic (*s.l.*) magnetic mineralogy of many of the studied samples is complex. The paramagnetic silicate mineralogy that is expected to contribute to the susceptibility signal of the sample suite includes both primary igneous minerals (biotite, orthopyroxene, clinopyroxene) and metamorphic minerals (chlorite, Ca-Fe amphibole). Susceptibilities of diamagnetic minerals (quartz, calcite) are extremely low compared to those of paramagnetic minerals (amphiboles, pyroxenes, micas, and chlorite) and they will therefore have no significant influence on the bulk susceptibility or on the AMS of the samples.

The opaque ferromagnetic (*s.l.*) minerals magnetite, titanomagnetite, pyrrhotite, and to a lesser extent hematite, may be expected to contribute to the susceptibility signal. Magnetite and titanomagnetite are both ferrimagnetic and will therefore influence both the AMS and ARM results. Hematite is antiferromagnetic but can exhibit 'parasitic magnetism' whereby one of the two magnetic moments may be slightly more magnetic than the other or the two magnetic moments may not be exactly anti-parallel (Tarling and Hrouda, 1993). This means that the magnetic properties may vary depending on the composition of the hematite. Hematite has a much lower susceptibility and remanence intensity than the other ferromagnetic minerals. Hematite also has a much higher coercivity and is more strongly anisotropic than the other ferromagnetic minerals. The influence of pyrrhotite is dependent

**Figure 5.1.** The contributions of some ferromagnetic (*s.l.*) and paramagnetic minerals to the bulk susceptibility of a rock. The individual influence of the mineral grains on the bulk susceptibility is dependent on the intrinsic susceptibility of the minerals as well as its concentration. Adapted from Hrouda and Kahan (1991).

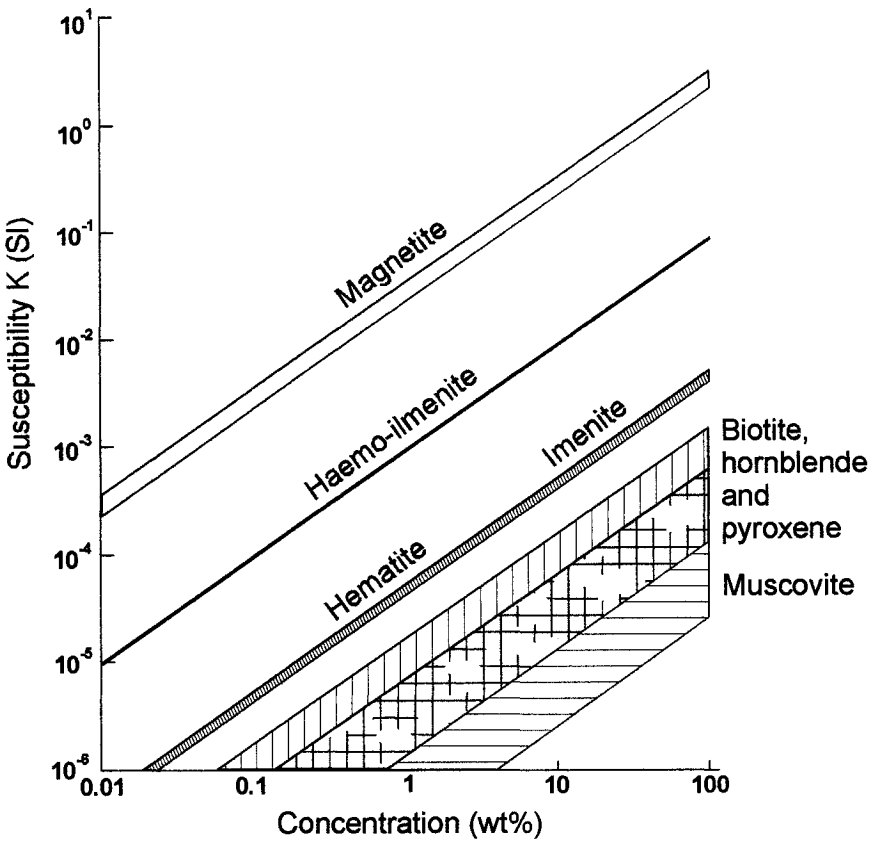
Susceptibility K (SI)
10^1
10^0
10^-1
10^-2
10^-3
10^-4
10^-5
10^-6
0.01
0.1
1
10
100
Concentration (wt%)
Magnetite
Haemo-ilmenite
Ilmenite
Hematite
Biotite, hornblende and pyroxene
Muscovite

Fig. 5.1.

on its crystal lattice. It is ferrimagnetic for slightly-monoclinic/pseudo-hexagonal forms and antiferromagnetic for hexagonal forms (Hrouda, 1982). Chalcopyrite and pyrite are both paramagnetic, but have low susceptibilities (<5000 x $10^{-6}$ SI; Hunt et al., 1995), and will therefore have only a minor influence on the AMS.

The presence of certain magnetic minerals may lead to anomalous magnetic fabrics that may not be easily related to the petrofabric of interest (Rochette et al., 1999). Single-domain (SD) titanomagnetite and magnetite grains produce intrinsically inverse magnetic fabrics, meaning that the maximum susceptibility axis of those grains is normal, rather than parallel, to their maximum dimension (Rochette et al., 1992). The presence of a mixture of SD and multi-domain (MD) magnetite (Fig. 5.2A) may produce anomalous fabrics (Benn et al., 1993; Pignotta and Benn, 1999). The influence of any SD magnetite, which is most likely secondary in origin, is dependent on the concentration of the mineral grains within the sample. Magnetite also shows a gradual increase in susceptibility with the transition from SD to MD behaviour (Fig. 5.2B).

The AMS of some samples is therefore a combined signal from igneous and metamorphic minerals and cannot be simply interpreted in terms of emplacement flow of the Whistle Offset dyke. For that reason, the anisotropy of remanent magnetization was also measured.

*5.2. Anisotropy of Anhysteretic Remanent (AAR) magnetization*

Imparting anhysteretic remanence (AAR), involves the removal of all natural magnetic remanence from a specimen by subjecting it to a slowly decaying alternating field. The magnetic remanence is carried primarily by the magnetite and titanomagnetite crystals in the samples. There is also a minor contribution from small amounts of hematite and

**Figure 5.2.** Influence of single- and multi-domain magnetite on susceptibility. **(5.2A)** Model of normalized principal susceptibilities, for a mixture of single- and multi-domain crystals, versus the proportion (P) of single-domain magnetite in the total susceptibility. Stereonets show the resulting $K_1$, $K_2$ and $K_3$ directions. Adapted from Rochette et al., 1999. **(5.2B)** Susceptibility of equidimensional magnetite grains plotted as a function of domain state. There is a marked drop in susceptibility at the change from the superparamagnetic (SP) to single-domain (SD) states. A gradual increase is then seen as the pseudo-single (PSD) and multi-domain (MD) states are approached. Adapted from Thompson and Oldfield, 1986.

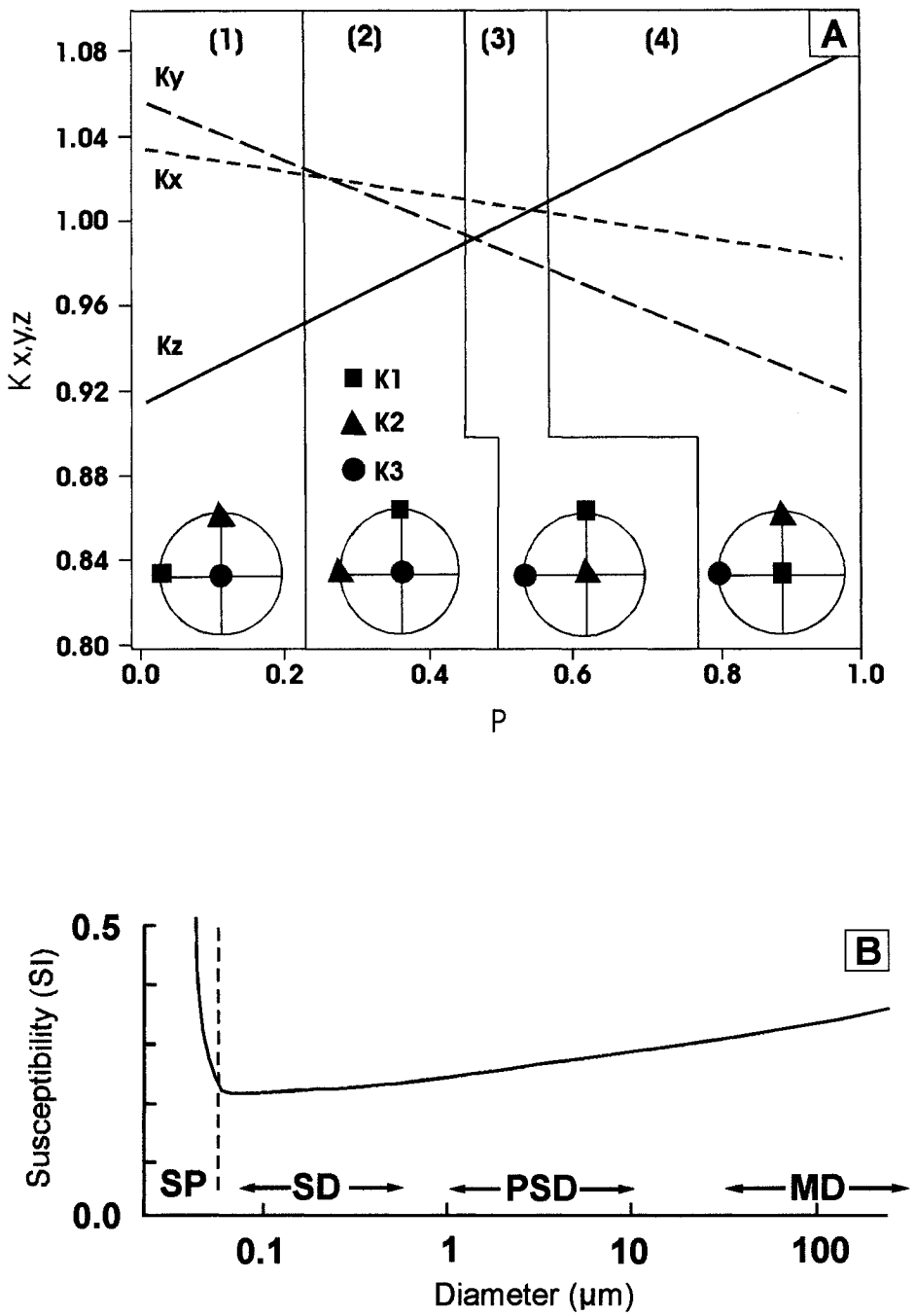
A
(1)
(2)
(3)
(4)
Ky
Kx
Kz
K1
K2
K3
K x,y,z
P
1.08
1.04
1.00
0.96
0.92
0.88
0.84
0.80
0.0
0.2
0.4
0.6
0.8
1.0
B
Susceptibility (SI)
0.5
0.0
SP
SD
PSD
MD
0.1
1
10
100
Diameter (μm)

Fig. 5.2.

pyrrhotite in the massive sulfide and in the sulfide-rich breccia. A new anhysteretic remanence is imparted in a predefined orientation by subjecting the specimen to a slowly decaying alternating field with a superimposed, co-axial direct bias field. Measurements of the anhysteretic remanence applied in several orientations provide the data for a second-order tensor similar to the AMS, but which only records the fabrics defined by the ferromagnetic minerals, magnetite, titanomagnetite, hematite and pyrrhotite.

The specimens were first demagnetized in a peak alternating field of 100 mT using a Molspin Shielded Demagnetizer. The specimens were demagnetized at a decay rate of 0.017 mT per cycle, for a peak field of 100 mT, to remove any pre-existing remanence before applying the anhysteretic remanence (AR). The Molspin demagnetizer has a two-axis tumbler to ensure that all parts of the specimen are subject to the demagnetization. The coil assembly and sample are contained inside a triple walled mu-metal bucket shield during the process.

AR was then imparted to the samples using the Molspin alternating-field demagnetizer equipped with a specially designed DC coil (provided by L. Molyneux, Molspin Ltd.) to superimpose a lower-intensity (0.1 mT) coaxial bias direct field (DF) on the decaying alternating field (AF), from a peak field of 100 mT. Special sample holders constructed of diamagnetic material were designed so a specimen could be placed within the DC coil in one of 7 orientations, corresponding to the Nye 7-position orientation scheme (Borradaile and Stupavsky, 1995). After each magnetization, the remanence vector was measured in the absence of an external field using a Minispin slow speed spinner fluxgate magnetometer. Before the application of AR for each position, the remanence of the specimen was cleaned by application of the decaying alternating field, with a peak field of 100 mT. The DC field was applied using a coil controlled by a Molspin P.A.R.M. (Partial

Anhysteretic Remanent Magnetization) attachment connected to the Molspin shielded demagnetizer.

The Spin 1A program provided with the Minispin magnetometer was used to control the operation of the magnetometer and to measure the AR intensity and orientation. Four measurements were made each time with the specimen placed in a different specified orientation within the magnetometer. The results were integrated to give a single measurement of the intensity, inclination and declination of the AR vector in sample coordinates. The results were then converted to geographic co-ordinates using the same program.

The AAR of a specimen is a second-order tensor geometrically represented as an ellipsoid with the principal axes of the ellipsoid corresponding to the maximum (ARmax), intermediate (ARint) and minimum (ARmin) remanent magnetizations. The average anhysteretic remanent magnetization (AR) for a specimen is given by AR = (ARmax + ARint + ARmin)/3. As in AMS the parameters P, L, F and T are used to characterize the magnitude and the shape of the ellipsoid. The parameter P = ARmax/ARmin gives the degree of the anisotropy while L = ARmax/ARint gives the eccentricity of the ellipsoid based on the lineation and F = ARint/ARmin gives the eccentricity of the ellipsoid based on the foliation. The shape of the ellipsoid is given by T = [2(ln(ARint) – ln(ARmin))/(ln(ARmax) – ln(ARmin))] – 1, where T = 1 for purely oblate ellipsoids, T = -1 for purely prolate ellipsoids, and T = 0 for neutral triaxial ellipsoids (Winkler and Sagnotti, 1994). The AAR tensors were calculated using the SI201b program; a magnetic fabric program written by Dr. Graham J. Borradaile (Lakehead University, Thunder Bay, Ontario).

*5.3. Anisotropy of partial Anhysteretic Remanence (ApAR)*

Anisotropy of partial anhysteretic remanence (ApAR) allows for the separation of mineral preferred orientations of different minerals and of different grain size populations of one minerals (i.e. different coercivity fractions) (Day et al., 1977; Jackson et al., 1988). Figure 5.3 shows the strong size-dependence of ApAR of magnetite. The steady direct field of 0.1 mT is only applied over a specific range during the decay of the AF field. Sub-populations of crystals that have coercivities that fall within the chosen AF window may acquire a net remanence while the rest of the mineral population remains demagnetized. In this study, a maximum peak AF of 30 mT was applied in order to limit the net remanence acquisition to the low-coercivity fraction, in this case coarse-grained magnetite. This allows the documentation and analysis of fabrics of different mineral populations in order to separate the signals from "primary" minerals (coarse-grained magnetite) that formed during the emplacement of the dyke from those of "secondary" minerals that formed during the later metamorphism and hydrothermal alteration of the rocks.

The ApAR was determined following an identical procedure to the one outlined in 5.2, with the exception that the bias DF was applied over restricted intervals of the decaying AF. The goal of the ApAR measurements was to isolate the subfabrics defined by coarse grained, soft coercivity magnetite crystals in the samples. The coarse-grained magnetite is interpreted to represent a primary mineral formed during crystallization and emplacement of the Whistle Offset dyke, while the finer grained magnetite crystals are interpreted to be of greenschist-grade, static metamorphic origin. Discrimination of magnetic subfabrics using ApAR was shown to be effective for synthetic samples and sedimentary rocks by Jackson et al. (1988) and it has also been used successfully in igneous rocks by Trinidade et al. (2001).

**Figure 5.3.** ApAR curves for synthetic samples containing magnetite. Responses of the magnetite grains of different sizes are strongly dependent on the range of the applied field. Coarser-grained magnetite reaches peak values at field strengths below 20mT, while finer-grained magnetite grains show peak values at higher applied field strengths. Grain sizes are given in μm. Adapted from Jackson et al., 1988.

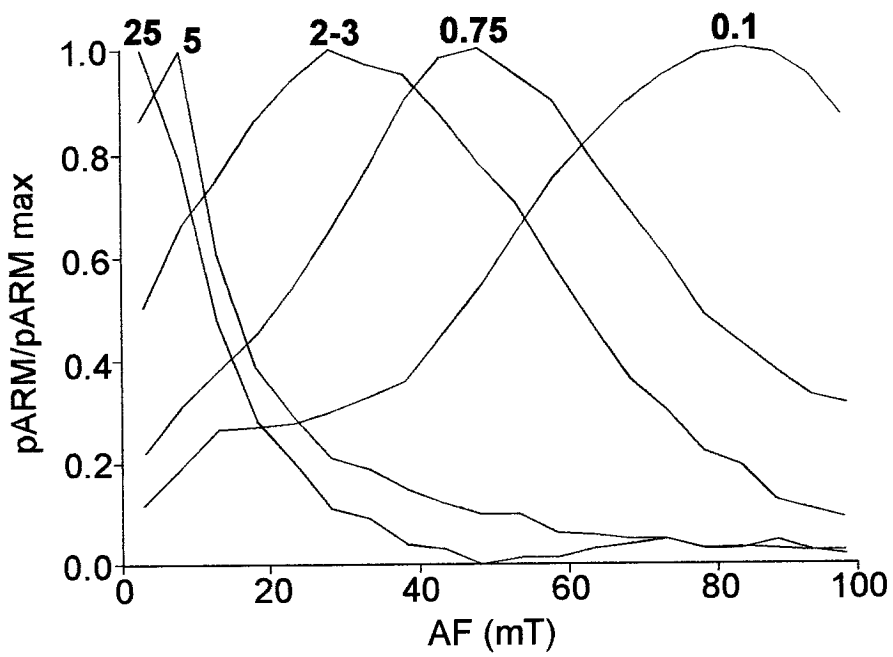


Fig. 5.3.

To determine the optimal interval of the AF decay curve when the bias DF could be applied to remagnetize only the coarser grained, weaker coercivity magnetite crystals, AF acquisition and demagnetization experiments were carried out for specimens from each site. A comparison of AMS, AAR and ApAR fabrics from three test sites was then used to determine the appropriate AF intervals to use for the remaining sites, and also to determine which of these three magnetic anisotropy methods was appropriate to measure the petrofabric at each site.

*5.4. Alternating Field Demagnetization and Acquisition measurements*

Several tests were performed to determine the AF ranges over which to apply the direct field for ApAR measurements. AF demagnetization tests were performed on representative specimens from each of the 20 sites. Partial AR acquisition tests were also performed on 13 of those specimens. Acquisition tests were not performed on specimens from some sites where very similar AF demagnetization curves were obtained for several sites of the same rock type.

Three specimens were then chosen, based on the demagnetization and partial AR acquisition tests, one from each of the three principal rock types: massive sulfides, norite and leucocratic breccia. ApAR was then measured for the three specimens using several different AF intervals. By considering the ApAR results to the AMS, AAR, and AF demagnetization and acquisition curves for the same sites, three different types of magnetic responses were identified. AF intervals for the ApAR of the remaining sites were then based on a comparison of their AF demagnetization and partial AR acquisition curves to those of the three test specimens.

The demagnetization tests involved the application of AR along the axis of a specimen. The remanence was then removed in successive alternating field demagnetization steps of 10 mT. Intensities were normalized to the maximum acquired remanence. For the partial AR acquisition tests, the 0.1 mT direct field was applied over 10-mT interval AF windows. Specimens were subjected to an AF peak demagnetization of 100 mT between each step. The partial AR acquisition was then normalized to the maximum intensity of the acquired remanence.

*5.5. Thermal Demagnetization*

To further investigate the ferromagnetic mineralogy of the sample suite, thermal demagnetization was carried out on 8 specimens (2 sulfide-rich breccia, 1 massive sulfide, 2 norite, 2 leucocratic breccia, and 1 amphibole-quartz diorite sample). The thermal demagnetization was performed in a shielded room, at the Magnetic Research Facility for Tectonic Studies at the paleomagnetics laboratory of the Geological Survey of Canada (GSC), in Ottawa.

Plotting of normalized thermal demagnetization curves allows the identification of the Curie temperatures ($T_C$) for the different ferromagnetic minerals that are present in a specimen. The Curie temperatures for the ferromagnetic minerals are 320°C for pyrrhotite, <575°C for titanomagnetite (highly dependant on the titanium content), 575-585°C for magnetite, and 680°C for hematite.

An anhysteretic remanent magnetization was first applied to each specimen along its axis, using the same procedure as described for the AAR technique. The specimens were then heated to a temperature of 150°C for 60 minutes using a GSC modified version of the Schonstedt model TSD-1 thermal specimen demagnetizer (Schonstedt Instrument Company,

Reston, Virginia). Specimens were allowed to cool and the intensity of the remaining remanence magnetization was measured using a Molspin Spinner Magnetometer. This procedure was repeated with the temperature being increased by 50°C intervals at each step, up to a final temperature of 700°C. Two additional steps were added at 525°C and 575°C as the blocking or Curie temperature ($T_C$) for magnetite was approached ($T_C$ = 575-585°C). At higher temperatures, the heating time was increased to 75 minutes for 600°C, and 90 minutes for 650°C and 700°C.

## Chapter 6: Results I – Magnetic Responses

AR acquisition and AF demagnetization experiments were carried out for one specimen from each of the eight representative sampling sites in order to determine the magnetic responses of the specimens. The magnetic responses are recorded in order to determine the optimal interval of the AF decay curve when the bias DF could be applied for ApAR measurements. The test sites included two sulfide-rich breccias (WL2C1 and WL3D2), an amphibole-quartz diorite (WL4C1), a massive sulfide (WL5C2), two leucocratic breccias (WL7D2 and WL11A3), a leucocratic norite (WL12C2) and a sublayer norite (WL18B1).

From the AR acquisition and AF demagnetization data, three different types of magnetic responses were identified. One example was chosen for each of three types of responses and the data for these type-sites were then compared along with the results for the AMS, AAR and ApAR fabrics for the same sites. The comparison was made in order to determine the optimal intervals of the AF decay curve when the bias DF could be applied to induce partial AR of different coercivity fractions. The AMS, AAR and ApAR of the three sites will be discussed in greater detail in the following chapter in the context of the full data set.

Thermal demagnetization was carried out on the same group of eight specimens that was used for the acquisition and demagnetization experiments. The Curie temperatures, $T_C$, are well known for the ferromagnetic minerals that have previously been identified in the eight specimens through petrographic and SEM studies. The ferromagnetic mineralogy and the principal stable remanence carrier can be more accurately identified for each specimen using thermal demagnetization.

*6.1. Alternating Field (AF) Demagnetization*

The demagnetization data in Fig. 6.1 were obtained by imparting AR along the axis of the cylindrical core specimens and then performing stepwise AF demagnetization, increasing the strength of the AF by 10 mT for each step. The remanence intensities are normalized to the initially acquired intensity in a peak AF field of 100 mT. The normalized intensities are plotted as a function of the peak AF under which the specimens were demagnetized at each step.

The AF demagnetization results reveal three types of magnetic responses. First, WL2C1 (Fig. 6.1A), a sulfide-rich breccia, shows a slight decrease of approximately 20% intensity up to a peak AF field of 20 mT. The response to the AF demagnetization is anomalous, as it does not approach zero intensity. This indicates that the specimen likely did not initially acquire a significant remanence magnetization due to lack of an abundant ferromagnetic component (ARmax = 9.78 mA/m).

The other two types of responses correspond to samples where either only a very soft coercivity fraction is present in the ferromagnetic mineralogy, or to samples that also include a harder coercivity fraction. In the case where there is only a very soft coercivity component, approximately 90% of the AR is cleaned by an AF of 20 mT. This corresponds to specimens WL3D2 (Fig. 6.1B), another sulfide-rich breccia, WL5C2 (Fig. 6.1D), a massive sulfide, WL12C2 (Fig. 6.1G), leucocratic norite, and WL18B1 (Fig. 6.1H), a sublayer norite. In all cases the demagnetization curves for these specimens show a sharp initial drop off in intensity and a near zero intensity above 20 mT.

Specimens WL4C1 (Fig. 6.1C), an amphibole-quartz diorite, WL7D2 (Fig. 6.1E) and WL11A3 (Fig. 6.1F), leucocratic breccias, differ in that they still have a significant hard

**Figure 6.1.** Stepwise AF demagnetization curves with normalized intensity ($AR/AR_{max}$) plotted as a function of the peak alternating field applied at each step.

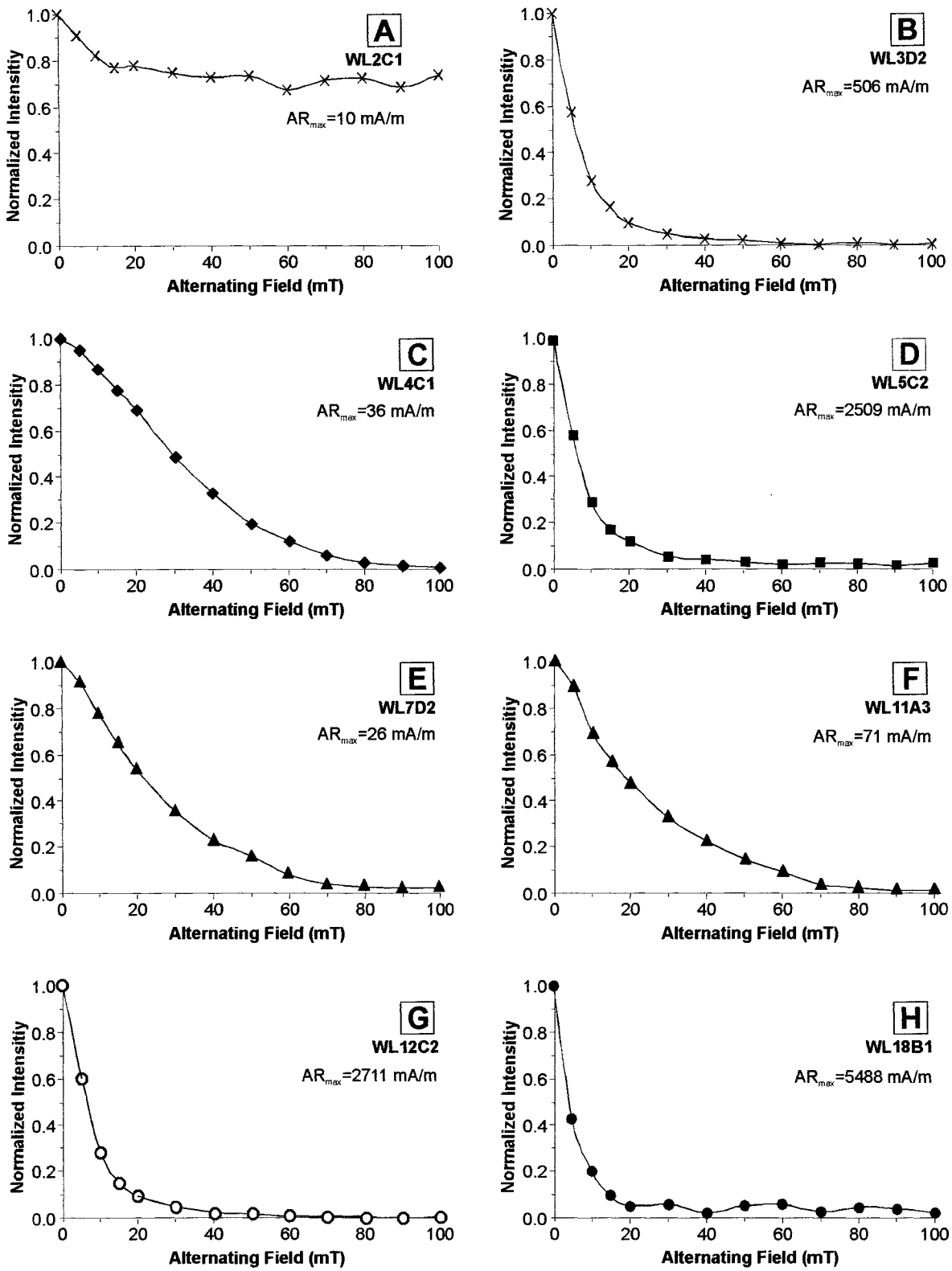
A
WL2C1
AR$_{max}$=10 mA/m
B
WL3D2
AR$_{max}$=506 mA/m
C
WL4C1
AR$_{max}$=36 mA/m
D
WL5C2
AR$_{max}$=2509 mA/m
E
WL7D2
AR$_{max}$=26 mA/m
F
WL11A3
AR$_{max}$=71 mA/m
G
WL12C2
AR$_{max}$=2711 mA/m
H
WL18B1
AR$_{max}$=5488 mA/m
Normalized Intensitiy
Alternating Field (mT)
0.0
0.2
0.4
0.6
0.8
1.0
0
20
40
60
80
100

Fig. 6.1.

coercivity fraction that remains magnetized at 20 mT. An AF of 20 mT cleans only 30-50% of the AR, while approximately 90% of the AR is cleaned by an AF of 60 mT.

Sites with only a very soft coercivity component have higher maximum anhysteretic remanence intensities (ARmax ≈ 500-5500 mA/m) than the sites that also contain a hard coercivity fraction (ARmax ≈ 25-70 mA/m). Petrographic studies have revealed that those sites with only a soft coercivity component have a much higher ferromagnetic mineral content (3-20%) consisting primarily of coarse-grained magnetite ± titanomagnetite and pyrrhotite. Those sites also containing a hard coercivity fraction have a much lower ferromagnetic mineral content (<1-5%) consisting primarily of fine-grained magnetite. Fine-grained magnetite is therefore likely to be the hard coercivity fraction.

*6.2. Partial Anhysteretic Remanence (pAR) Acquisition*

The acquisition data in Fig. 6.2 were generated by sequentially imparting pAR along the core axis for non-overlapping intervals of 10 mT in the decaying AF. The pAR acquired for each interval was cleaned in a maximum 100 mT AF before imparting the pAR for the next interval. The pAR acquisition technique was performed on the same group of specimens used for AF demagnetization, minus specimen WL2C1, the sulfide-rich breccia, which the demagnetization measurements revealed is nearly devoid of remanence bearing minerals.

The pAR acquisition results reveal two types of magnetic responses. The first type of response corresponds to samples where, as with the AF demagnetization, there is only a very soft coercivity component. This type of response corresponds to specimens WL3D2 (Fig. 6.2B), a sulfide-rich breccia, WL5C2 (Fig. 6.2D), a massive sulfide, WL12C2 (Fig. 6.2G), a leucocratic norite, and WL18B1 (Fig. 6.2 H), a sublayer norite. The pAR acquisition curves

**Figure 6.2.** pAR interval acquisition curves with normalized intensity ($pAR/pAR_{max}$) plotted as a function of the AF window over which the d.c. bias field was applied.

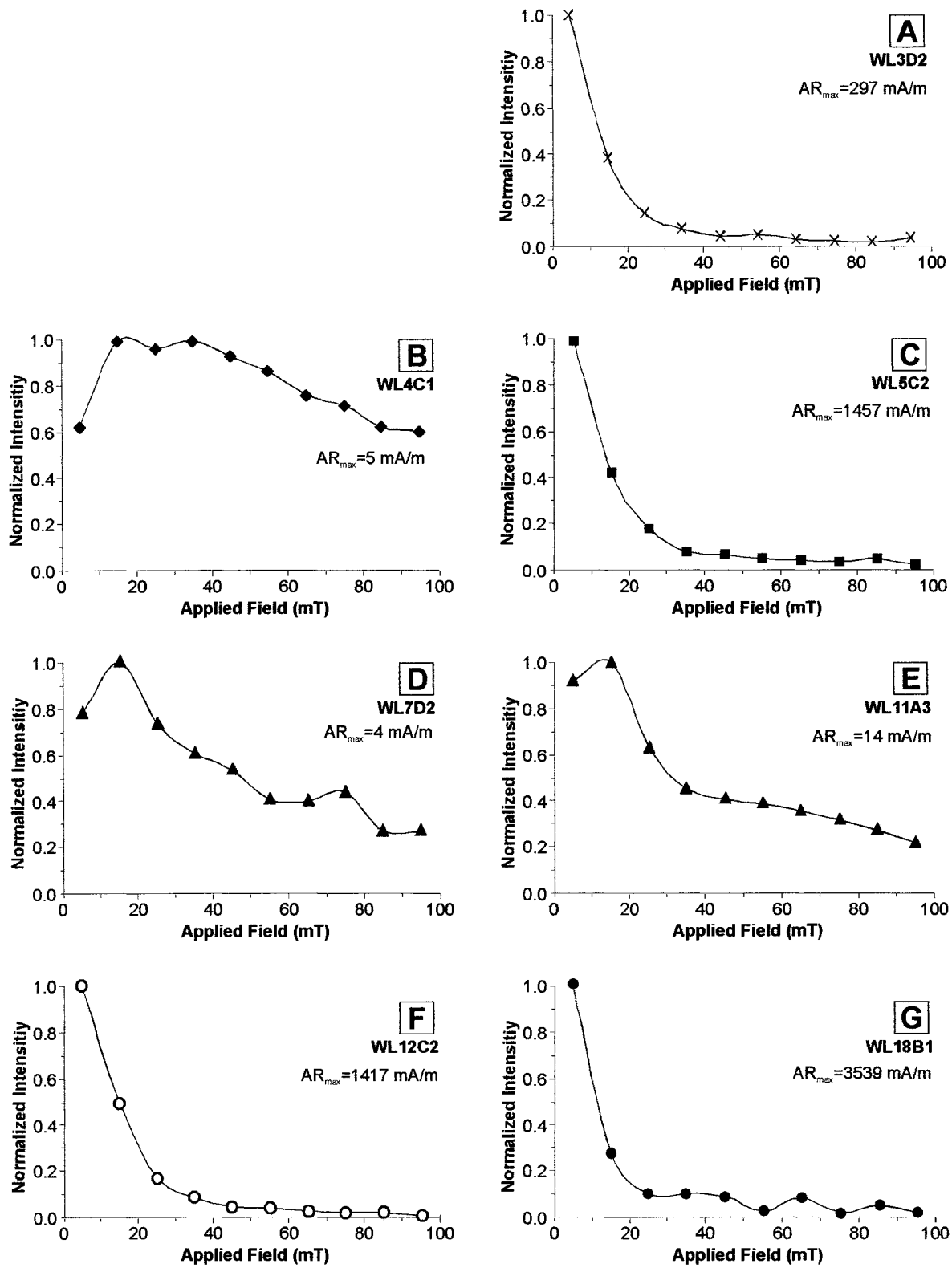
A
WL3D2
AR$_{max}$=297 mA/m
B
WL4C1
AR$_{max}$=5 mA/m
C
WL5C2
AR$_{max}$=1457 mA/m
D
WL7D2
AR$_{max}$=4 mA/m
E
WL11A3
AR$_{max}$=14 mA/m
F
WL12C2
AR$_{max}$=1417 mA/m
G
WL18B1
AR$_{max}$=3539 mA/m
Normalized Intensitiy
Applied Field (mT)

Fig. 6.2.

for these specimens show that the specimens acquire 80% of their anhysteretic remanence with an AF of 20 mT.

The second type of response corresponds to samples where, as with AF demagnetization, there is a hard coercivity component in addition to the soft component. Specimens WL4C1 (Fig. 6.2C), an amphibole-quartz diorite, WL7D2 (Fig. 6.2E) and WL11A3 (Fig. 6.2F), two leucocratic breccias, continue to acquire a significant anhysteretic remanence at peak alternating fields above 20 mT. The greatest pAR acquisition occurs for these specimens over the 20-10 mT interval. A secondary peak in acquisition occurs for specimen WL4C1 over the 40-30 mT interval. In all cases, the curve does not reach an intensity of zero. This is likely due to the continuing pAR acquisition by the hard coercivity fraction, here consisting of fine-grained magnetites and possibly titanomagnetites.

The pAR acquisition data therefore confirm the two principal magnetic response types defines previously using the AF demagnetization, allowing the coercivity populations to be more tightly constrained.

*6.3. Relating coercivity to magnetic anisotropy fabrics*

Fig. 6.3A presents lower-hemisphere equal-area projections of orientation data for the AMS, AAR and ApAR of three representative sampling sites chosen from the eight sites described above. The three representative sites were chosen based on the two types of responses identified in the AF demagnetization and pAR acquisition results. Three types of magnetic response were identified. They *do not* correspond to, but are dependent on, the lithological types. The magnetic responses are the result of both primary and secondary (metamorphic) mineralogy and therefore they are identified only by magnetic characteristics

**Figure 6.3.** Magnetic response type examples. **(6.3A)** AMS, ApAR and AAR subfabrics for specimens WL4C1 (amphibole diorite), WL5C2 (massive sulfide) and WL11A3 (leucocratic breccia). Lower-hemisphere equal-area projections. **(6.3B)** AR demagnetization curves for specimens from the sampling sites in A, plus a specimen from site WL2C1 (sulfide breccia). **(6.3C)** AR acquisition curves. The demagnetization and acquisition curves in 6.3B&C are taken from Fig. 6.1 and Fig. 6.2.

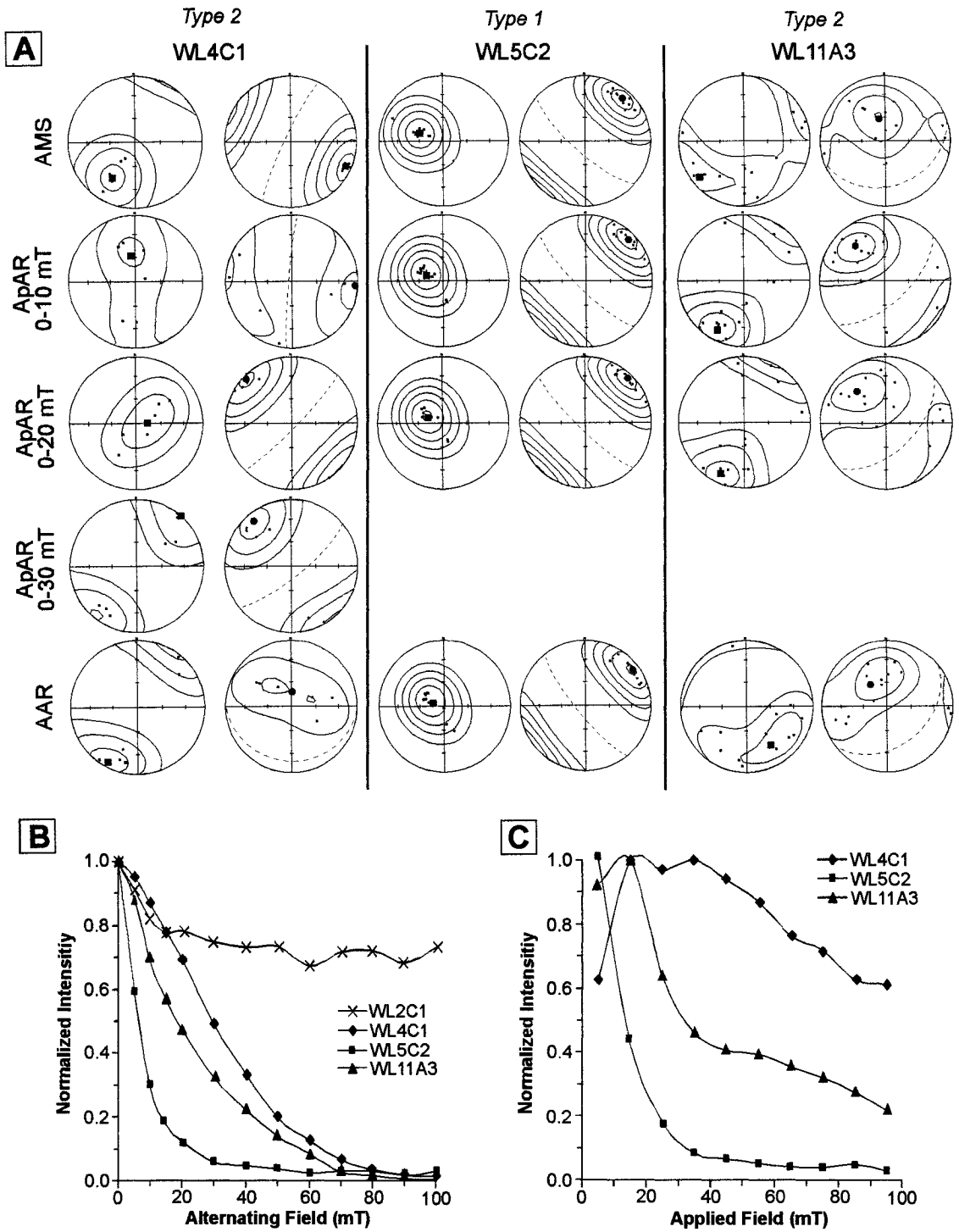
A
Type 2
WL4C1
Type 1
WL5C2
Type 2
WL11A3
AMS
ApAR 0-10 mT
ApAR 0-20 mT
ApAR 0-30 mT
AAR
B
Normalized Intensitiy
Alternating Field (mT)
WL2C1
WL4C1
WL5C2
WL11A3
C
Normalized Intensitiy
Applied Field (mT)
WL4C1
WL5C2
WL11A3

Fig. 6.3.

and not by lithological type. Three types of magnetic response were identified and are described with reference to Figs. 6.3B,C.

*Type 1.* WL5C2 is a representative massive sulfide sample for which AR is ≥ 80% cleaned by an AF of ≤ 20 mT, and ≥ 80% of the AR is acquired within AF intervals ≤ 30 mT (Figs. 6.3B,C). The ferromagnetic mineralogy is predominated by the low coercivity fraction, represented by coarse-grained magnetite, pyrrhotite and titanomagnetite observed in thin sections. For type 1 specimens, the same fabric orientations are measured for AMS, AAR and ApAR (Fig. 6.3A). In this case, it is interpreted that the AMS, the AAR and the ApAR are all dominated by the susceptibility and remanence signals from coarse grained, weak coercivity magnetite, pyrrhotite and titanomagnetite crystals. It is therefore sufficient and more efficient to measure only the AMS in order to resolve the petrofabric orientations in those samples, with type 1 magnetic responses, such as WL5C2.

*Type 2.* WL4C1 (amphibole-quartz diorite) and WL11A3 (leucocratic breccia) represent samples for which a higher coercivity fraction makes a significant contribution to the remanence signal. The higher coercivity fraction consists of fine-grained magnetite, titanomagnetite, and hematite, as identified petrographically and using SEM. Cleaning of ≥ 80% of the AR required an AF > 40 mT. Figs. 6.3 B,C show that for those specimens, a large proportion of the AR is acquired by high coercivity minerals within intervals > 30 mT. For specimen WL11A3, the AMS measurements show a great deal of scatter, likely due to the influence of the higher coercivity fraction, in this specimen represented by fine-grained metamorphic magnetite. A similar, but more well-defined fabric orientation is obtained for the ApAR, when the remanence is acquired at ≤ 20-mT AF. The AAR fabric orientation is most strongly influenced by the metamorphic magnetite, which is remagnetized when the bias direct field is applied over the entire decay range of the AF.

For site WL11 and the sites with similar magnetic responses, the ApAR is thought to provide the best measurement of the rock fabric, when applied over an AF range of 20-0 mT.

Specimen WL4C1 represents a unique case within the sample suite. The AMS fabric is quite well defined, as are the fabrics for the AAR and for the ApAR obtained for the 30-0 mT and 20-0 mT windows of the AF decay field. However, the three magnetic subfabrics are different in orientation. Notably, the magnetic lineations for the AMS, the AAR and the ApAR acquired over the AF range 30-0 mT are all shallowly plunging, whereas the magnetic lineation for the ApAR acquired over the AF range 20-0 mT is subvertical. It is interpreted that the ApAR (20-0 mT) subfabric best isolates the coarse grained magnetite in the sample and is least affected by the higher coercivity mineral fraction that is evidently present, from the data shown in Figs. 6.3B,C.

*Type 3*. The third type of magnetic response corresponds to specimen WL2C1, which is a sulfide-rich breccia from the unique site where the ARav is very weak (7 mA/m; Table 7.2) and only the AMS fabric could be determined. This suggests a near total absence of magnetite and titanomagnetite at that sampling site. Therefore, AMS is used to determine the petrofabric.

### *6.4. Thermal Demagnetization*

In addition to AF demagnetization and pAR acquisition, thermal demagnetization (Fig. 6.4) was used to aid in confirming the mineralogy that contributes to the magnetic remanence. When compared to the AF demagnetization and pAR acquisition results, thermal demagnetization can be used to identify which minerals are controlling the remanence over certain AF ranges. An increase in intensity over higher temperatures for some specimens (Figs. 6.4 A,B,C,E) is likely due to chemical alterations of the specimens occurring at high

**Figure 6.4.** Thermal demagnetization curves with normalized intensity ($AR/AR_{max}$) plotted as a function of temperature (°C). Stereographic projections showing orientations of the AR vector at different heating steps. Lines joining the different measurements show the progression of orientations with a change in temperature. **(6.4A)** WL2C1 = sulfide-rich breccia, **(6.4B)** WL3D2 = sulfide-rich breccia, **(6.4C)** WL4C1 = amphibole-quartz diorite, **(6.4D)** WL5C2 = massive sulfide. Temperatures in °C.

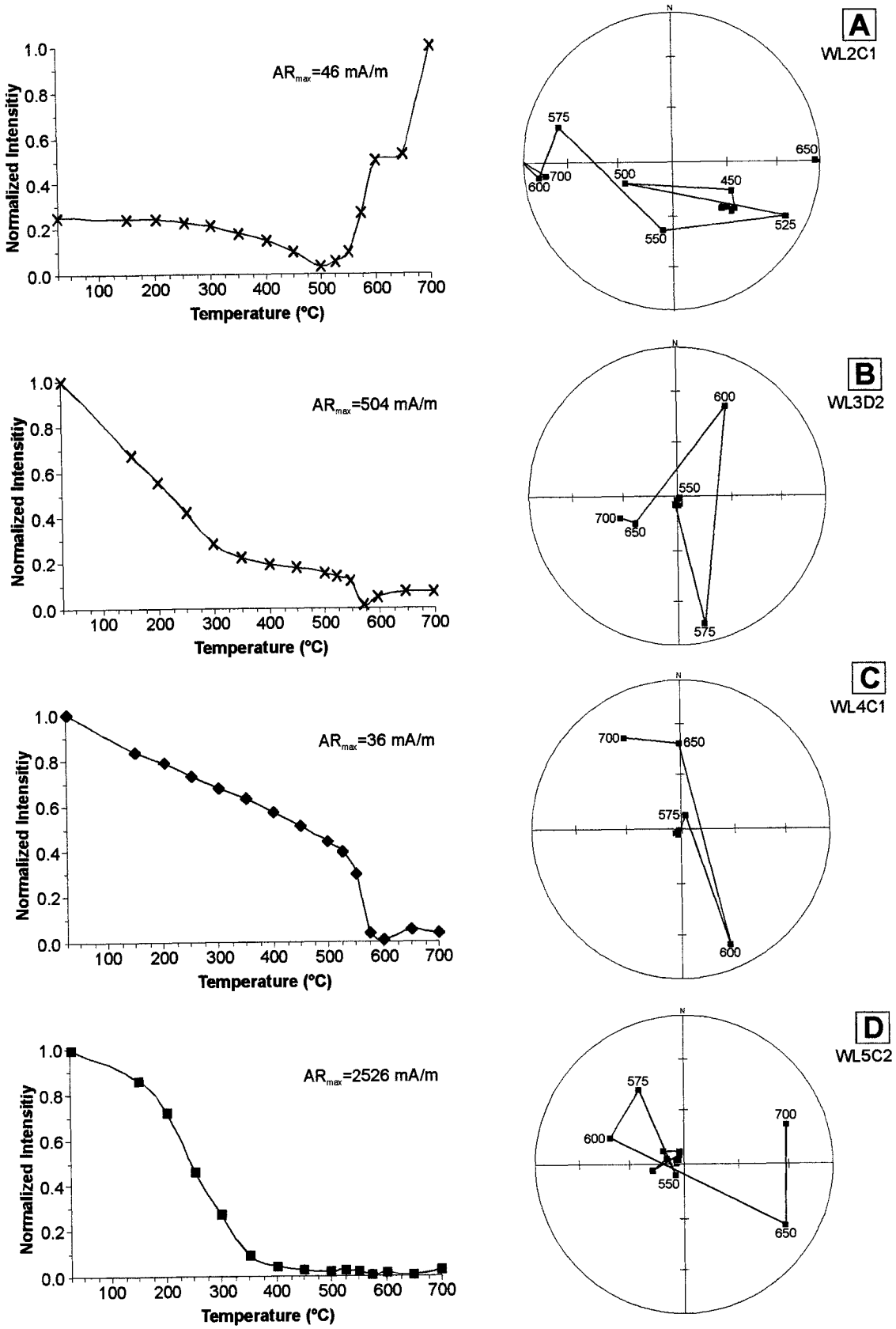
A
WL2C1
AR$_{max}$=46 mA/m
Normalized Intensitiy
Temperature (°C)
575
650
700
600
500
450
525
550
B
WL3D2
AR$_{max}$=504 mA/m
600
550
700
650
575
C
WL4C1
AR$_{max}$=36 mA/m
700
650
575
600
D
WL5C2
AR$_{max}$=2526 mA/m
575
700
600
550
650

Fig. 6.4.

temperatures. The production of secondary magnetite followed by its magnetization in the weak field that is present in a shielded room may be responsible for the remanence at high temperatures.

Specimen WL2C1 (Fig. 6.4A), a sulfide-rich breccia, shows a gradual decrease in normalized intensity up to 500°C due to the presence of titanomagnetite and pyrrhotite. Above 500°C there is an increase in intensity, with a step in the curve at 600°C. The specimen actually acquires a remanence magnetization that is greater in intensity than the originally applied remanent magnetization. The approximately five-fold increase in intensity must be the result of intense chemical alterations. The random orientations of the measured remanence magnetization at temperatures above 450°C (Fig. 6.4A) are also indicative of chemical alterations, most likely the production of fine-grained magnetite and/or titanomagnetite.

Specimen WL3D2 (Fig. 6.4B), another sulfide-rich breccia, shows a gradual decrease in intensity with the curve levelling off at approximately 300°C, indicating the presence of pyrrhotite ($T_C$ = 320°C). A sharp drop in the curve at approximately 575°C indicates the Curie temperature of nearly pure magnetite. A slight increase in intensity at $T \geq 600$°C may be due to minor chemical alterations; this is also indicated by the remanence orientations, which become randomized above temperatures of 550°C.

Specimen WL4C1 (Fig. 6.4C), an amphibole-quartz diorite, shows a gradual decrease in intensity with only one sharp drop in intensity near the blocking temperature of magnetite. The orientations of the measured remanence magnetizations again suggest that the slight increase in intensity above 575°C may be due to minor chemical alterations.

Specimen WL5C2 (Fig. 6.4D), a massive sulfide, has a drop off in intensity between 200 and 350°C. This represents the blocking temperature of pyrrhotite ($T_C$ = 320°C), which

**Figure 6.4 (continued).** Thermal demagnetization curves with normalized intensity ($AR/AR_{max}$) plotted as a function of temperature (°C). Stereographic projections showing orientations of the AR vector at different heating steps. Lines joining the different measurements show the progression of orientations with change in temperature. **(6.4E)** WL7D2 = leucocratic breccia, **(6.4F)** WL11A3 = leucocratic breccia, **(6.4G)** WL12C2 = leucocratic norite, **(6.4H)** WL18B1 = sublayer norite. Temperatures in °C.

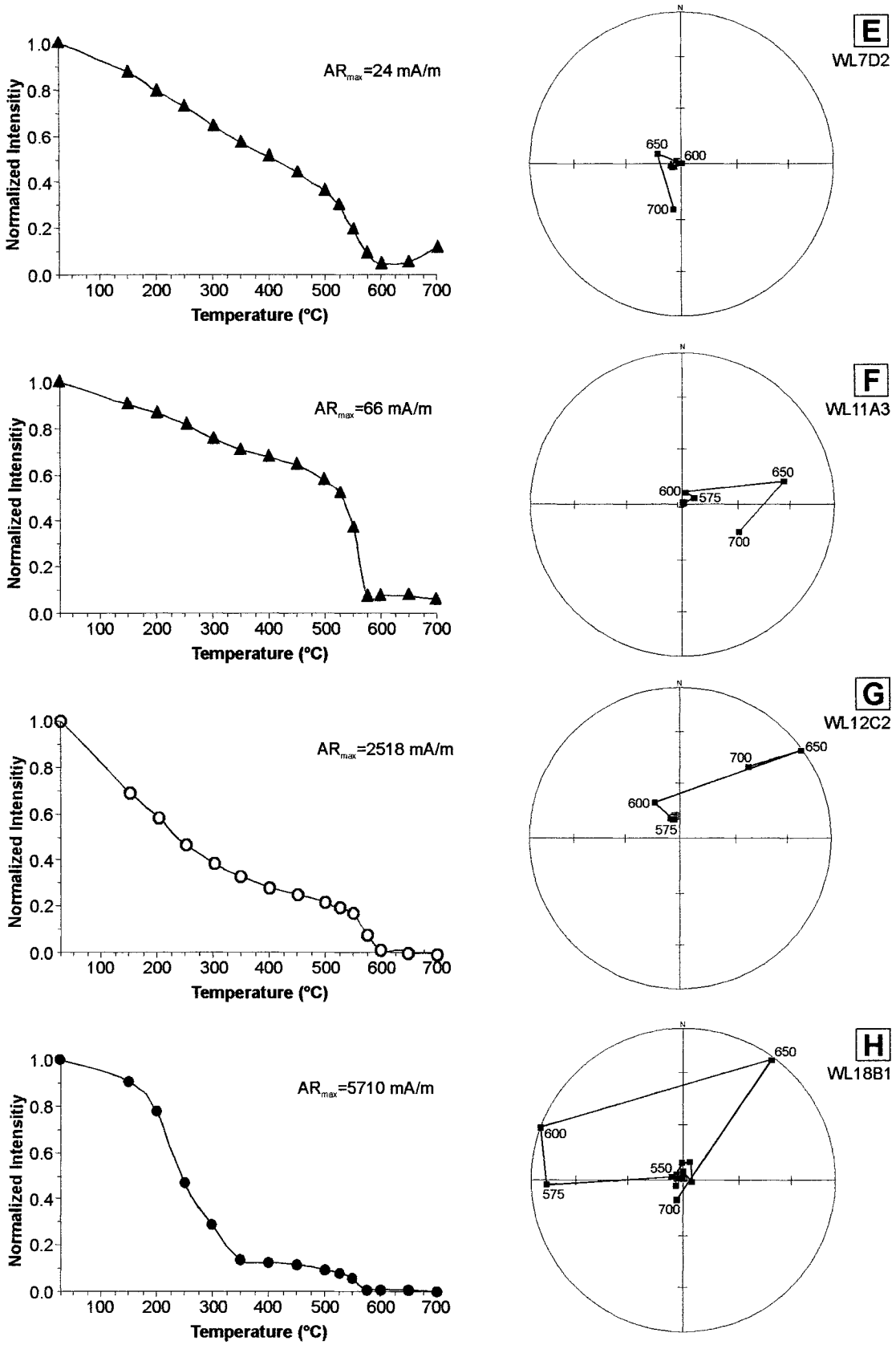
E
WL7D2
AR$_{max}$=24 mA/m
Normalized Intensitiy
Temperature (°C)
650
600
700
F
WL11A3
AR$_{max}$=66 mA/m
650
600
575
700
G
WL12C2
AR$_{max}$=2518 mA/m
700
650
600
575
H
WL18B1
AR$_{max}$=5710 mA/m
650
600
550
575
700

Fig. 6.4. (Cont.)

was identified in petrographic studies, possibly with some contribution from titanomagnetite. There is a small drop in intensity evident at the Curie temperature for nearly pure magnetite, with a randomization of orientations being observed above 550°C.

Specimens WL7D2 (Fig. 6.4E), a leucocratic breccia, displays a gradual decrease in intensity with a sharper decrease in intensity and loss of the remanence vector at ~600°C, indicating the blocking temperature of nearly pure magnetite. The intensity remains slightly above zero above the blocking temperature of magnetite indicating the presence of minor amounts of hematite. A slight increase in intensity above 650°C may be due again to minor chemical alterations. Specimen WL11A3 (Fig. 6.4F), another leucocratic breccia, has a similar curve but shows a sharper drop at the blocking temperature of pure magnetite. Again, a remaining normalized intensity of approximately 10%, above 575°C, indicates the presence of hematite.

Specimen WL12C2 (Fig. 6.4G), a leucocratic norite, shows a slight change in the slope of the curve at $T_C \approx 320$°C indicating the presence of pyrrhotite. There is a sharper drop off in the curve occurring at the Curie temperature for magnetite. There does not appear to be any remaining remanence above the Curie temperature of magnetite.

Specimen WL18B1 (Fig. 6.4H), a sublayer norite, shows a fairly sharp drop off in intensity between 200 and 300°C representing the demagnetization of pyrrhotite plus a Ti-rich titanomagnetite component. Both minerals were identified using SEM. A second drop off at the approximately 575°C indicates the presence of magnetite. A loss of a remanence vector above 550°C indicates an absense of hematite.

The thermal demagnetization responses confirm the 3 types of magnetic responses previously identified using AF demagnetization and pAR acquisition.

*Type 1.* The thermal demagnetization responses for type 1 sites (WL3D2, WL5C2, WL12C2 and WL18B1) reveal that for those sites pyrrhotite and magnetite carry the remanence, with a probable contribution from titanomagnetite. The loss of any stable remanence above 600°C indicates an absence of hematite at these sites.

*Type 2.* For specimens WL4C1 (amphibole-quartz diorite), and WL7D2 and WL11A3 (leucocratic breccia) the only recognizable blocking temperature is 575°C, indicating that the stable remanence carrier for type 2 sites is magnetite. The demagnetization curves do not reveal the presence of any pyrrhotite; however the gradual decrease in intensities below 575°C may be due to variable amounts of titanomagnetite. Specimens WL7D2 and WL11A3 have curves that retain at least 10% of the initial remanence magnetization at temperatures above 575°C and only show minor variations in the orientation of the remanence vector. This indicates that there is a minor hematite component to these specimens. This is not observed for specimen WL4C1.

*Type 3.* The thermal demagnetization response for specimen WL2C1 shows that there is no stable remanence carrier for this sulfide-rich breccia. This suggests a near total absence of magnetite and titanomagnetite at that sampling site. The thermal response is anomalous in that above 450°C there is intense chemical alteration within the specimen, which actually lead to a 400% increase in the intensity of its remanence magnetization. Below 450°C, the specimen does show a slight decrease in intensity, likely indicating the presence of minor amounts of titanomagnetite.

## Chapter 7: Results II - Magnetic Anisotropy Fabrics

Both scalar and directional data are presented for the anisotropy of magnetic susceptibility (AMS), and the anisotropy of total (AAR) and partial (ApAR) anhysteretic remanent magnetization. The scalar data are presented in degree of anisotropy (P) versus average susceptibility ($K_{av}$) diagrams (Fig. 7.1) for AMS, P versus $AR_{av}$ (Fig. 7.5) for AAR, and P versus $pAR_{av}$ (Fig. 7.9) for ApAR. The shape parameter, T, is also plotted as a function of P for AMS (Fig. 7.2), AAR (Fig. 7.6) and ApAR (Fig. 7.10). Site averages for the susceptibilities and remanence values, as well as site averages for the P, T, L, and F values are summarized in Table 7.1 for AMS, Table 7.2 for AAR and Table 7.3 for ApAR. The directional data for the three methods are compared for each site, on maps showing site locations, in Figures 7.3 and 7.4 for AMS, Figures 7.7 and 7.8 for AAR, and Figures 7.11 and 7.12 for ApAR. The average directional data for each site are also summarized in Tables 7.1, 7.2 and 7.3.

### *7.1. Anisotropy of Magnetic Susceptibility (AMS)*

The AMS technique allowed the bulk preferred orientations of paramagnetic and ferromagnetic crystals to be measured (Rochette et al., 1992; Borradaile and Henry, 1997). The extent to which the different paramagnetic and ferromagnetic mineral fractions influence the AMS of the specimens is dependent on the abundance and of the individual mineral species, their intrinsic susceptibility, their intrinsic anisotropy, and the intensity and symmetry of the preferred orientations. The scalar parameters are used along with the measured magnetic responses described in the previous chapter to interpret whether or not

**Table 7.1.** Average AMS data by sampling site.

Table 7.1. Average AMS data by sampling site

| Site | N | Type | Kav x 10-6 (SI) | St Dev | K1 dec/inc | K3 dec/inc | P | T | L | F |
|---|---|---|---|---|---|---|---|---|---|---|
| WL1m | 12 | MS | 95257 | 45913 | 237/45 | 137/10 | 1.40 | 0.20 | 1.128 | 1.239 |
| WL1d | 7 | SB | 4378 | 4114 | 304/51 | 167/30 | 1.05 | -0.18 | 1.027 | 1.020 |
| WL2 | 14 | SB | 520 | 49 | 099/63 | 321/21 | 1.06 | -0.36 | 1.038 | 1.018 |
| WL3 | 14 | SB | 47157 | 37267 | 247/35 | 030/49 | 1.04 | 0.38 | 1.014 | 1.031 |
| WL4 | 6 | AD | 555 | 18 | 210/34 | 116/07 | 1.02 | 0.34 | 1.007 | 1.014 |
| WL5 | 11 | MS | 53427 | 17646 | 284/61 | 041/14 | 1.44 | -0.05 | 1.189 | 1.207 |
| WL6 | 16 | MS | 62170 | 15048 | 144/85 | 023/02 | 1.36 | 0.75 | 1.034 | 1.312 |
| WL7 | 11 | LB | 617 | 209 | 210/61 | 066/24 | 1.03 | 0.42 | 1.009 | 1.023 |
| WL8 | 10 | MN | 72310 | 5393 | 060/35 | 150/00 | 1.09 | -0.22 | 1.052 | 1.035 |
| WL9 | 7 | LB | 1384 | 367 | 166/09 | 268/53 | 1.01 | -0.25 | 1.007 | 1.004 |
| WL10 | 10 | LB | 1134 | 191 | 210/04 | 117/40 | 1.01 | -0.31 | 1.006 | 1.003 |
| WL11 | 13 | LB | 5941 | 15751 | 236/15 | 347/54 | 1.02 | 0.29 | 1.008 | 1.015 |
| WL12 | 11 | MN | 108248 | 11290 | 000/28 | 132/52 | 1.21 | 0.31 | 1.063 | 1.135 |
| WL13 | 9 | LB | 23927 | 44968 | 024/59 | 277/10 | 1.03 | 0.29 | 1.012 | 1.022 |
| WL14 | 10 | LB | 703 | 264 | 011/11 | 102/04 | 1.01 | 0.52 | 1.002 | 1.006 |
| WL15 | 8 | LB | 718 | 182 | 267/66 | 082/24 | 1.01 | 0.45 | 1.002 | 1.005 |
| WL16 | 11 | LB | 1088 | 423 | 080/69 | 285/19 | 1.01 | 0.51 | 1.004 | 1.011 |
| WL17 | 13 | SN | 68128 | 55976 | 009/43 | 107/09 | 1.05 | 0.06 | 1.023 | 1.027 |
| WL18 | 7 | SN | 74010 | 47607 | 257/17 | 165/07 | 1.07 | -0.11 | 1.041 | 1.033 |
| WL19 | 9 | SN | 71867 | 6501 | 254/13 | 100/76 | 1.05 | 0.55 | 1.011 | 1.040 |

N=number of specimens; Type=rock type: massive sulfide (MS), sulfide-rich breccia (SB), amphibole-quartz diorite (AD), leucocratic breccia (LB), mafic norite (MN), sublayer norite (SN), leucocratic norite (LN); Kav=mean volume susceptibility in SI units; ST DEV=standard deviation of Kav; Dec/Inc=declination and inclination in degrees; P=degree of anisotropy; T= shape of the susceptibility ellipsoid; eccentricity of the ellipsoid based on magnetic lineation (L) and magnetic foliation (F).

the subfabrics measured are primary, thereby representing the kinematics of emplacement, or are masked by secondary metamorphic minerals.

*Scalar parameters:* The massive sulfide specimens (Fig. 7.1A) have high average susceptibility ($K_{av}$) values, which range from ~30,000 x $10^{-6}$ SI to ~150,000 x $10^{-6}$ SI. The high $K_{av}$ values indicate that the ferromagnetic minerals make an overwhelming contribution to the susceptibility of the specimens, swamping the signal from the paramagnetic minerals. Based on the thermal demagnetization and petrographic studies (sections 3.6, 6.4), the principal ferromagnetic components are magnetite and pyrrhotite ± titanomagnetite. The degree of anisotropy, P, is most highly variable for the massive sulfide specimens, ranging from 1.19 to 1.94. The large variation is interpreted to indicate a difference in the volume of pyrrhotite in different specimens (1-5%). Pyrrhotite has a very higher intrinsic susceptibility anisotropy (P > 100; Tarling and Hrouda, 1993); therefore it will have a strong influence on the measured degree of anisotropy. Neither the P nor the $K_{av}$ values are site dependent, as within-site variations are equal to between-site variations.

Sulfide-rich breccia specimens (Fig 7.1B) have $K_{av}$ values ranging from ~400 x $10^{-6}$ SI to ~150,000 x $10^{-6}$ SI. The large variation in $K_{av}$ values is interpreted to be due to variations in magnetite abundance between specimens and sites; sites with lower magnetite contents (1% for WL1d, <1% for WL2) have lower $K_{av}$ values, while site WL3, which contains an estimated 15% magnetite, has the highest $K_{av}$ values. $K_{av}$ values are therefore strongly site dependent for the sulfide-rich breccia. The range of P values is more restricted for the sulfide-rich breccia specimens than for the massive sulfide specimens and P values are much lower (1.01-1.19) than those for the massive sulfides. This reflects a lower pyrrhotite content (<1% observed in thin sections) for the sulfide-rich breccia specimens.

**Figure 7.1.** Scalar parameters for AMS. Degree of anisotropy (P) plotted as a function of average magnetic susceptibility ($K_{av}$) of the specimen. **(7.1A)** PK plots for massive sulfide sites. **(7.1B)** Sulfide-rich breccia. **(7.1C)** Amphibole-quartz diorite. **(7.1D)** Leucocratic breccia. **(7.1E)** Mafic and leucocratic norites. **(7.1F)** Sublayer norite.

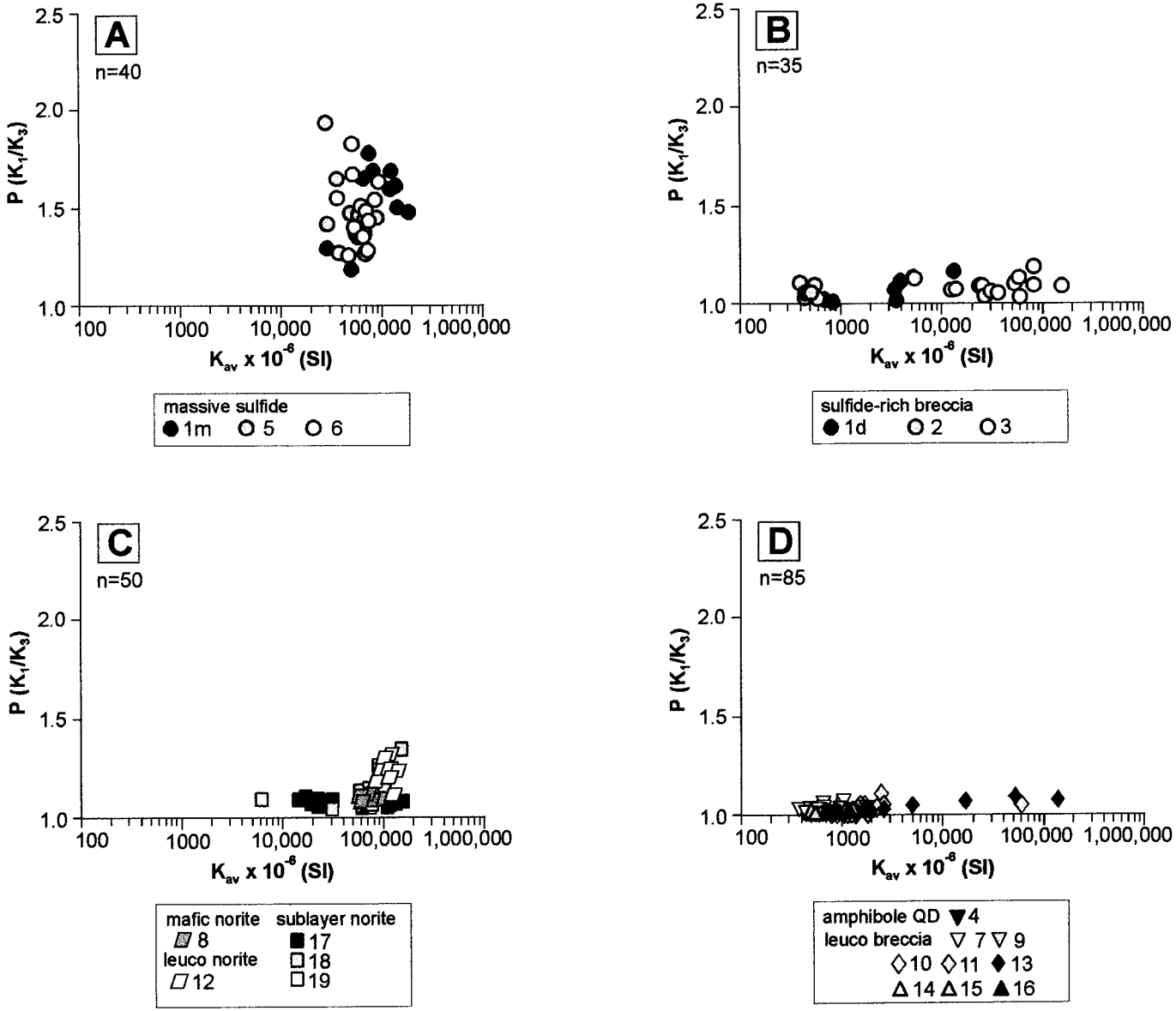
A
n=40
P (K1/K3)
Kav x 10-6 (SI)
massive sulfide
1m 5 6
B
n=35
sulfide-rich breccia
1d 2 3
C
n=50
mafic norite 8
leuco norite 12
sublayer norite 17 18 19
D
n=85
amphibole QD 4
leuco breccia 7 9 10 11 13 14 15 16

Fig. 7.1.

Noritic specimens, including the sublayer, leucocratic and mafic norites (Fig 7.1C), have high $K_{av}$ values (~6,000 x $10^{-6}$ SI to ~150,000 x $10^{-6}$ SI), similar to the massive sulfides, reflecting a high magnetite (1-15%) content and to a lesser degree, the presence of pyrrhotite (1-5%). The greatest variation in $K_{av}$ values occurs for sublayer norite sites WL17 and WL18. P values for the norites are also variable, ranging from 1.04 to 1.34, with the greatest variation occuring for sites WL12 and WL18.

Amphibole-quartz diorite and leucocratic breccia specimens (Fig. 7.1D) have $K_{av}$ values ranging from ~400 x $10^{-6}$ SI to ~140,000 x $10^{-6}$ SI, though most specimens have $K_{av}$ < 500,000 x $10^{-6}$ SI. The large variation is for two sites, WL11 and WL13, where it is interpreted to be due to variation in the abundance of Fe-Ti oxides in different specimens. The large variations are also responsible for large standard deviations of $K_{av}$ for those sites (Table 7.1). The range of P values is more restricted for the leucocratic breccia and amphibole-quartz diorite specimens (1.00-1.10 for AMS; Fig. 7.1D). Low P values may be due to the absence of abundance of pyrrhotite for these sites, as determined by petrography and thermal demagnetization (sections 3.4, 6.4; pyrrhotite only identified for site WL11).

The shape parameter T is plotted as a function of P in Figure 7.2, for AMS. Dominantly oblate magnetic fabrics (T>0) are recorded for the massive sulfide sites WL1m and WL6 (Fig. 7.2A), as all specimens have T values greater than zero. The oblate dominant fabric likely represents the influence of pyrrhotite, which has a highly intrinsic oblate anisotropy (Uyeda, Fuller et al. 1963). There is no relationship between the degree of anisotropy and the ellipsoid shape. The sulfide-rich breccia specimens have a broad range of ellipsoid shapes, with T values ranging from quite prolate (-0.8) to quite oblate (~0.8) (Fig. 7.2B). Of the norites (Fig. 7.2C), site WL8 has a dominantly prolate shape, while site WL12 is dominantly oblate. The three sublayer norite sites show no predominant shape. Noritic

**Figure 7.2.** Scalar parameters for AMS. Shape parameter (T) plotted as a function of the degree of anisotropy (P). **(7.2A)** PT plots for massive sulfide sites. **(7.2B)** Sulfide-rich breccia. **(7.2C)** Amphibole-quartz diorite. **(7.2D)** Leucocratic breccia. **(7.2E)** Mafic and leucocratic norites. **(7.2F)** Sublayer norite.

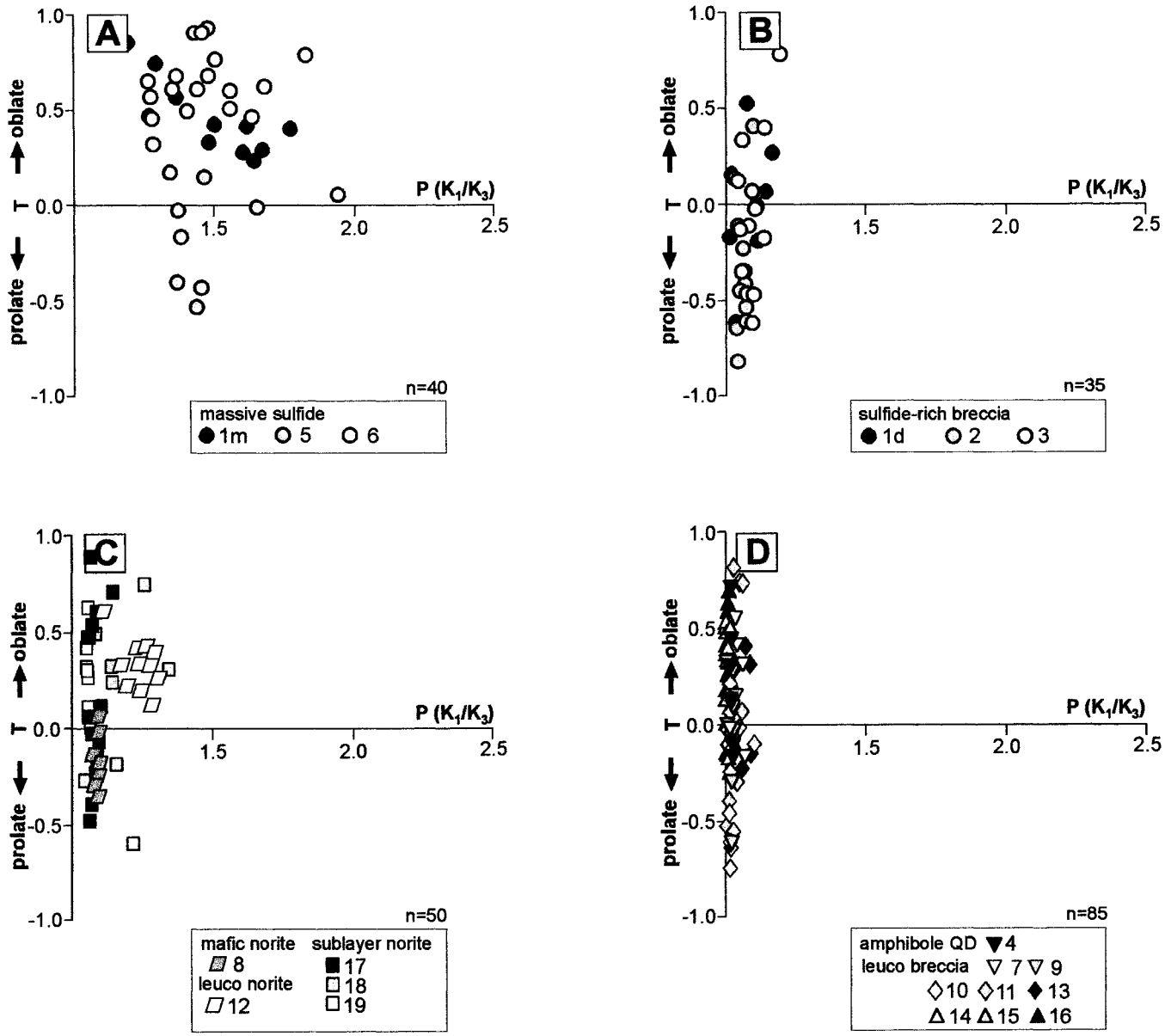
A
B
C
D
T
oblate
prolate
P (K1/K3)
1.0
0.5
0.0
-0.5
-1.0
1.5
2.0
2.5
n=40
massive sulfide
1m 5 6
n=35
sulfide-rich breccia
1d 2 3
n=50
mafic norite 8
leuco norite 12
sublayer norite 17 18 19
n=85
amphibole QD 4
leuco breccia 7 9 10 11 13 14 15 16

Fig. 7.2.

specimens with higher P values tend to correspond to oblate magnetic fabrics. The amphibole-quartz diorite and leucocratic breccia sites (Fig. 7.2D) show no obviously dominant ellipsoid shapes.

*Directional data:* Equal-area projections of the directional data are shown for each site in Figure 7.3 (embayment and proximal offset) and Figure 7.4 (the North Zone).

Sublayer and leucocratic norite sites within the embayment (Fig.7.3) exhibit *Type 1* magnetic responses. The AMS fabrics recorded at these sites are controlled primarily by coarse-grained magnetite ± pyrrhotite and therefore are expected to represent a primary magmatic fabric, related to emplacement of the noritic magma. Paramagnetic Fe-silicate minerals will not contribute significantly to the fabrics as their signal are overwhelmed by the high intensities of the ferromagnetic mineral fraction ($K_{av}$ values > 50,000 x $10^{-6}$ SI).

Samples of sublayer norite from the Whistle embayment (Fig. 7.3) have a horizontal magnetic foliation towards the centre of the embayment (WL19). The foliation becomes steeper approaching the outer wall of the embayment (WL18), and finally near vertical, striking approximately N-S (WL17) near the contact of the embayment with the dyke wall. Magnetic lineations are near horizontal towards the centre of the embayment and trend roughly parallel to the NE-SW strike of the dyke. Near the dyke wall, the magnetic lineation plunges more steeply and trends roughly parallel to the strike of the dyke. The leucocratic norite site, WL12, shows a N trending horizontal lineation and SW striking, moderately dipping foliation that is similar to site WL17.

Leucocratic breccia sites within the proximal Whistle dyke (Fig. 7.3) exhibit *Type 2* magnetic responses indicating that the primary ferromagnetic component contributing to the AMS fabric is magnetite, which may be either coarse- or fine-grained. $K_{av}$ values generally <

**Figure 7.3.** AMS fabric map for the Whistle embayment and the proximal Whistle Offset dyke. Equal-area projections of K1 (squares) and K3 (circles). The magnetic foliation plane for each site is shown as a dashed great circle. Orientations for individual specimens (small symbols) and the site average (large symbols) are shown. The orientation of the nearby dyke wall is shown as a solid black line. Location of Fig. 7.4 is indicated. Base map provided by FNX Mining Company Ltd.

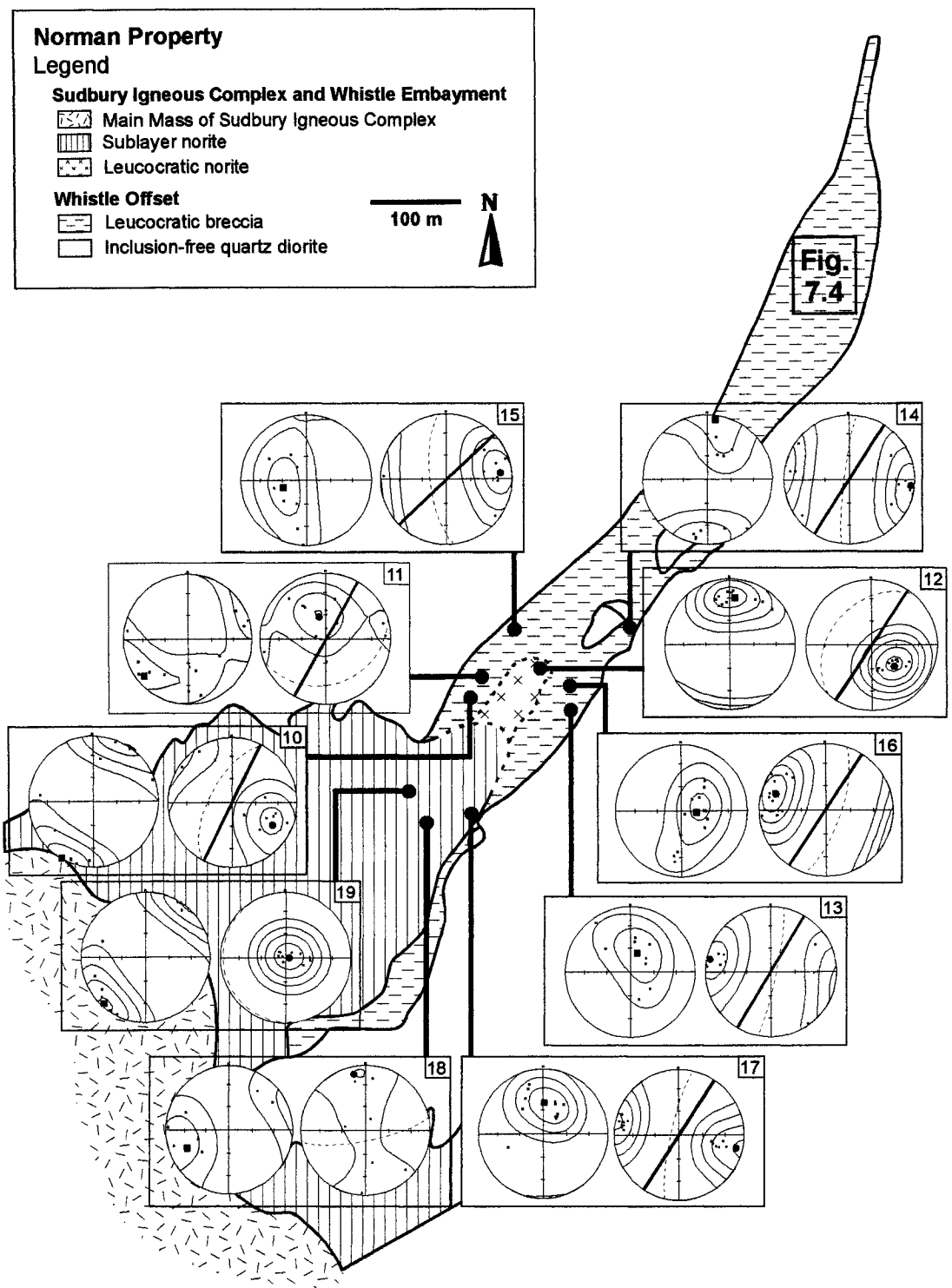
Norman Property
Legend
Sudbury Igneous Complex and Whistle Embayment
Main Mass of Sudbury Igneous Complex
Sublayer norite
Leucocratic norite
Whistle Offset
Leucocratic breccia
Inclusion-free quartz diorite
100 m
N
Fig. 7.4
15
14
11
12
10
16
19
13
18
17

Fig. 7.3.

5000 x $10^{-6}$ SI suggest that the paramagnetic component (biotite, pyroxenes, chlorite and Ca-Fe amphibole) may also contribute significantly to the AMS for these sites (Tarling and Hrouda, 1993).

Within the proximal Whistle Offset dyke, the magnetic foliations are mostly steeply dipping and strike obliquely to the dyke walls. Site WL11 has a shallowly dipping foliation, but the fabric is poorly defined, possible due to the presence of fine-grained metamorphic magnetite. There are two groups of fabrics based on lineations: The first group of sites (WL10, WL11, and WL14) has horizontal lineations trending N-S to NE-SW. These lineations are in accordance with the expected orientations in the case of flow during emplacement of the dyke. In the second group, the sites (WL13, WL15, and WL16) have near vertical lineations, highly discordant to the horizontal lineations at the other sites. A simple model of emplacement flow within a dyke cannot explain the vertical lineations.

Within the distal Whistle Offset (Fig. 7.4), sites displaying all three types of magnetic responses are present. *Type 1* massive sulfide sites record steeply dipping magnetic foliations that strike NE-SW (sites WL1m and WL1d) or NW-SE (sites WL5 and WL6). Magnetic lineations for sites WL5 and WL6 are near vertical. For sites WL1m and WL1d, the lineations plunge moderately and trend to the SW and NW respectively. The sulfide-rich breccia site WL3 has a shallowly dipping foliation and a W-trending horizontal lineation. For sites with *Type 2* magnetic responses (WL4, WL7, and WL9), both a ferromagnetic component (magnetite) plus a paramagnetic component contributed to the fabric signal. The AMS fabric for WL4 is very similar to WL1m, while that of site WL7 is similar to sites WL5 and WL6. Site WL9 has a well-defined N-S trending horizontal lineation but a poorly defined N striking subvertical magnetic foliation, with the $K_3$ poles defining a girdle distribution. Sulfide-rich breccia site WL2 exhibits a *Type 3* magnetic response, indicating an

**Figure 7.4.** AMS fabric map of the distal Whistle Offet dyke where the North deposit outcrops. Equal-area projections of K1 (squares) and K3 (circles). The magnetic foliation plane for each site is shown as a dashed great circle. Orientations for individual specimens (small symbols) and the site average (large symbols) are shown. The approximate orientation of the dyke wall is shown as a solid black line. Approximate Location of this map is shown in Fig. 7.3. Base map provided by FNX Mining Company Ltd.

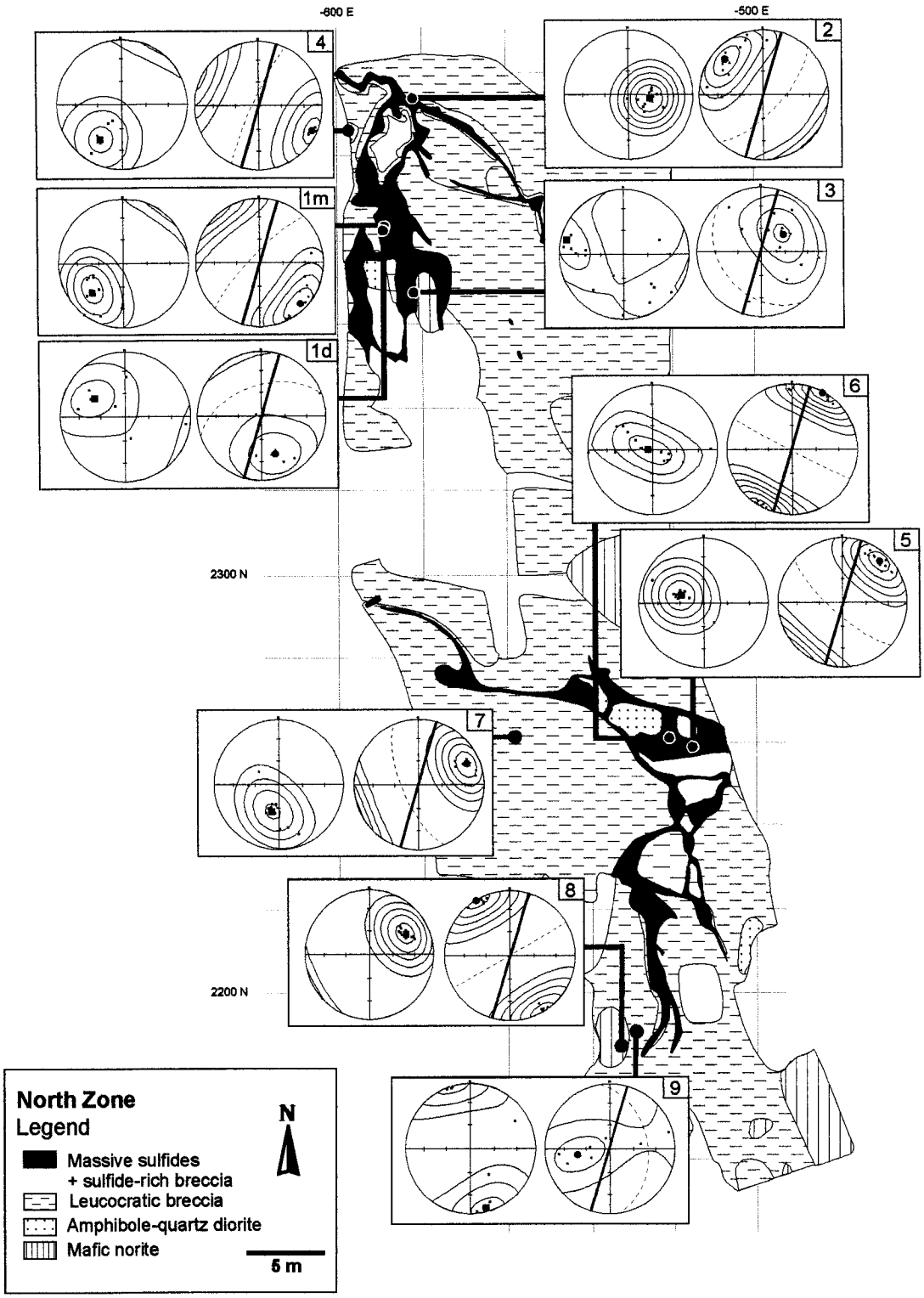
-600 E
-500 E
4
2
1m
3
1d
6
5
2300 N
7
8
2200 N
9
North Zone
Legend
N
Massive sulfides
+ sulfide-rich breccia
Leucocratic breccia
Amphibole-quartz diorite
Mafic norite
5 m

Fig. 7.4.

**Table 7.2.** Average AAR data by sampling site.

Table 7.2. Average total AAR data by sampling site

| Site | N | Type | ARav (mA/m) | St Dev | ARmax dec/inc | ARmin dec/inc | P | T | L | F |
|---|---|---|---|---|---|---|---|---|---|---|
| WL1m | 12 | MS | 1152 | 523 | 236/44 | 131/12 | 1.83 | 0.38 | 1.22 | 1.50 |
| WL1d | 7 | SB | 87 | 61 | 117/03 | 201/23 | 1.32 | 0.00 | 1.12 | 1.18 |
| WL2 | 14 | SB | 7* | - | - | - | - | - | - | - |
| WL3 | 14 | SB | 778 | 861 | 304/02 | 024/32 | 1.41 | -0.04 | 1.18 | 1.19 |
| WL4 | 6 | AD | 38 | 3 | 209/09 | 003/72 | 1.14 | -0.18 | 1.08 | 1.05 |
| WL5 | 11 | MS | 2190 | 567 | 285/75 | 051/12 | 1.46 | -0.02 | 1.22 | 1.20 |
| WL6 | 16 | MS | 4264 | 996 | 229/88 | 033/03 | 1.62 | 0.50 | 1.13 | 1.43 |
| WL7 | 11 | LB | 49 | 64 | 013/04 | 350/84 | 1.26 | 0.04 | 1.12 | 1.12 |
| WL8 | 10 | MN | 4784 | 269 | 069/32 | 159/04 | 1.24 | 0.19 | 1.09 | 1.14 |
| WL9 | 7 | LB | 94 | 24 | 014/14 | 269/55 | 1.14 | 0.18 | 1.06 | 1.08 |
| WL10 | 10 | LB | 62 | 12 | 296/09 | 170/81 | 1.14 | -0.04 | 1.07 | 1.06 |
| WL11 | 13 | LB | 293 | 683 | 149/31 | 322/52 | 1.17 | 0.01 | 1.08 | 1.09 |
| WL12 | 11 | MN | 3471 | 439 | 005/23 | 124/58 | 1.61 | 0.37 | 1.16 | 1.38 |
| WL13 | 9 | LB | 275 | 438 | 336/37 | 089/15 | 1.15 | 0.25 | 1.04 | 1.10 |
| WL14 | 10 | LB | 30 | 9 | 335/25 | 218/45 | 1.14 | 0.14 | 1.06 | 1.07 |
| WL15 | 8 | LB | 39 | 6 | 293/07 | 202/43 | 1.08 | -0.29 | 1.05 | 1.03 |
| WL16 | 11 | LB | 44 | 13 | 076/07 | 297/82 | 1.12 | -0.04 | 1.06 | 1.05 |
| WL17 | 13 | SN | 3584 | 3282 | 351/69 | 096/12 | 1.18 | 0.34 | 1.05 | 1.12 |
| WL18 | 7 | SN | 7274 | 5342 | 261/25 | 004/33 | 1.44 | -0.19 | 1.26 | 1.14 |
| WL19 | 9 | SN | 3778 | 1061 | 227/07 | 092/77 | 1.18 | 0.27 | 1.07 | 1.10 |

*single specimen result
N=number of specimens; Type=rock type: massive sulfide (MS), sulfide-rich breccia (SB), amphibole-quartz diorite (AD), leucocratic breccia (LB), mafic norite (MN), sublayer norite (SN), leucocratic norite (LN); ARav = mean anhysteretic remanence magnetization in mA/m; ST DEV=standard deviation of Arav; Dec/Inc=declination and inclination in degrees; P= degree of anisotropy; T=shape of the remanence ellipsoid; eccentricity of the ellipsoid based on magnetic lineation (L) and magnetic foliation (F).

absence of a ferromagnetic component in the AMS signal. Paramagnetic Fe-silicate minerals must therefore control the well-defined, near vertical NE-SW striking magnetic foliation and a NE trending subvertical magnetic lineation measured for that site. Mafic norite site WL8 is very similar to WL2 with well-defined near vertical NE-SW striking foliations and subhorizontal NE trending lineations.

*7.2. Anisotropy of Anhysteretic Remanence (AAR)*

AAR was used to measure the magnetic fabrics defined by the ferromagnetic minerals in the sample suite. The ferromagnetic mineralogy includes coarse-grained magnetite, thought to represent a primary, magmatic mineral, pyrrhotite, and fine-grained magnetite of probable metamorphic origin.

*Scalar parameters:* Average anhysteretic remanence ($AR_{av}$) values for the massive sulfide specimens (Fig. 7.5A) range from ~500 mA/m to ~6500 mA/m. Higher values indicate relatively abundant ferromagnetic minerals in the massive sulfide specimens. The degree of anisotropy, P, is highly variable for the massive sulfide specimens, ranging from 1.70 to 2.39. Slightly higher values than for the AMS (compare to Fig. 7.1A) are likely due to the coarse-grained (single-domain) magnetite crystals, as they are expected to exhibit much larger particle anisotropies for remanent magnetization than for susceptibility (Stephenson et al., 1986).

The sulfide-rich breccia specimens (Fig. 7.5B) have generally lower $AR_{av}$ values (~30 mA/m to ~3200 mA/m) than the massive sulfides due to the lower abundances of ferromagnetic minerals in the breccia. $AR_{av}$ values are higher for site WL3, which contains up to 15% magnetite (section 3.7). Results are not available for site WL2, which has a very weak remanence signal ($AR_{av}$ values ~7 mA/m; Table 7.2), due to a lack of a significant

**Figure 7.5.** Scalar parameters for AAR. Degree of anisotropy (P) plotted as a function of average anhysteretic remanence ($AR_{av}$) of the specimen. **(7.5A)** P vs $AR_{av}$ plots for massive sulfide sites. **(7.5B)** Sulfide-rich breccia. **(7.5C)** Amphibole-quartz diorite. **(7.5D)** Leucocratic breccia. **(7.5E)** Mafic and leucocratic norites. **(7.5F)** Sublayer norite.

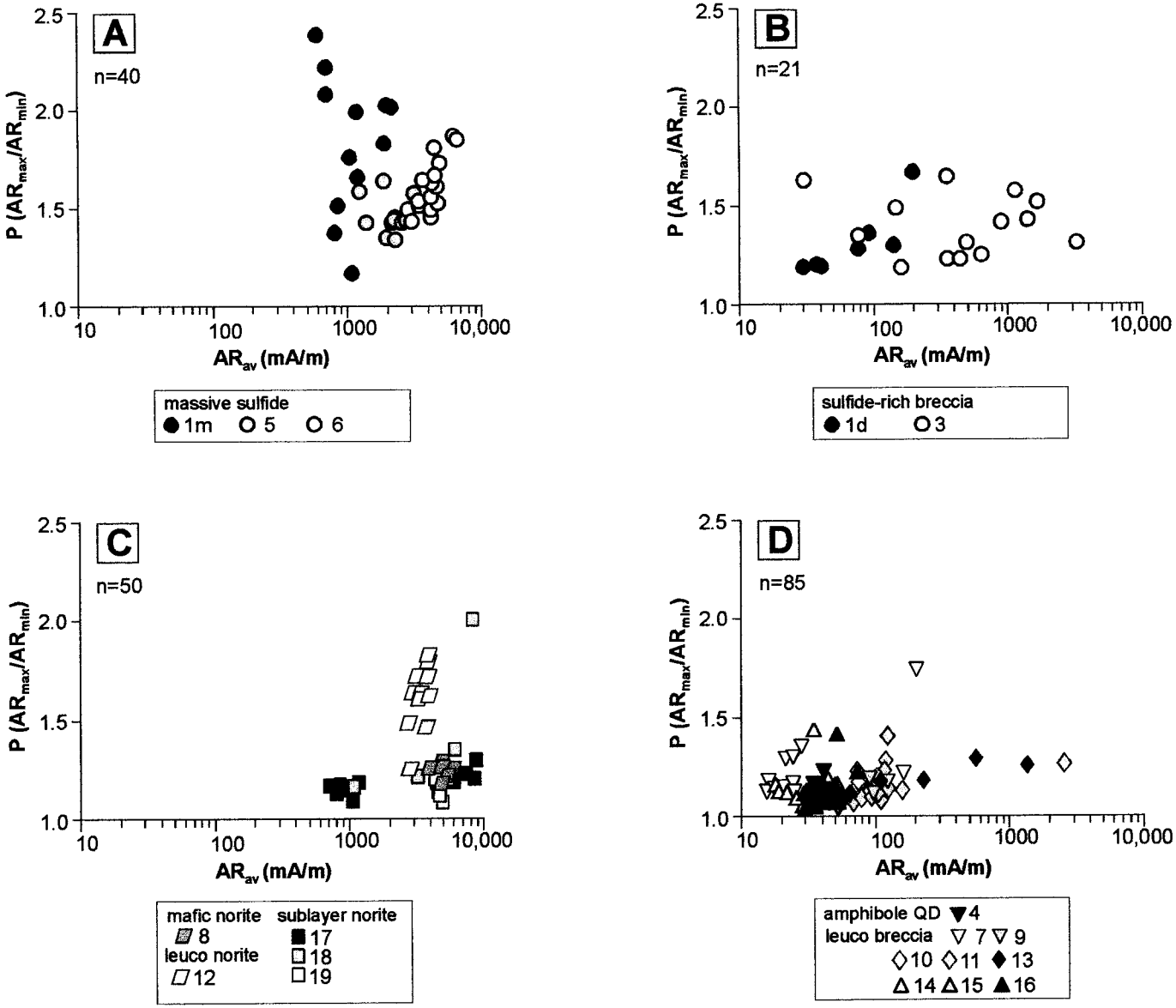
A
n=40
B
n=21
C
n=50
D
n=85
P (ARmax/ARmin)
ARav (mA/m)
2.5
2.0
1.5
1.0
10
100
1000
10,000
massive sulfide
1m 5 6
sulfide-rich breccia
1d 3
mafic norite 8
leuco norite 12
sublayer norite 17 18 19
amphibole QD 4
leuco breccia 7 9 10 11 13 14 15 16

Fig. 7.5.

**Figure 7.6.** Scalar parameters for AAR. Shape parameter (T) plotted as a function of the degree of anisotropy (P). **(7.6A)** PT plots for massive sulfide sites. **(7.6B)** Sulfide-rich breccia. **(7.6C)** Amphibole-quartz diorite. **(7.6D)** Leucocratic breccia. **(7.6E)** Mafic and leucocratic norites. **(7.6F)** Sublayer norite.

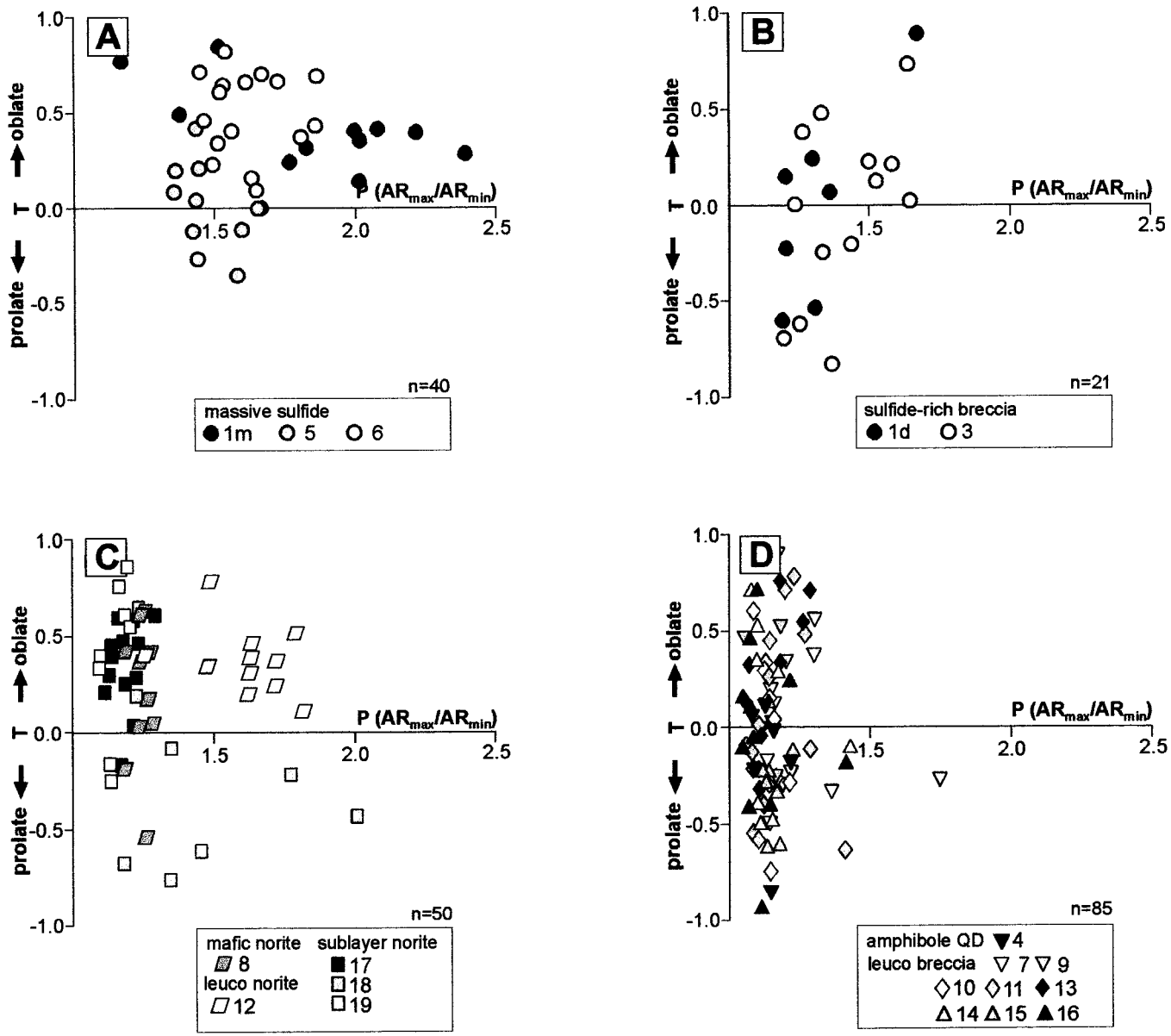
A
B
C
D
T
oblate
prolate
P (ARmax/ARmin)
1.0
0.5
0.0
-0.5
-1.0
1.5
2.0
2.5
n=40
massive sulfide
1m 5 6
n=21
sulfide-rich breccia
1d 3
n=50
mafic norite 8
leuco norite 12
sublayer norite 17 18 19
n=85
amphibole QD 4
leuco breccia 7 9 10 11 13 14 15 16

Fig. 7.6.

ferromagnetic component. The sulfide component of the specimens instead consists of paramagnetic chalcopyrite and pyrite. P values for the sulfide-rich breccia specimens range from 1.19 to 1.67.

Noritic specimens, including the sublayer, leucocratic and mafic norites (Fig. 7.5C), have consistently high $AR_{av}$ values, similar to the massive sulfide samples (~700 mA/m to ~17,000 mA/m). The greatest variation in $AR_{av}$ values occurs for sublayer norite sites WL17 and WL18. P values for the norites are also variable, ranging from 1.09-2.01 for AAR, with the greatest variation occuring for sites WL12 and WL18.

Amphibole-quartz diorite and leucocratic breccia specimens (Fig. 7.5D) have $AR_{av}$ values between ~15 mA/m and ~4000 mA/m. As with the AMS, the greatest variation in $AR_{av}$ values occurs for sites WL11 and WL13. Variations in the abundance of magnetite within sites are responsible for the relatively large standard deviations of $AR_{av}$ in the amphibole-quartz diorite and leucocratic breccia specimens. The range of P values is more restricted for the leucocratic breccia and amphibole-quartz diorite sites (1.09-1.81 for AAR).

Compared to the AMS results, the P values for the AAR measurements are higher. On the other hand, T values show a similar distribution to those recorded for AMS. A dominantly oblate magnetic fabric (T>0) is recorded for the majority of the massive sulfide and norite samples using the AAR method (Fig. 7.6A,C). There is no relationship between the degree of anisotropy and the shape of the ellipsoid.

*Directional data:* The AAR method records the average mineral preferred orientations of all the ferromagnetic grains in a sample. Based on the previously recorded magnetic responses (section 7.3), it is expected that for *Type 1* sites, the AAR method should record similar fabrics to the AMS. For *Type 2* sites the AAR may record dissimilar fabrics to

**Figure 7.7.** AAR fabric map for the Whistle embayment and the proximal Whistle Offset dyke. Equal-area projections of ARmax (squares) and ARmin (circles). The magnetic foliation plane for each site is shown as a dashed great circle. Orientations for individual specimens (small symbols) and the site average (large symbols) are shown. The orientation of the nearby dyke wall is shown as a solid black line. Location of Fig. 7.8 is indicated. Base map provided by FNX Mining Company Ltd.

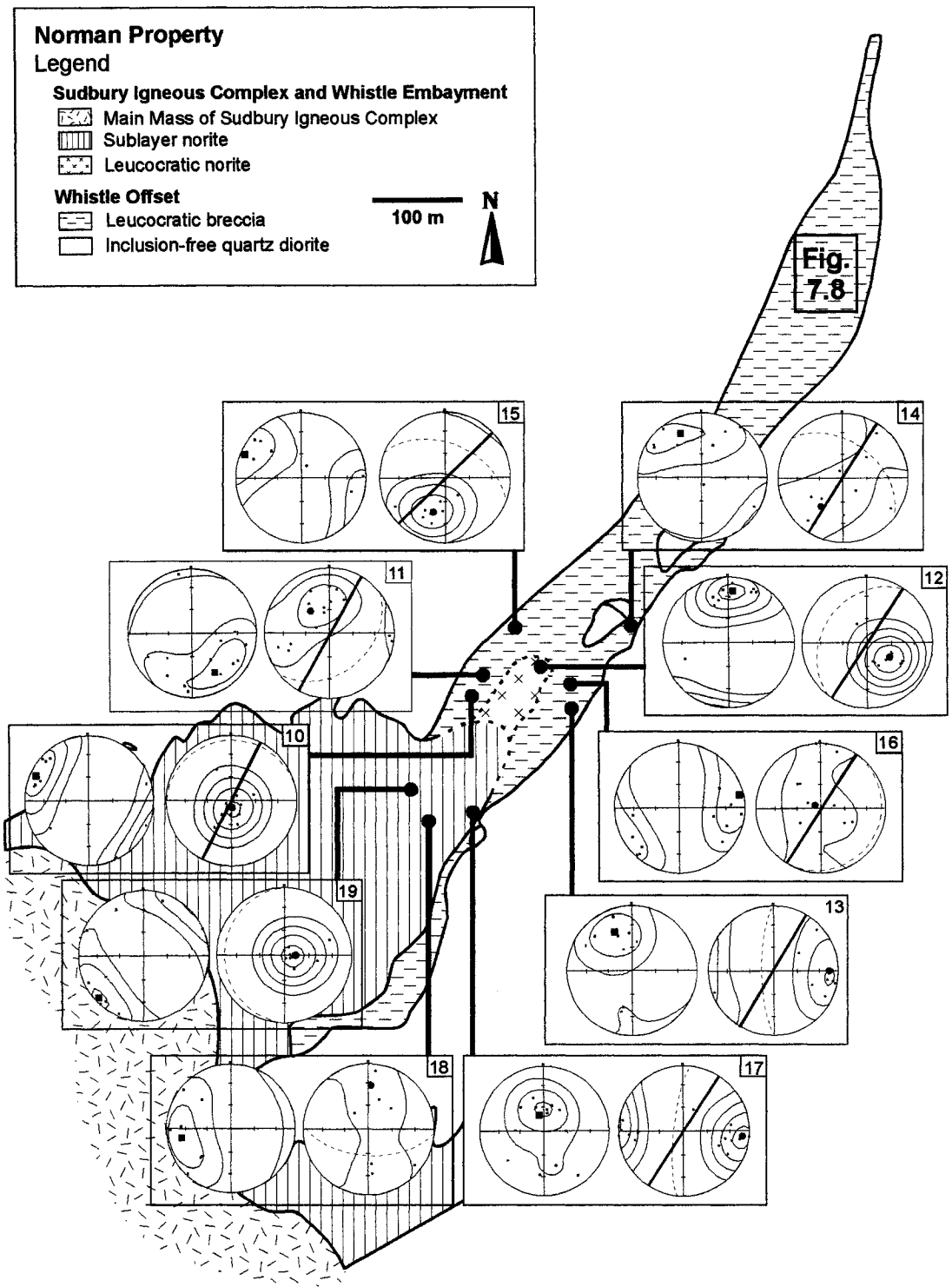
Norman Property
Legend
Sudbury Igneous Complex and Whistle Embayment
Main Mass of Sudbury Igneous Complex
Sublayer norite
Leucocratic norite
Whistle Offset
Leucocratic breccia
Inclusion-free quartz diorite
100 m
N
Fig. 7.8
15
14
11
12
10
16
19
13
18
17

Fig. 7.7.

the AMS, as the paramagnetic component, which may be mainly metamorphic, does not contribute to the AAR.

The AAR measurements provide very similar magnetic fabric orientations to those provided by the AMS for the sublayer and leucocratic norite sites from the Whistle embayment (compare Figs. 7.3 and 7.7). This confirms that the ferromagnetic mineral fraction, and not the paramagnetic fraction, controls the AMS fabric orientations for those *Type 1* sites.

Leucocratic breccia sites within the proximal Whistle dyke (Fig. 7.7) show *Type 2* magnetic responses, indicating that the ferromagnetic component controlling the AAR fabric is principally magnetite, which may include both coarse-grained (primary) or fine-grained (metamorphic) fractions. Both the soft coercivity coarse-grained magnetite and the harder coercivity fine-grained magnetite contribute to the AAR fabric.

Two of the leucocratic breccia sites, sites WL11 and WL13 (Fig. 7.7), have AAR fabric orientations that are similar to the AMS orientations. Both sites have approximately one order higher average intensities (Table 7.2) than the other leucocratic sites indicating a greater abundance of ferromagnetic minerals for those two sites. The AAR lineations at both sites are shallowly plunging. Site WL11 has a NE striking subhorizontal average foliation, while site WL13 has near vertical N-S striking foliation.

Within the rest of the proximal Whistle Offset dyke (Fig. 7.7), the AAR fabric orientations are dissimilar to the AMS. The AAR lineations plunge to the NW for sites WL10, WL14 and WL15, and plunge to the E for site WL16. Sites WL14 and WL15 have subvertical foliations, which strike nearly perpendicular to the dyke walls. Magnetic lineations for the same two sites have a trend that is also perpendicular to the dyke walls. Site WL15, which has a well-defined magnetic foliation, shows an approximately 90° rotation

**Figure 7.8.** AAR fabric map of the distal Whistle Offet dyke where the North deposit outcrops. Equal-area projections of ARmax (squares) and ARmin (circles). The magnetic foliation plane for each site is shown as a dashed great circle. Orientations for individual specimens (small symbols) and the site average (large symbols) are shown. The approximate orientation of the dyke wall is shown as a solid black line. Approximate Location of this map is shown in Fig. 7.7. Base map provided by FNX Mining Company Ltd.

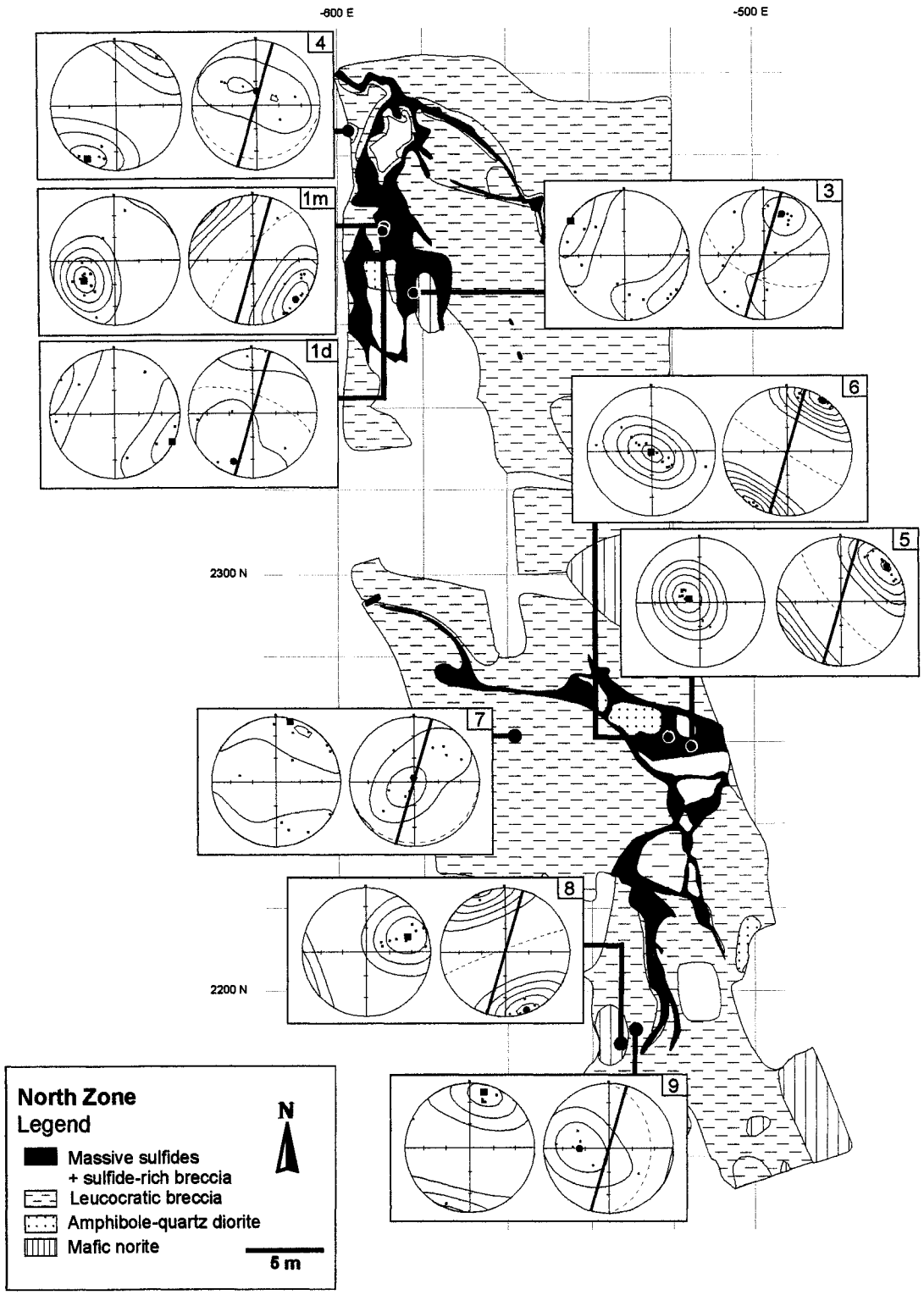
-600 E
-500 E
4
1m
1d
3
6
5
2300 N
7
8
2200 N
9
North Zone
Legend
Massive sulfides
+ sulfide-rich breccia
Leucocratic breccia
Amphibole-quartz diorite
Mafic norite
N
5 m

Fig. 7.8.

from the AMS. Sites WL10 and WL16 have horizontal foliations. Both the lineation and foliation for site WL16 are poorly defined.

AAR foliations and lineations for the massive sulfide sites of the North Zone are very similar to those for AMS (compare Figs. 7.4 and 7.8). The foliations are near vertical and strike NE-SW (WL1m) or NW-SE (WL5 and WL6), whereas the lineations are vertical to subvertical. The rest of the *Type 1* sites, WL1d, WL3, and WL8, also show similar fabrics to the AMS. The sulfide-rich breccia sites, WL1d and WL3, both show horizontal NW-SE trending lineations and poorly defined NW or SE striking subvertical foliations. Leucocratic breccia site WL9 has a similar foliation and lineation to the AMS. Amphibole-quartz diorite site WL4 shows a similar lineation orientation to the AMS, but shows a poorly defined horizontal average magnetic foliation with a girdle distribution of the individual specimen orientations. Site WL7 has a similar AAR fabric to WL4, with a N trending horizontal lineation and horizontal foliation.

### *7.3. Anisotropy of partial Anhysteretic Remanence Magnetization (ApAR)*

The ApAR technique allows for the measurement of the anisotropy of the ferromagnetic minerals corresponding to different coercivity fractions. The different coercivities may correspond to different grain sizes of minerals or to different mineral species. Here, the ApAR is employed to separate out the fabrics defined by the coarse-grained, softer coercivity magnetite, which is interpreted to represent the emplacement flow kinematics of the dyke and the embayment. *Scalar parameters:* Due to the remagnetization of only part of the ferromagnetic mineral populations during pAR acquisition, the resulting $pAR_{av}$ intensities are lower than the AAR values (Table. 7.3). $pAR_{av}$ intensities for the

**Table 7.3.** Average ApAR data by sampling site.

Table 7.3. Average ApAR data by sampling site

| Site | N | Type | range (mT) | pARav (mA/m) | St Dev | pARmax dec/inc | pARmin dec/inc | P | T | L | F |
|---|---|---|---|---|---|---|---|---|---|---|---|
| WL1m | 12 | MS | 0-10 | 742 | 424 | 241/39 | 139/13 | 2.15 | 0.24 | 1.33 | 1.61 |
| WL1d | 7 | SB | 0-20 | 67 | 51 | 115/09 | 004/02 | 1.36 | -0.02 | 1.14 | 1.20 |
| WL2 | 14 | SB | - | - | - | - | - | - | - | - | - |
| WL3 | 14 | SB | 0-20 | 687 | 768 | 300/05 | 027/71 | 1.40 | -0.04 | 1.18 | 1.19 |
| WL4 | 6 | AD | 0-20 | 9 | 2 | 087/76 | 311/07 | 1.11 | 0.45 | 1.03 | 1.08 |
| WL5 | 11 | MS | 0-10 | 1062 | 372 | 288/69 | 045/11 | 1.90 | -0.05 | 1.42 | 1.34 |
| WL6 | 16 | MS | - | - | - | - | - | - | - | - | - |
| WL7 | 11 | LB | 0-20 | 15 | 26 | 206/71 | 060/15 | 1.44 | 0.00 | 1.18 | 1.21 |
| WL8 | 10 | MN | 0-10 | 2390 | 173 | 063/28 | 333/02 | 1.41 | 0.02 | 1.18 | 1.20 |
| WL9 | 7 | LB | 0-20 | 31 | 12 | 072/47 | 273/32 | 1.20 | -0.02 | 1.09 | 1.10 |
| WL10 | 10 | LB | 0-20 | 16 | 6 | 238/10 | 345/22 | 1.09 | -0.03 | 1.04 | 1.04 |
| WL11 | 13 | LB | 0-10 | 119 | 349 | 208/18 | 318/29 | 1.27 | 0.01 | 1.14 | 1.12 |
| WL12 | 11 | MN | 0-10 | 1874 | 226 | 006/23 | 127/58 | 1.76 | 0.47 | 1.17 | 1.50 |
| WL13 | 9 | LB | 0-15 | 174 | 315 | 198/64 | 312/11 | 1.25 | 0.14 | 1.09 | 1.14 |
| WL14 | 10 | LB | 0-20 | 8 | 6 | 018/17 | 101/01 | 1.15 | 0.07 | 1.06 | 1.09 |
| WL15 | 8 | LB | 0-20 | 9 | 1 | 001/60 | 276/02 | 1.10 | -0.05 | 1.04 | 1.05 |
| WL16 | 11 | LB | 0-20 | 15 | 10 | 189/41 | 307/16 | 1.17 | -0.03 | 1.08 | 1.08 |
| WL17 | 13 | SN | 0-10 | 1194 | 1056 | 013/38 | 097/00 | 1.31 | 0.36 | 1.09 | 1.20 |
| WL18 | 7 | SN | 0-10 | 4702 | 3935 | 254/23 | 147/50 | 1.63 | -0.19 | 1.32 | 1.22 |
| WL19 | 9 | SN | 0-10 | 1710 | 958 | 026/09 | 275/75 | 1.26 | 0.10 | 1.13 | 1.11 |

N=number of specimens; Type=rock type: massive sulfide (MS), sulfide-rich breccia (SB), amphibole-quartz diorite (AD), leucocratic breccia (LB), mafic norite (MN), sublayer norite (SN), leucocratic norite (LN); range = range of decaying AF over which d.c. field was applied for ApAR measurements; pARav = mean partial anhysteretic remanence magnetization in mA/m; ST DEV= standard deviation of pARav; Dec/Inc=declination and inclination in degrees; P= degree of anisotropy; T=shape of the remanence ellipsoid; eccentricity of the ellipsoid based on magnetic lineation (L) and magnetic foliation (F).

different sites range from 8 mA/m for WL14 (leucocratic breccia) to 4702 mA/m for WL18 (sublayer norite).

For the *Type 1* massive sulfide sites the direct field (DF) was applied from 0-10 mT. Average pAR values for the massive sulfide specimens (Fig. 7.9A) range from ~200 mA/m to ~1700 mA/m. P values for the massive sulfide specimens are further increased using the ApAR method compared to AAR, ranging from 1.49 to 3.14.

For the sulfide-rich breccia sites, the DF was applied from 0-20 mT. Average pAR values for the sulfide-rich breccia specimens (Fig. 7.9B) range from ~15 mA/m to ~2800 mA/m. $pAR_{av}$ values are fairly similar to those obtained for the same specimens using AAR, being only slightly lower. Values are higher for site WL3, which has a higher magnetite content (15%) than site WL1D. Degree of anisotropy, P, values are similar to those for AAR, ranging from 1.17 to 1.89. Low P values indicate that pyrrhotite does not contribute significantly. Magnetite is therefore the primary ferromagnetic component for ApAR.

For the *Type 1* noritic sites, the DF was applied over the 0-10 mT range. Average pAR values for the noritic specimens (Fig. 7.9C) range from ~250 mA/m to ~12,000 mA/m. As for AAR, the greatest variation in $pAR_{av}$ values occurs for sites WL17 and WL18. P values for the norites are also variable, ranging from 1.15-2.48. The greatest variation in P values occurs for sites WL12 and WL18.

For the *Type 2* leucocratic breccia and amphibole-quartz diorite sites the DF was applied over different AF ranges, with the AF range required to clean approximately 50% of the AR being chosen. A smaller range was used for the two leucocratic breccia sites with higher than average intensities for both AMS and AAR (0 to 10 mT for WL11 and 0 to 15 mT for WL13). A range of 0 to 20 mT was used for the remaining sites. Average AR values for the leucocratic breccia and amphibole-quartz diorite sites range from ~2 mA/m to ~1300

**Figure 7.9.** Scalar parameters for ApAR. Degree of anisotropy (P) plotted as a function of average partial anhysteretic remanence ($pAR_{av}$) of the specimen. **(7.5A)** P vs. $pAR_{av}$ plots for massive sulfide sites. **(7.5B)** Sulfide-rich breccia. **(7.5C)** Amphibole-quartz diorite. **(7.5D)** Leucocratic breccia. **(7.5E)** Mafic and leucocratic norites. **(7.5F)** Sublayer norite.

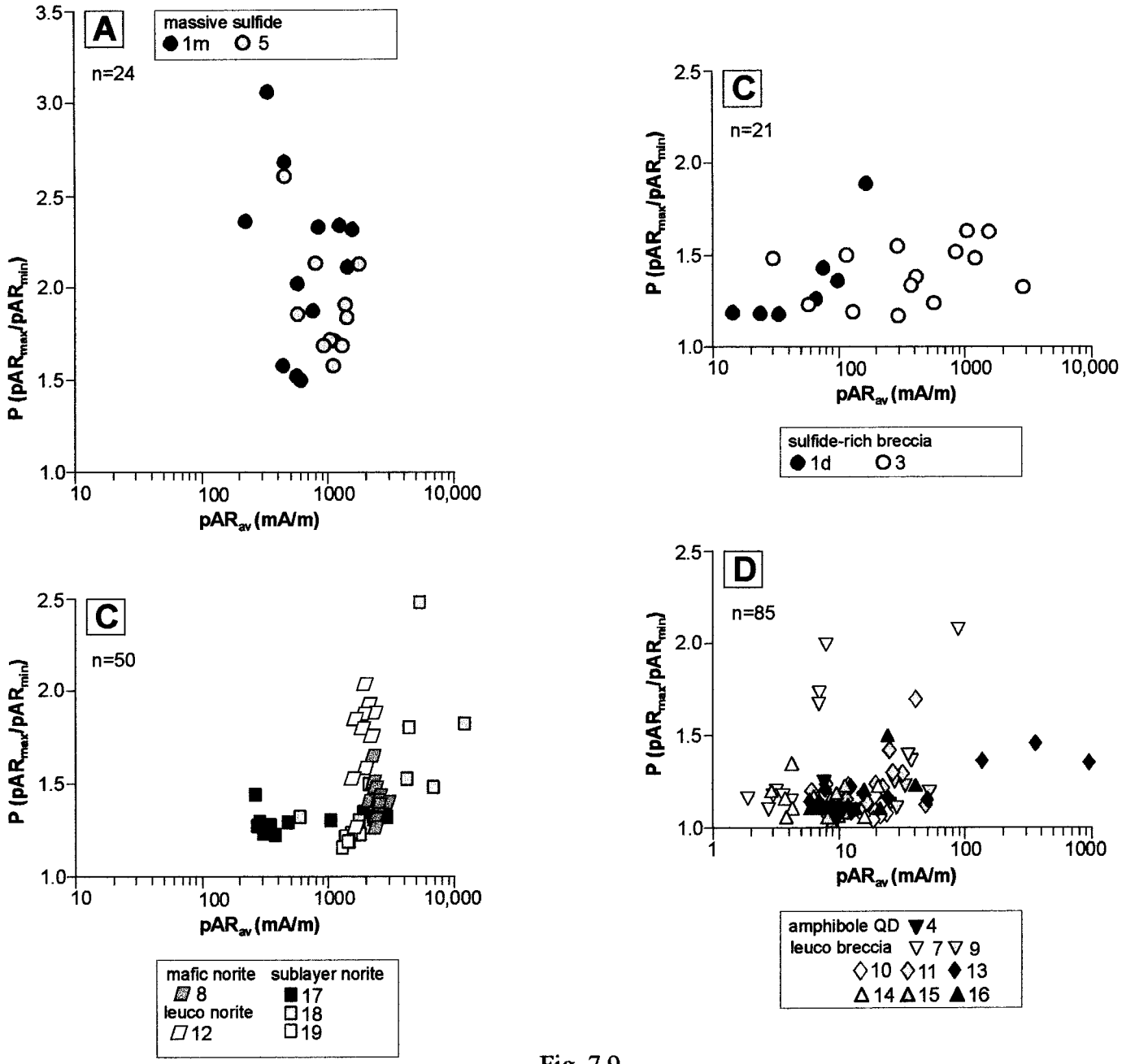
A
massive sulfide
1m 5
n=24
C
n=21
sulfide-rich breccia
1d 3
C
n=50
mafic norite sublayer norite
8 17
leuco norite 18
12 19
D
n=85
amphibole QD 4
leuco breccia 7 9
10 11 13
14 15 16
P (pARmax/pARmin)
pARav (mA/m)

Fig. 7.9.

**Figure 7.10.** Scalar parameters for ApAR. Shape parameter (T) plotted as a function of the degree of anisotropy (P). **(7.10A)** PT plots for massive sulfide sites. **(7.10B)** Sulfide-rich breccia. **(7.10C)** Amphibole-quartz diorite. **(7.10D)** Leucocratic breccia. **(7.10E)** Mafic and leucocratic norites. **(7.10F)** Sublayer norite.

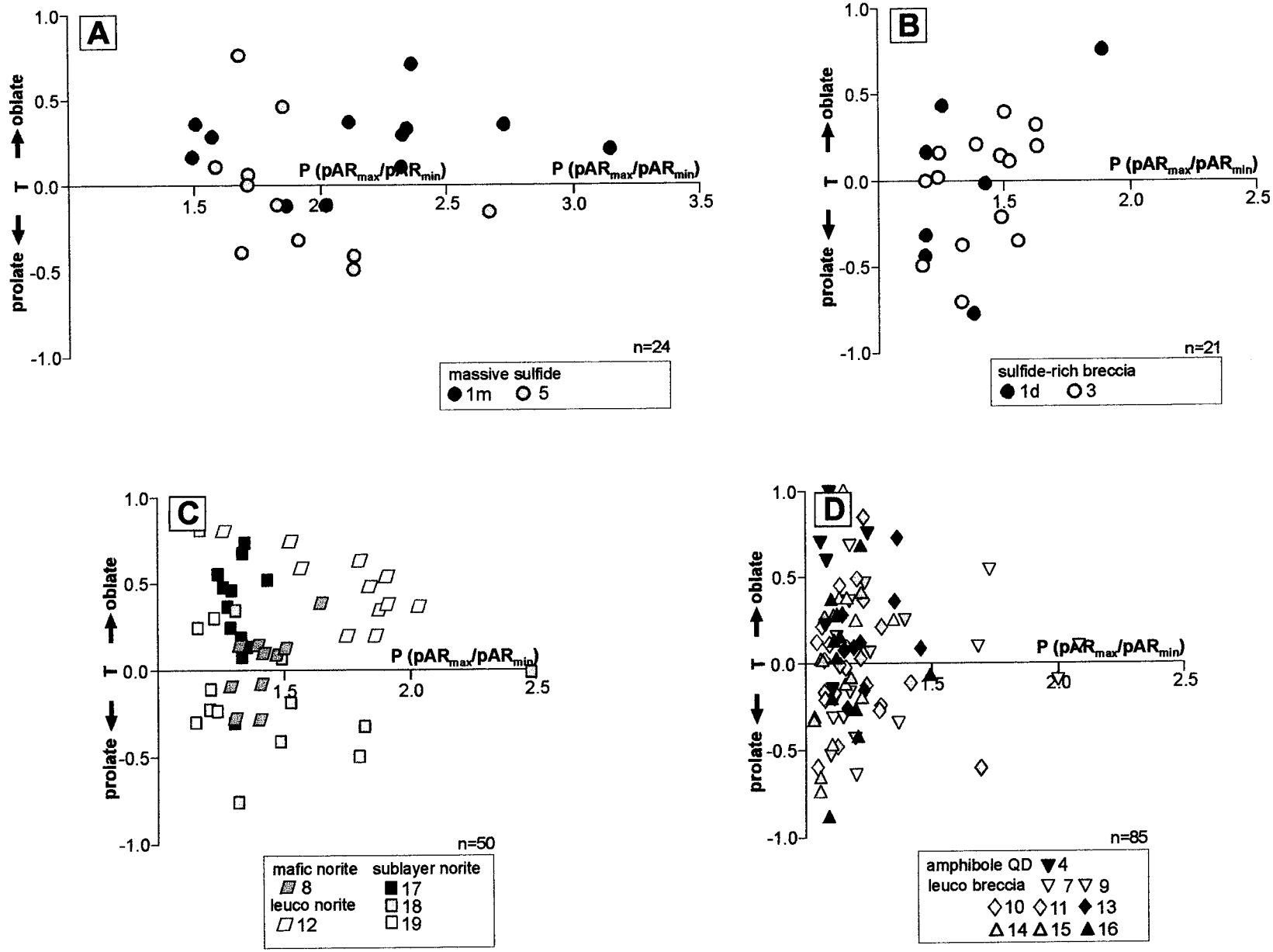
A
B
C
D
T
oblate
prolate
P (pAR$_{max}$/pAR$_{min}$)
n=24
massive sulfide
1m 5
n=21
sulfide-rich breccia
1d 3
n=50
mafic norite 8
sublayer norite 17
leuco norite 12
18
19
n=85
amphibole QD 4
leuco breccia 7 9
10 11 13
14 15 16

Fig. 7.10.

mA/m. The greatest variation occurs for site WL11. The rest of the sites do not exhibit intensities above 100 mA/m. The P values for the leucocratic breccia and amphibole-quartz diorite sites range from 1.04 to 2.08. P values are fairly similar to those obtained using AAR.

For ApAR, all rock types have a broad range of ellipsoid shapes, with T values ranging from quite prolate to quite oblate. Noritic sites WL12 and WL17 (Fig. 7.10C) still show dominantly oblate fabrics as for AAR, while the remaining noritic sites show no dominant fabric ellipsoid shape. The amphibole-quartz diorite site and the leucocratic breccia sites show no dominant fabric shapes. There does not appear to be a strong correlation between P and T values.

*Directional data:* The ApAR fabrics of *Type 1* sites, for which the AMS and AAR fabrics are interpreted to be controlled by the soft coercivity fraction, the ApAR fabrics are expected to have similar orientations to those obtained by those two methods. For *Type 2* sites, for which a hard coercivity fraction is present, the ApAR fabrics should better represents the preferred orientations of the coarse-grained magnetite, as the hard coercivity component, primarily fine-grained magnetite, was not remagnetized.

ApAR gives similar magnetic fabric orientations to both the AMS and AAR for the sublayer and leucocratic norite samples from the Whistle embayment (Fig. 7.11). This confirms that both the AMS and AAR fabrics for these *Type 1* sites were controlled by the soft coercivity coarse-grained magnetite fraction. Site WL18 shows a much better defined magnetic foliation than for AMS or AAR with a SW striking moderately dipping foliation.

Leucocratic breccia sites within the proximal Whistle (Fig. 7.11) have *Type 2* magnetic responses, indicating that the ferromagnetic component controlling the AAR fabric

**Figure 7.11.** ApAR fabric map for the Whistle embayment and the proximal Whistle Offset dyke. Equal-area projections of pARmax (squares) and pARmin (circles). The magnetic foliation plane for each site is shown as a dashed great circle. Orientations for individual specimens (small symbols) and the site average (large symbols) are shown. The orientation of the nearby dyke wall is shown as a solid black line. Location of Fig. 7.12 is indicated. Base map provided by FNX Mining Company Ltd.

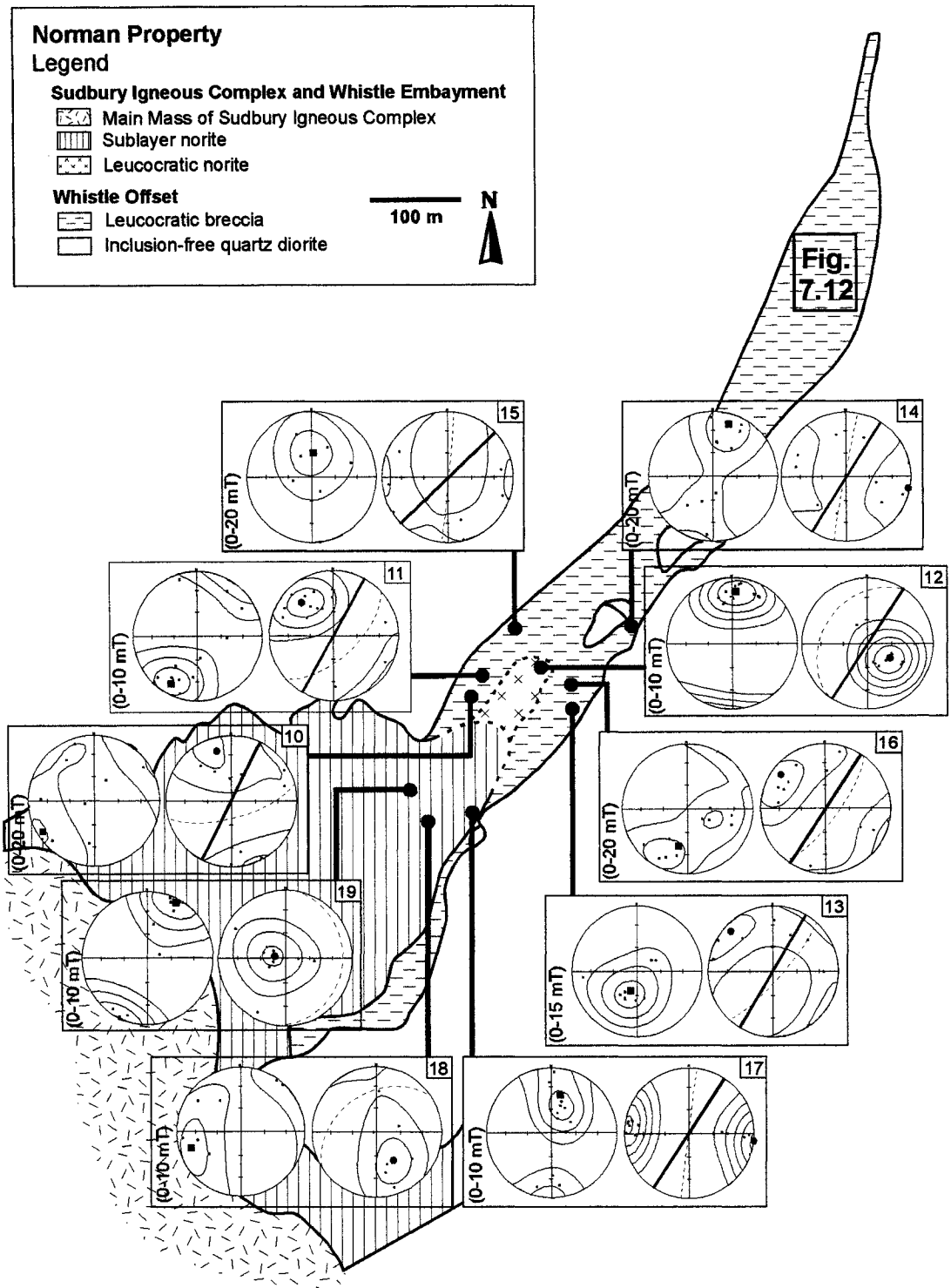
Norman Property
Legend
Sudbury Igneous Complex and Whistle Embayment
Main Mass of Sudbury Igneous Complex
Sublayer norite
Leucocratic norite
Whistle Offset
Leucocratic breccia
Inclusion-free quartz diorite
100 m
N
Fig. 7.12
15
(0-20 mT)
14
(0-20 mT)
11
(0-10 mT)
12
(0-10 mT)
10
(0-20 mT)
16
(0-20 mT)
19
(0-10 mT)
13
(0-15 mT)
18
(0-10 mT)
17
(0-10 mT)

Fig. 7.11.

was magnetite, which may be either coarse-grained or fine-grained. In ApAR, the harder coercivity fine-grained magnetite is not expected to contribute to the ApAR fabric.

Two of the leucocratic breccia sites, sites WL11 and WL13, show similar foliations to the AMS and AAR (compare Figs. 7.3, 7.7 and 7.11). The use of ApAR gives a better defined NE striking subvertical average foliation for site WL13, while a similar, yet less well defined, foliation is obtained for the same site compared to the ones recorded using AMS or AAR. Site WL11 has a near horizontal lineation which trends parallel to the strike of the dyke. ApAR gives a near vertical foliation for site WL13.

Within the rest of the proximal Whistle Offset dyke, the ApAR foliations for sites WL14 and WL15 are poorly defined and are near vertical striking N-S, slightly obliquely to the dyke walls. The foliation for site WL10 is near vertical and strikes approximately E-W, oblique to the dyke wall. The average foliation for WL16 is also near vertical and strikes NE-SW, parallel to the dyke wall. Magnetic lineations for sites WL14 and WL15 are horizontal and plunging ~50° respectively and trend to the North. At sites WL10 and WL16 the magnetic lineations are poorly defined, the average orientations of the magnetic lineations are 238/10 and 189/41 respectively. In general, the magnetic fabrics in the proximal Offset are similar to those recorded by the AMS but are less well defined. In the case of site WL11 the fabric is better defined for ApAR than for AMS or AAR.

The ApAR fabrics are not greatly improved using ApAR for the massive sulfide sites (WL1m and WL5) of the North Zone (Fig. 7.12) (ApAR was not measured for site WL6 as no obvious improvement was observed for the other two sites). The rest of the *Type 1* sites, WL1d, WL3, and WL8, also show similar fabrics to the AMS and AAR. Leucocratic breccia site WL9 has a similar foliation to the AMS and AAR. The lineation for the same site is dissimilar to those obtained using AMS or AAR, with a subvertical plunge and NE trend.

**Figure 7.12.** ApAR fabric map of the distal Whistle Offet dyke where the North deposit outcrops. Equal-area projections of pARmax (squares) and pARmin (circles). The magnetic foliation plane for each site is shown as a dashed great circle. Orientations for individual specimens (small symbols) and the site average (large symbols) are shown. The approximate orientation of the dyke wall is shown as a solid black line. Approximate Location of this map is shown in Fig. 7.11. Base map provided by FNX Mining Company Ltd.

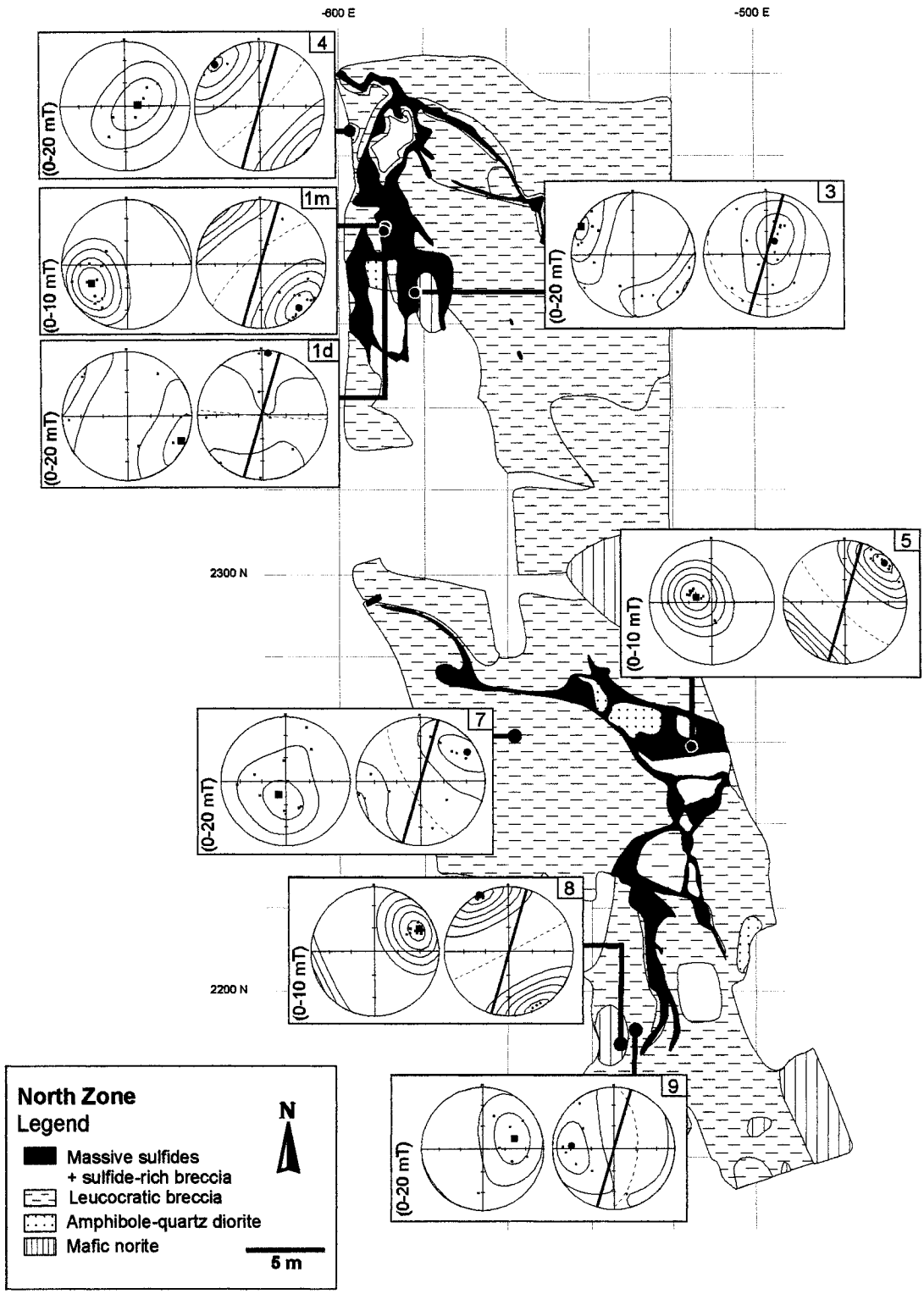
-600 E
-500 E
2300 N
2200 N
4
(0-20 mT)
1m
(0-10 mT)
1d
(0-20 mT)
3
(0-20 mT)
5
(0-10 mT)
7
(0-20 mT)
8
(0-10 mT)
9
(0-20 mT)
North Zone
Legend
Massive sulfides
+ sulfide-rich breccia
Leucocratic breccia
Amphibole-quartz diorite
Mafic norite
N
5 m

Fig. 7.12.

Site WL7, a leucocratic breccia, show similar fabrics to the AMS, but a less well defined. Site WL4 has a similar foliation to the AMS, but shows a vertical lineation, which is unlike the horizontal lineation recorded by both the AMS and AAR techniques. In general, the North Zone sites have near vertical obliquely striking magnetic foliations. Magnetic lineations are generally near horizontal where well defined, with the exception of the massive sulfide sites and the amphibole-quartz diorite sites where the lineations are near vertical.

*7.4. Summary of the primary magnetic anisotropy fabrics*

Maps were compiled with the fabrics being chosen that were believed to represent the primary emplacement flow fabrics. In other words, one of the AMS, AAR or ApAR fabrics was chosen for each of site which was interpreted to best represent the magnetic fabric defined by the primary, magmatic coarse-grained magnetite crystals. For the majority of sites with *Type 1* magnetic responses, where the fabrics are similar for each method, the AMS fabrics were used for the compilation. In some cases, where slightly better defined fabrics were recorded, the ApAR plot was used instead for the *Type 1* sites. For *Type 2* sites, ApAR data was chosen where it is dissimilar to the AMS or where the elimination of the high-coercivity fraction has improved on the AMS data. In some cases the fabrics are similar for AMS and ApAR, but the AMS plots are better defined so they are used instead. For *Type 3* sites, the AMS data is also plotted, as AAR and ApAR are not available.

Lower hemisphere equal-area projections of the directional data are shown for each sample site in Fig. 7.13 (embayment and proximal offset) and Fig. 7.14 (the North Zone). The dyke margins were not exposed at the North Zone outcrop; their orientations in the equal-area plots in Fig. 7.14 are interpreted from available maps (e.g. Fig. 7.13).

**Figure 7.13.** Summary fabric map for the Whistle embayment and the proximal Whistle Offset dyke. The magnetic foliation plane for each site is shown as a dashed great circle. Orientations for individual specimens (small symbols) and the site average (large symbols) are shown. The orientation of the nearby dyke wall is shown as a solid black line. Base map provided by FNX Mining Company Ltd.

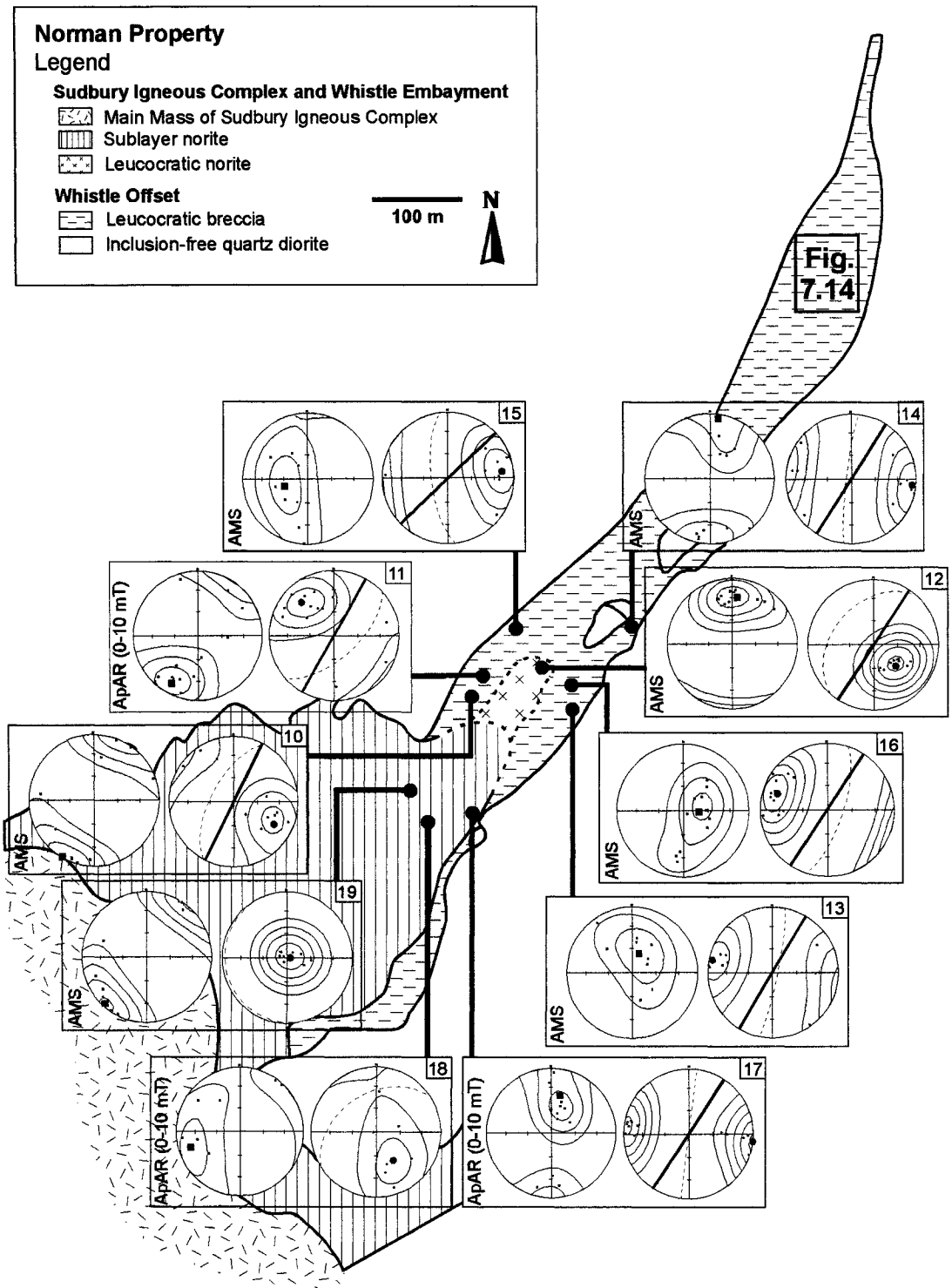
Norman Property
Legend
Sudbury Igneous Complex and Whistle Embayment
Main Mass of Sudbury Igneous Complex
Sublayer norite
Leucocratic norite
Whistle Offset
Leucocratic breccia
Inclusion-free quartz diorite
100 m
N
Fig. 7.14
15
AMS
14
AMS
11
ApAR (0-10 mT)
12
AMS
10
AMS
16
AMS
19
AMS
13
AMS
18
ApAR (0-10 mT)
17
ApAR (0-10 mT)

Fig. 7.13.

Within the Whistle Embayment (Fig. 7.13), AMS results are used for sites WL12 and WL19, while the ApAR results are used for sites WL17 and WL18, as ApAR provided slightly better defined fabrics for those *Type 1* sites. Sublayer norite site WL19, located towards the centre of the embayment, has a horizontal magnetic foliation and horizontal lineation trending parallel to the strike of the dyke. Approaching the outer wall of the embayment, site WL18 has a subhorizontal foliation striking parallel to the strike of the dyke, with a near horizontal lineation trending parallel to the strike of the dyke. At the contact of the embayment with the dyke wall, site WL17 has a vertical foliation striking approximately N-S, oblique to the dyke wall. Near the dyke wall, the magnetic lineation for WL17 plunges more steeply and trends roughly parallel to the strike of the dyke. The leucocratic norite site, WL12, shows a N trending horizontal lineation and SW striking, moderately dipping foliation that is similar to site WL18. The recorded fabrics for the Whistle embayment fit with the believed funnel shape of the embayment coupled with a lateral flow into the dyke.

Within the proximal Offset (Fig. 7.13), the recorded fabrics fall into two groups. The first group includes sites with subvertical to vertical foliations and horizontal lineations. This group includes leucocratic breccia sites WL10, WL11, and WL14. The fabrics for these sites fit with those expected in the case of lateral flow within a dyke. In all cases the foliation strike parallel or slightly obliquely to the dyke walls and the magnetic lineations trend parallel to the strike of the dyke. The second group of sites within the proximal Offset includes sites that also have subvertical to vertical foliations but have near vertical lineations. This second group includes leucocratic breccia sites WL13, WL15 and WL16. The lineations for these sites do not fit with the proposed model of lateral flow in the dyke and therefore must be explained. Foliations for these sites strike obliquely to the dyke walls, lineations are

**Figure 7.14.** Summary fabric map of the distal Whistle Offet dyke where the North deposit outcrops. The magnetic foliation plane for each site is shown as a dashed great circle. Orientations for individual specimens (small symbols) and the site average (large symbols) are shown. The approximate orientation of the dyke wall is shown as a solid black line. Base map provided by FNX Mining Company Ltd.

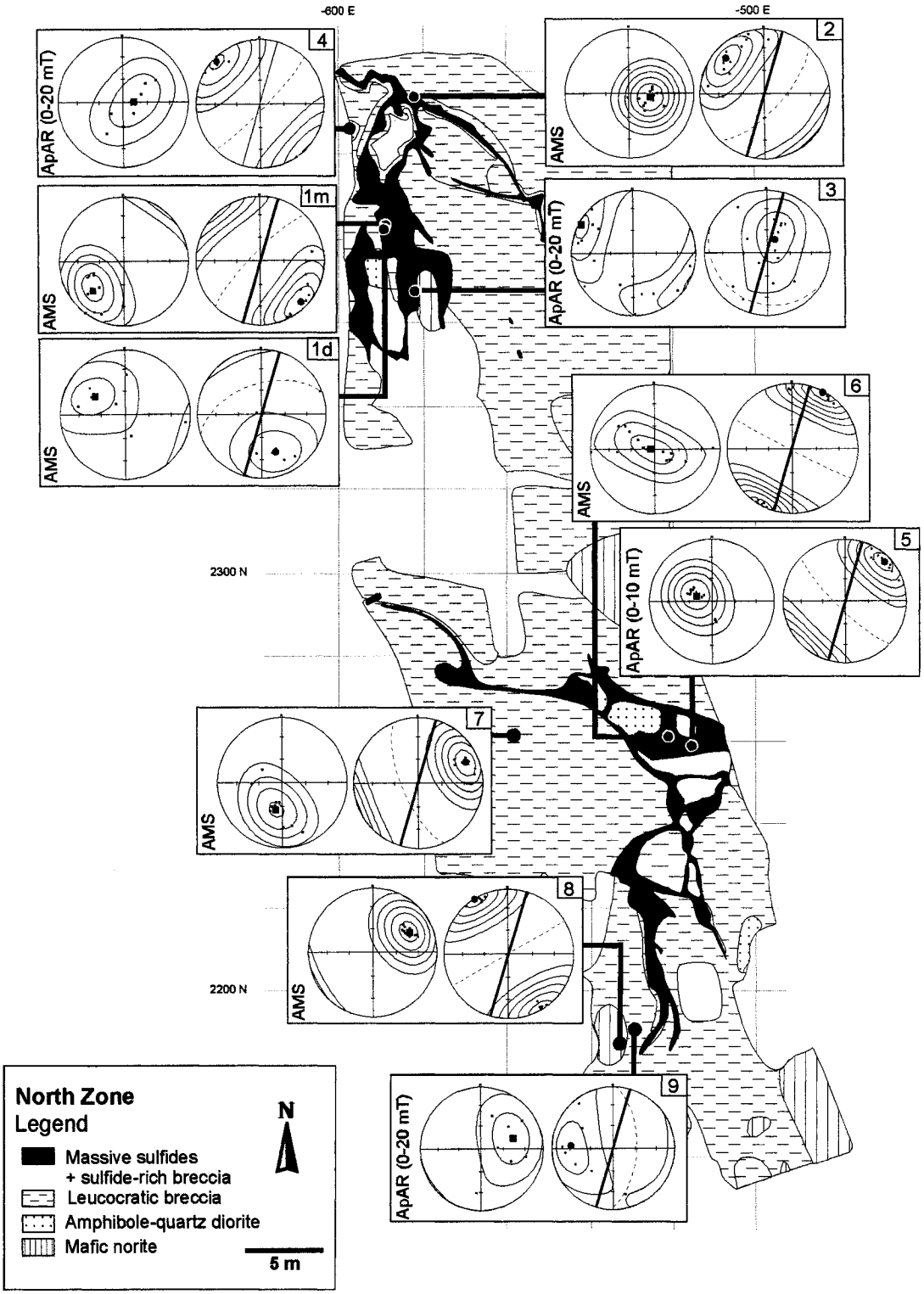
-600 E
-500 E
4
ApAR (0-20 mT)
2
AMS
1m
AMS
3
ApAR (0-20 mT)
1d
AMS
6
AMS
5
ApAR (0-10 mT)
2300 N
7
AMS
8
AMS
2200 N
9
ApAR (0-20 mT)
North Zone
Legend
Massive sulfides
+ sulfide-rich breccia
Leucocratic breccia
Amphibole-quartz diorite
Mafic norite
N
5 m

Fig. 7.14.

near vertical. Along the SE margin, all foliations are counterclockwise oblique to the embayment and dyke margins. Near the NW margin, the obliquity is not consistent; the foliation at site WL10 is parallel to the dyke wall, the foliation at site WL11 is clockwise oblique, and at site WL15 it is counterclockwise oblique.

Within the distal North Zone of the Offset (Fig. 7.14), the magnetic fabrics at most sampling sites are quite well defined although the orientations vary significantly between sites that are only a few metres apart. The magnetic foliations in the North deposit are steeply dipping, with the sole exception being sulfide-rich breccia site WL3, which has a poorly defined horizontal foliation. WL3 is also the only site within the North Zone that records a horizontal average lineation. Sulfide-rich breccia site WL2 and amphibole-quartz diorite sites WL4 both have NE striking, near vertical foliations which record a clockwise obliquity with respect to the dyke margin. Both sites also record near vertical lineations. Sulfide-rich breccia WL1d and massive sulfide site WL1m both have similar steeply dipping foliations to site WL2 and WL4. Lineations for the two sites are subhorizontal and trend to the NW or SW. Two massive sulfide sites, WL5 and WL6, and nearby leucocratic breccia site WL7 all have a similar near vertical SE striking foliations and near vertical lineations. Mafic norite site WL8 is strongly metamorphosed and may be a xenolith. The site records a fabric similar to that of site WL2, with a vertical NE-SW striking foliation and subhorizontal NE trending lineation. If mafic norite is a xenolith, the fabric will not be related to the other flow fabrics in the dyke. Leucocratic breccia site WL9 has a N striking subvertical foliation and subvertical NE trending lineation, which is similar to the lineation for site WL8.

## Chapter 8: Synthesis and Discussion

In this study, magnetic anisotropy fabrics of the Whistle Offset dyke and the Whistle embayment structure were used to map the petrofabrics defined by different populations of Fe-rich minerals in the lithologically and mineralogically complex suite of rocks. Petrographic and SEM observations of the samples revealed that the complex magnetic mineralogy consists of paramagnetic silicates and ferromagnetic minerals of both magmatic and metamorphic origins. The paramagnetic silicate mineralogy that is expected to contribute to the magnetic susceptibility signal of the sample suite includes both primary igneous minerals (biotite, orthopyroxene, clinopyroxene) and low-grade metamorphic minerals (chlorite, Ca-Fe amphibole). The opaque ferromagnetic (*s.l.*) mineralogy that is expected to contribute to the susceptibility signal includes fine- and coarse-grained magnetite, titanomagnetite, pyrrhotite, and minor hematite. The coarse-grained magnetite is interpreted to be primary (of igneous origin) while the fine-grained magnetite is interpreted to be of metamorphic origin. Paramagnetic sulfide minerals chalcopyrite and pyrite are also present, but have low susceptibilities (section 5.1), and will therefore have only a minor influence on the AMS. Only in the case of sulfide-rich breccia site WL2, which lacks a significant ferromagnetic component, are the lower susceptibility chalcopyrite and pyrite crystals expected to contribute significantly to the AMS, along with inclusions of pyroxene.

The principal magnetic subfabric of interest is the one that is defined by coarse-grained, low (soft) coercivity magnetites. The coarse-grained magnetites are interpreted to be primary crystals that formed within the magmas that were derived from the impact melt and can therefore be related to the emplacement of the embayment, the dyke and the hosted massive sulfides. Anhysteretic remanence acquisition and demagnetization tests were used to

study the magnetic responses of the different ferromagnetic mineral fractions within the samples, and the magnetic subfabrics defined by the AMS, the AAR and the ApAR were measured. The results showed that AMS is the most efficient method to determine the primary, emplacement-related subfabric in samples where the coarse-grained magnetite fraction provides the strongest anisotropy signal (i.e. *Type 1* sites). In other samples, the used of ApAR was required to measure the primary magnetite subfabric, in order to eliminate the magnetic signal from harder coercivity pyrrhotite, fine-grained magnetite and hematite (i.e. *Type 2* sites). For a singular site, where there was an absence of a significant ferromagnetic mineral component (i.e. *Type 3* site), AMS was the only option for measuring the petrofabric of the paramagnetic minerals.

The results are now considered in the context of geological and geochemical studies of the Whistle embayment and the Whistle Offset dyke, to provide new constraints on their magmatic emplacement and also on the emplacement of the hosted massive sulfides.

### *8.1. Flow patterns and Offset dyke emplacement*

Murphy and Spray (2002) produced detailed maps of the lithologies that make up the Whistle and Parkin Offsets, and determined the relative timing of emplacement of the different lithologies and of the sulfide-rich rocks. Their study of the field relationships between different lithological units indicates that the clast-bearing rocks which make up most of the Whistle Offset (leucocratic breccia, as defined here) were most likely forcefully injected into a vertical radial fracture in the target rocks. Injection is thought to have occurred during crater excavation and the early stage of crater modification. Their interpretation of forceful injection is based on the presence of very large clasts of country

rock included within the breccia, that were apparently transported large distances, requiring high flow velocities. During the early crater modification stage and prior to any significant differentiation of the impact melt sheet, inclusion-free quartz diorite was intruded from the overlying impact melt sheet into the still unsolidified breccia magma. Only minor amounts of the inclusion-free quartz diorite are found within the Whistle Offset; it is far more abundant in the more distal Parkin Offset (Fig. 2.1). Murphy and Spray (2002) also proposed that the sublayer norite of the Whistle embayment was deposited on top of the Whistle Offset dyke, presumably by gravity accumulation during magmatic differentiation of the overlying SIC. This interpretation was also adopted by Lightfoot et al. (1997) for the Whistle Offset and embayment, and for the radial Offset dykes in general (Lightfoot et al., 2001). The massive sulfides would have originally accumulated at the base of the overlying SIC, and then, due to their high density, would have foundered and sunk into the unsolidified Whistle Offset dyke (Lightfoot et al., 1997; Murphy and Spray, 2002).

Field and petrographic observations, presented herein, from the North deposit are consistent with the interpretation that the massive sulfides were the last lithology to be emplaced within the Whistle Offset dyke. Within the massive sulfide of the North deposit, coarse-grained magnetite crystals are commonly brecciated and rimmed by sulfide minerals (Figs. 4.1A,C,D,E). This suggests that the coarse-grained magnetite crystals originated as xenocrysts and may have been derived from the partially solidified leucocratic breccia magma as the massive sulfides were emplaced. The magnetic subfabrics shown in Figs. 7.13 and 7.14 can be used to propose a refined view of the emplacement history suggested by Murphy and Spray (2002). The interpreted flow pattern is discussed with reference to Fig. 8.1. Two emplacement models, that are consistent with the recorded magnetic subfabrics and

**Figure 8.1.** Interpreted flow trajectories based on the magnetic subfabric measurements shown in Figs. 7.13, 7.14. Solid traces are inferred directly from the magnetic fabric measurements. Dashed traces are interpreted for the region where the Offset dyke is covered by overburden. Open circles mark sampling sites in the embayment and proximal Offset. Rock types as in Fig. 7.13.

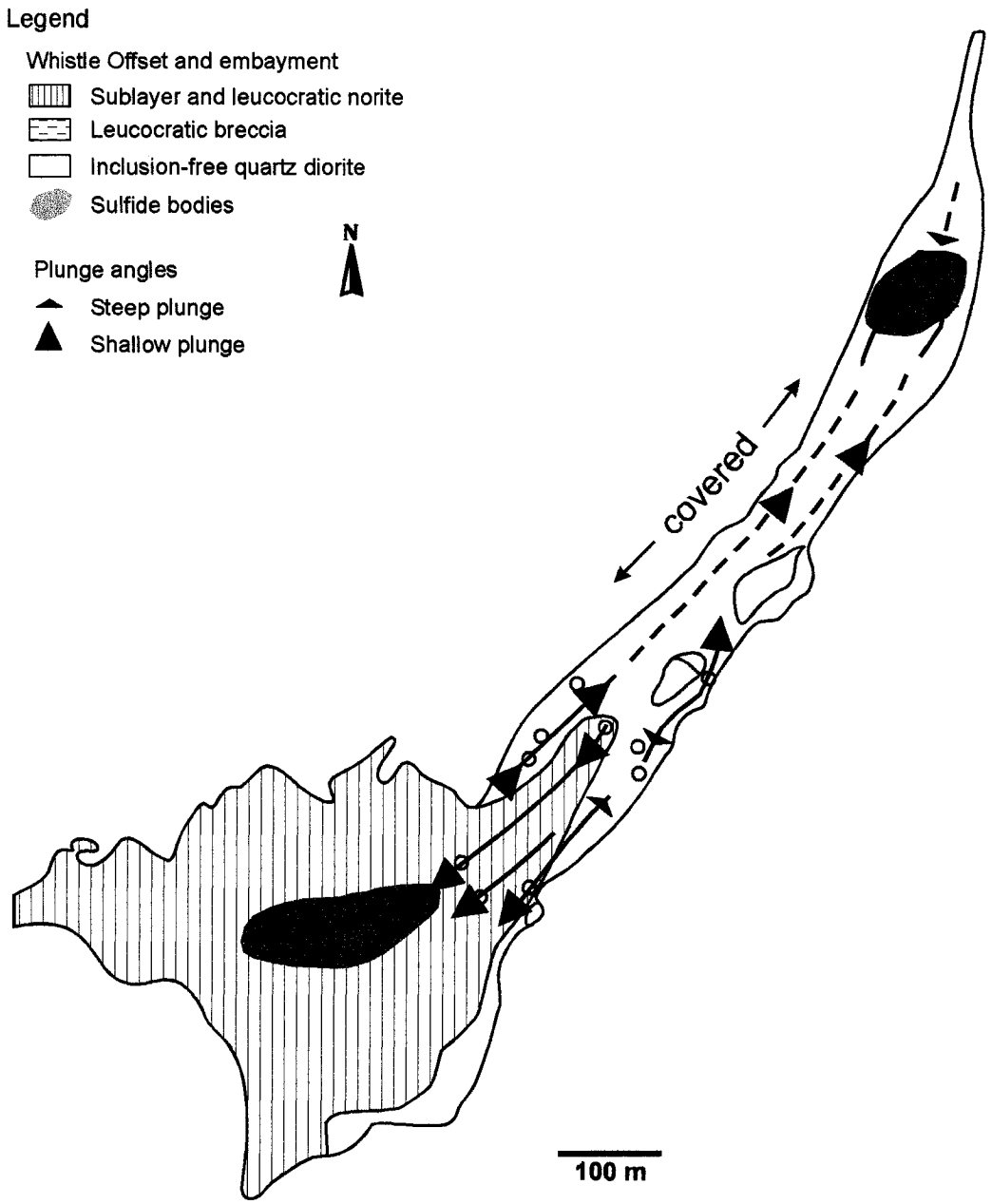
Legend
Whistle Offset and embayment
Sublayer and leucocratic norite
Leucocratic breccia
Inclusion-free quartz diorite
Sulfide bodies
N
Plunge angles
Steep plunge
Shallow plunge
covered
100 m

Fig. 8.1.

with the geological data presented in this thesis, are later shown schematically in Figs. 8.3A,B (model 1) and 8.3C,D (model 2).

Magnetite crystals in the sublayer and leucocratic norites may have originated from the assimilation of diabase into the sublayer magma (Lightfoot et al., 1997) prior to emplacement within the embayment. Coarse-grained magnetite xenocrysts in the embayment rocks therefore likely do not originate from the same immediate source as those found in the Whistle Offset, which were derived from the undifferentiated leucocratic breccia melt. The three sample sites (WL17,18,19) within the sublayer norite reveal a horizontal foliation towards the central part of the Whistle embayment that gradually becomes steeper towards the margin. This is in agreement with the generally accepted funnel shape for the embayment (Pattison, 1979). The magnetic foliations are suggestive of steep walls and a shallowly dipping bottom to the embayment. At sites WL18 and WL19, the lineation in the embayment is horizontal and trends parallel to the axis of the embayment and of the Offset dyke. The well-defined lineation could not have been formed by simple gravity accumulation of the cumulate-textured rock (Figs. 3.3D), which would result in an oblate petrofabric with no lineation (Benn and Allard, 1989). The lineation at sites WL18 and WL19 instead suggests either lateral flow emplacement of the sublayer norite magmas (possibly due to gravity currents or thermal convection within the SIC), or gravity slumping of the pyroxene-rich cumulates on the shallowly dipping floor and steep walls of the funnel shaped embayment. Further studies of the petrofabrics within the Whistle embayment are required to determine which interpretation is correct, as the available magnetic fabric data do not allow for the discrimination between them. In both cases, the lineations documented within the embayment point to a dynamic environment for the formation of the sublayer norites that may have implications for emplacement of the hosted ore deposits.

Leucocratic norite site WL12 has a magnetic foliation, which strikes parallel to the axis of the Offset dyke with a dip of ~35° to the NW. The magnetic lineation of WL12 trends approximately parallel to the axis of the elongated leucocratic norite unit, which stretches outwards from the embayment into the Offset dyke. Within the proximal Offset dyke, at sites WL10, 11, 14, the magnetic foliations dip steeply and the magnetic lineations have shallow to horizontal plunge angles. At the present level of exposure, those fabrics, along with the leucocratic norite fabric, suggest lateral (horizontal) flow of the clast rich impact melts into the vertical fracture, most likely from SW to NE. The direction of flow, as shown in Fig. 8.1, is inferred from the counterclockwise obliquity of the foliation planes with respect to the vertical SE dyke wall. The obliquity between the magnetic foliation and the dyke margins is consistent with a dextral shear gradient in the magma flowing horizontally along the vertical dyke wall. SW to NE emplacement flow is consistent with the generally accepted source of the Offset dyke material having been the SIC melt body (Lightfoot et al., 1997; Murphy and Spray, 2002). An opposing sinistral shear gradient in the magma flow is also required along the NW dyke margin for the magnetic fabrics to fit with the interpretation of SW to NE injection of the magma into non-deforming wallrocks. Therefore, clockwise-oblique magnetic foliations are expected near the NW wall of the proximal Offset dyke, as is present in the case of site WL11. The foliation at site WL10 strikes parallel to the dyke wall and therefore it is also permissive in the case of SW to NE flow. Only at site WL15, where the strike of the magnetic foliation is counter-clockwise oblique, are the data inconsistent with the interpretation of SW to NE flow.

The magnetic lineation data for the sublayer norite specimens at site WL17, which is on the margin of the embayment, are distributed on a partial girdle, with an average orientation that plunges moderately to the north. Along the SE dyke margin in the part of the

proximal Offset dyke closest to site WL17, leucocratic breccia sites WL13 and WL16 preserve steeply plunging lineations, with that of site WL13 resembling the lineation at site WL17. It is interpreted that the magnetic lineations at those three sites may record foundering of the norite and of the leucocratic breccia along the SE wall of the embayment and the nearby part of the Offset dyke. The now steeply plunging lineations were reoriented at sites WL13 and WL16 due to the downward flow, while the original foliation obliquities, which record lateral flow, were apparently preserved. It is unknown whether the foundering resulted from deposition of a denser sublayer norite layer on top of the previously emplaced leucocratic breccia in this part of the Offset and embayment, or whether the steeply plunging lineations record sinking of dense massive sulfides through that region. If the steeply plunging lineations record the sinking of a sulfide body, it may suggest the presence of an ore body below the current level of exposure.

In the distal part of the Whistle Offset dyke, within the North deposit and its host rocks, the strike directions of the mostly steeply dipping magnetic foliations are well defined for the majority of the sites. However, large variation in orientations between sites suggests that a consistent flow plane is not recorded in that outcrop. The Whistle Offset dyke narrows considerably just to the north of the North deposit (Fig. 7.13). It is interpreted that the lack of a well-defined flow plane at the North Zone may be at least partly due to choking of the lateral flow of the highly brecciated rocks, as the dyke narrows significantly from a width of ~100 meters to ~10-20 meters (Fig. 7.3). The locations of the dyke margins relative to the sites in the North Zone are not known, as they are not exposed. The orientations of the dyke margins are therefore interpreted from the larger scale maps and are therefore not useful in determining an accurate sense of obliquity for these sites.

The orientations of the magnetic lineations in the North deposit outcrop also vary strongly between sites. There is a predominance of steep to moderate plunge angles, with the lineations at eight of the ten sites having plunges $\geq 45°$ (Tables 7.1-7.3). At two of the three sites where the massive sulfides were samples, sites WL5 and WL6, the lineations plunge very steeply, and are nearly vertical. It is interpreted that the steep plunge angles of the magnetic lineations within and surrounding the massive sulfide bodies record the sinking of the still ductile, dense sulfide magma into the partly crystallized silicate magma, now represented by the lithologies that host the North deposit. Sinking of the massive sulfide through the North deposit outcrop surface may also have contributed to the variable strike directions of the magnetic foliations there.

One site within the North Zone, site WL8, may record a fabric that is unrelated to the flow within the Offset. The mafic norite site exhibits a much higher degree of greenshist grade metamorphism than other nearby leucocratic breccia sites, and may be a xenolith. The well-defined magnetic fabric for that site is greatly different from that recorded by site WL9, which is located within only a metre of site WL8. Considering the close proximity of the two sites, similar fabrics would be expected for both.

### *8.2. Previous magnetic fabric studies*

In a study of the Copper Cliff Offset dyke, located to the south of the SIC, Scott and Benn (2001, 2002) documented steeply dipping, predominantly NW-SE striking magnetic foliations and steeply plunging to vertical magnetic lineations. Magnetic foliations on both sides of the dyke were found to be counter-clockwise oblique to the vertical dyke margins. The magnetic fabrics in the Copper Cliff Offset led to its re-interpretation as a melt

**Figure 8.2.** Expected mineral lineations and foliations in the cases of flow plus dextral shear **(8.2A)** and simple magmatic flow within a dyke **(8.2B)**. 8.2A is a simplified model for the Copper Cliff Offset dyke modified from Fig. 9 in Scott and Benn (2002).

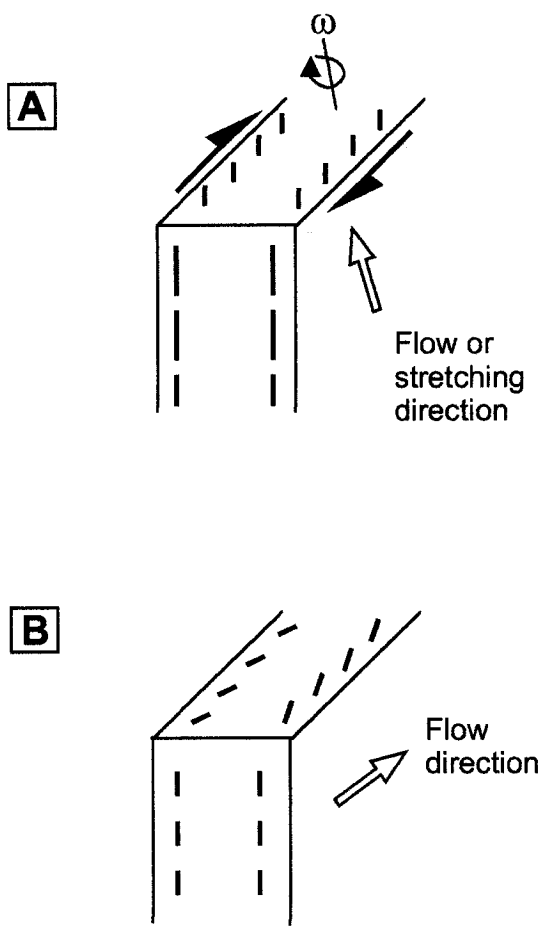


Fig. 8.2.

lubricated dextral transfer fault, as a combination of fault-like movement along with magmatic flow were required to explain the constant sense of obliquity (Fig. 8.2A).

Magnetic fabrics in the Whistle Offset differ in that they reveal an opposite sense of obliquity at the two vertical dyke margins. Such a case fits better with the interpretation of simple magmatic flow within a dyke (Fig. 8.2B). The differences in the data between the two Offset dykes illustrates that the different Offsets associated with the SIC may not have all formed in exactly the same manner. The further use of magnetic fabric studies on other Offset dykes may help to highlight some of the differences in their mechanisms of emplacement.

### *8.3. Model for emplacement of the massive sulfides*

The two emplacement models (Fig. 8.3) that are consistent with the data set are outlined in Fig. 8.1. Model 1 is essentially the same as the models proposed by Murphy and Spray (2002) for the Whistle Offset and the more general model proposed in Lightfoot et al. (2001). The leucocratic breccia magma is emplaced first horizontally along a fracture in the footwall, possibly during the excavation stage of cratering (Fig. 8.3A). Sublayer norite and massive sulfides accumulate at the base of the SIC as the impact melt sheet is differentiated. Some of the massive sulfides then founder and sink into the still unsolidified Offset dyke from the overlying melt sheet (Fig. 8.3B). The embayment structure is also filled by sublayer norite during the first mafic differentiation of the melt sheet. The overlying units then eroded to expose the Offset dyke and sulfide bodies at their current level.

In model 2, pockets of sulfide rich magma are injected laterally along with the host silicate magma, at a structural level higher than the present erosional surface (Fig. 8.3C).

**Figure 8.3.** Models for the emplacement of the Whistle Offset dyke. **(8.3A,B)** Emplacement model 1: leucocratic breccia injected, then sulfides and sublayer accumulate on the floor of the impact melt body, followed by sinking of the sulfides (and possibly sublayer as well) into the dyke. Open arrows denote injection into the dyke. **(8.3C,D)** Emplacement model 2: sulfide melts injected with leucocratic breccia magma (8.3A) and then sink to deeper levels in the dyke. 8.3A-D are simplified drawings modified from Fig. 8 in Murphy and Spray (2002). The sublayer norite is not shown in Figs. 8.3A-D.

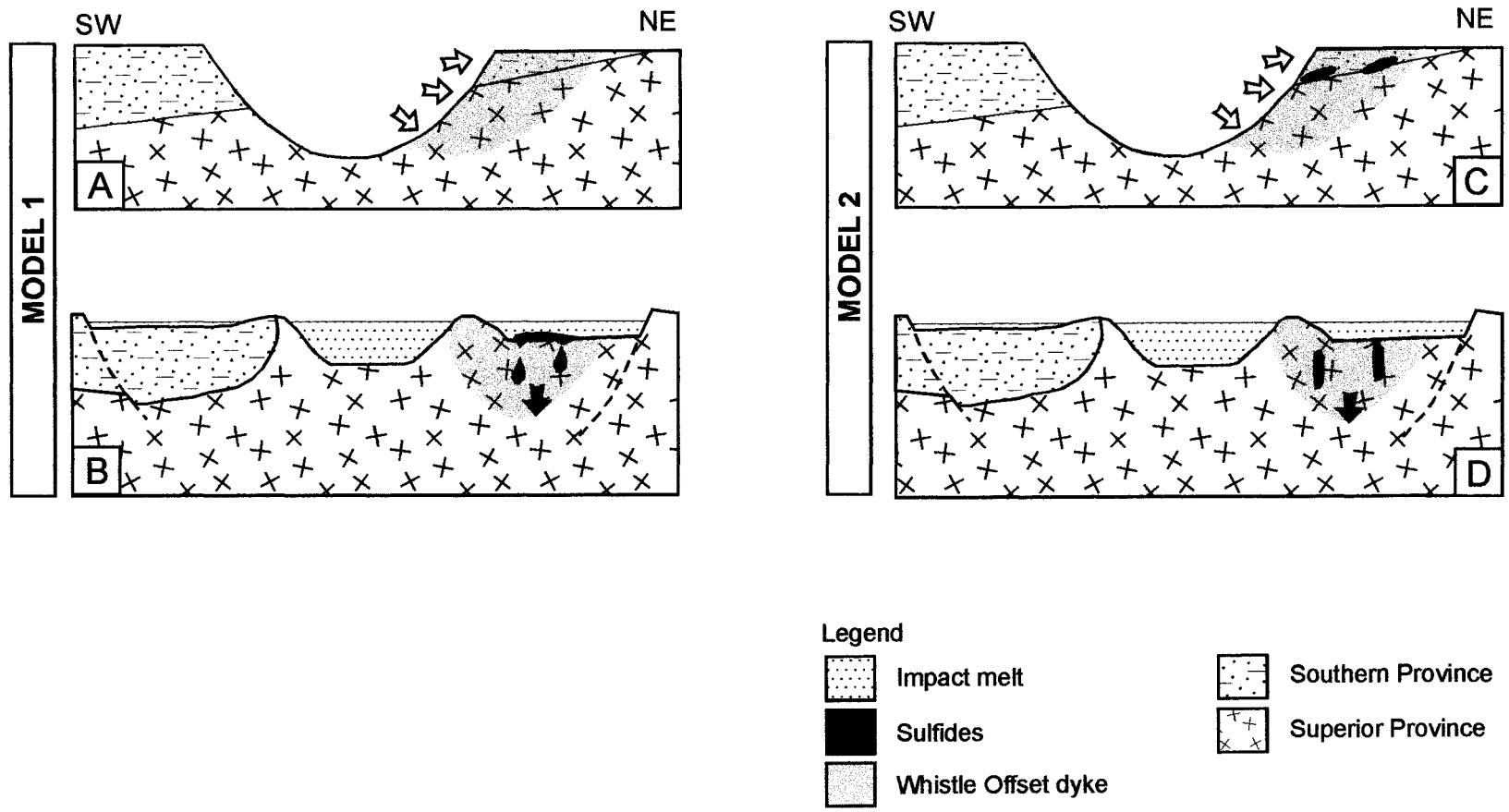
SW
NE
MODEL 1
A
B
SW
NE
MODEL 2
C
D
Legend
Impact melt
Sulfides
Whistle Offset dyke
Southern Province
Superior Province

Fig. 8.3.

Sulfides accumulate due to differential flow within the dyke. Subsequently, during cooling and crystallization of the Offset dyke, the massive sulfides sink through the sampled level (Fig. 8.3D) due to a density contrast with the less dense host silicate magma. The sinking of the sulfide bodies results in the steeply plunging lineations recorded for and around the massive sulfide bodies in the North Zone.

In both cases, the steeply plunging lineation within the exposed massive sulfide deposit and the magnetic fabrics within the rest of the Whistle Offset dyke suggest sinking of the sulfides into the unsolidified silicate magma.

## Chapter 9: Conclusions

The magnetic mineralogy and the magnetic anisotropy subfabrics were studied in detail for a 20-site sample suite from the Whistle Offset dyke and the Whistle embayment. Petrographic and SEM observations of the samples revealed a complex magnetic mineralogy, consisting of paramagnetic silicates and sulfides, and ferromagnetic minerals, of both magmatic and metamorphic origins. To investigate the differences in coercivities of the various mineral fractions of the samples, partial anhysteretic remanence (pAR) acquisition, anhysteretic remanence (AR) demagnetization, and thermal demagnetization were utilized. The anisotropies of magnetic susceptibility (AMS), anhysteretic remanence (AAR) and partial anhysteretic remanence (ApAR) of the samples were investigated to record the subfabrics defined by the difference coercivity fractions.

The results of the magnetic study revealed that the AMS of some samples is dominated by the soft coercivity, coarse grained primary (magmatic) magnetite crystals ± pyrrhotite and titanomagnetite. These *Type 1* sites include the massive sulfides, sulfide-rich breccias and the noritic rock types. All three magnetic anisotropy techniques (AMS, AAR and ApAR) record very similar fabrics for these sites. For other samples, both the AMS and the AAR also include a strong signal from hard coercivity minerals, including fine grained (metamorphic) magnetite and hematite. For these *Type 2* sites, which include all leucocratic breccia sites, the magnetic subfabric of the coarse-grained magnetite was successfully isolated using ApAR. *Type 2* samples containing a more significant coarse-grained magnetite fraction recorded similar subfabrics using both AMS and ApAR, as the soft coercivity coarse-grained magnetite swamped the signal from the harder coercivity fine-grained magnetite in the AMS.

The subfabrics controlled by coarse-grained magnetite are interpreted to be primary and therefore to record the kinematics of emplacement of the Offset dyke and the embayment. Evidence for the primary origin of the coarse-grained magnetite includes the presence of brecciated magnetite crystals in the massive sulfides and the rimming of the magnetites by different sulfide phases.

The primary magnetic subfabrics in the Whistle Offset reveal a counter-clockwise sense of obliquity of the near vertical magnetic foliation planes with respect to the vertical SE dyke margin. The obliquity between the magnetic foliation and the dyke margins is consistent with a dextral shear gradient in the magma flowing horizontally along the SE vertical dyke wall. A clockwise sense of obliquity of the magnetic foliations near the NW wall of the proximal Offset dyke is recorded at site WL11. Such an opposing sinistral shear gradient in the magma flow along the NW dyke margin fits with an interpretation of SW to NE injection of the magma into the non-deforming wallrocks. SW to NE emplacement flow is consistent with the generally accepted source of the Offset dyke material having been the SIC melt body. The foliation at site WL10 strikes parallel to the dyke wall and therefore it is also permissive in the case of SW to NE flow. The NE-SW striking magnetic foliations and N-NE trending horizontal magnetic lineations recorded for the majority of the sites within the proximal Offset are similar to the magnetic fabrics previously recorded in the North Lobe of the SIC.

Along with oblique magnetic foliations, horizontal lineations trending parallel to the length of the dyke are observed for the majority of the sites within the proximal Offset dyke, and are in agreement with the interpretation of horizontal injection of the magma into the dyke. At some sites, especially with the North Zone, near vertical lineations are recorded. In the North Zone, vertical lineations are most likely the result of the sinking of the massive

sulfide body. Vertical lineations that are not directly related to exposed sulfide bodies, such as those at sites WL13 and WL16 in the proximal Offset, may instead represent the foundering and sinking of sulfide bodies above or below the current level of exposure. Alternately the sinking of inclusion-free quartz diorite after the emplacement of the leucocratic breccia (as suggested in the Murphy and Spray model) may be responsible.

Fabrics in the cumulate sublayer norites in the Whistle embayment, which links the Offset dyke to the Sudbury Igneous Complex, are suggestive of steep walls and a shallowly dipping bottom to the funnel-shaped embayment. The fabrics indicate deposition in a dynamic environment that possibly involved gravity currents, thermal convection, or the slumping of cumulates on the floor and walls of the embayment.

Based on the magnetic fabric data, it is interpreted that the Whistle Offset was emplaced by a forceful lateral injection into a vertical radial fracture in the target rocks. Two possible models are consistent with the magnetic data. In the first emplacement model (Model 1) the leucocratic breccia magma was emplaced first, horizontally, along a vertical fracture in the footwall, possibly during the excavation stage of the impact cratering. Sublayer norite and massive sulfides then accumulated at the base of the SIC during the first mafic differentiation of the impact melt sheet. Some of the massive sulfides then foundered and sank into the still unsolidified Offset dyke from the overlying melt sheet. The sublayer norite also filled the embayment structure during the first mafic differentiation of the melt sheet. The overlying units then eroded to expose the Offset dyke and sulfide bodies at their current level.

In the second model (Model 2), pockets of sulfide rich magma were injected laterally along with the host silicate magma, at a structural level higher than the present erosional surface. Sulfides accumulated due to differential flow within the dyke and during subsequent

cooling and crystallization of the Offset dyke the massive sulfides sank through the sampled level due to a density contrast with the less dense host silicate magma. The sinking of the sulfide bodies resulted in the steeply plunging lineations recorded for and around the massive sulfide bodies in the North Zone.

In both cases, the magnetic fabrics in the Whistle Offset dyke suggest sinking of the sulfides into the silicate magma. The results suggest that further studies may reveal vertical lineations elsewhere in the Whistle Offset dyke, and in other Offset dykes of the Sudbury Impact Structure, and that these vertical fabrics may indicate the presence of sunken massive sulfides in the subsurface. The differences in the magnetic fabrics and suggested kinematics of emplacement between the Whistle and Copper Cliff Offset dykes illustrates that the different Offsets associated with the SIC may have somewhat different emplacement histories. The further use of magnetic fabric studies on other Offset dykes may help to highlight some of the differences in their mechanisms of emplacement.

**References**


Benn, K. and Allard, B., 1989, Preferred mineral orientations related to magmatic flow in ophiolite layered gabbros: Journal of Petrology, v. 30, p. 925-946.

Benn, K., Rochette, P., Bouchez, J.L., and Hattori, K., 1993, Magnetic susceptibility, magnetic mineralogy and magnetic fabrics in a late Archean granitoid-gneiss belt: Precambrian Research, v. 63, p. 59-81.

Boerner, D.E., Milkereit, B., Wu, J., and Salisbury, M., 2000, Seismic images and three-dimensional architecture of a Proterozoic shear zone in the Sudbury Structure (Superior Province, Canada): Tectonics, v.19, p. 397-405.

Borradaile, G. J. and Henry, B., 1997, Tectonic applications of magnetic susceptibility and its anisotropy: Earth-Science Reviews: v. 42, p. 49-93.

Borradaile, G.J. and Stupavsky, M., 1995, Anisotropy of magnetic susceptibility: measurement schemes: Geophysical Research Letters, v. 22, p. 1957-1960.

Butler, H. R., 1994, Lineament analysis of the Sudbury multiring impact structure, *in* Dressler, B.O., Grieve, R.A.F. and Sharpton, V.L., eds., Large Meteorite Impacts and Planetary Evolution, Special Paper 293: Boulder, Colorado, Geological Society of America, p. 319-329.

Coleman, A.P., 1903, The Sudbury nickel deposits: Report for 1902, Ontario Bureau of Mines, p. 235-303.

Cowan, E.J., 1999a, Magnetic fabric constraints on the initial geometry of the Sudbury Igneous Complex: a folded sheet or a basin-shaped igneous body?: Tectonophysics, v. 307, p. 135-162.

Cowan, E.J., Riller, U., and Schwerdtner, W.M., 1999b, Emplacement geometry of the Sudbury Igneous Complex: structural examination of a proposed impact melt sheet, *in* Dressler, B.O., Grieve, R.A.F. and Sharpton, V.L., eds., Meteorite impacts and planetary evolution II, Special Paper 339: Boulder, Colorado, Geological Society of America, p. 399-418.

Day, R., Fuller, M., and Schmidt, V.A., 1977, Hysteresis properties of titanomagnetites: grain-size and compositional dependence: Physics of the Earth and Planetary Interiors, v. 13, p. 260-267.

Deutsch, A., Grieve, R.A.F., Avermann, M., Bischoff, L., Brockmeyer, P., Buhl, D., Lakomy, R., Muller-Mohr, V., Ostermann, M., and Stoffler, D., 1995, The Sudbury structure (Ontario, Canada): a tectonically deformed multi-ring impact basin: Geologishe Rundschau, v. 84, p. 697-709.

Dietz, R. S., 1964, The Sudbury Structure as an astrobleme: Journal of Geology, v. 72, p. 412-434.

Dressler, B. O., 1984, The Effects of the Sudbury Event and the Intrusion of the Sudbury Igneous Complex on the Footwall Rocks of the Sudbury Structure, *in* Pye, E.G., Naldrett A.J., Giblin, P.E. eds., The Geology and Ore Deposits of the Sudbury Structure, Special Volume 1: Ontario, Canada, Ontario Geological Survey, p. 97-136.

Farrow, C.E.G., and Watkinson, D.H., 1997, Diversity of precious-metal mineralization in footwall Cu-Ni-PGE deposits, Sudbury, Ontario: implications for hydrothermal models of formation: The Canadian Mineralogist, v. 35, p. 817-839.

FNX, 2003, Norman Property, FNX Mining Company Inc. 2003.

French, B. M., 1967, Sudbury Structure, Ontario: some petrographic evidence for origin by meteorite impact: Science, v. 156, p. 1094-1098.

Giroux, L.A., and Benn, K., *In review*, Emplacement of the Whistle Offset dike and hosted sulfides, Sudbury Impact Structure, Ontario: magnetic anisotropy fabrics: Economic Geology

Grant, R. W. and Bite, A., 1984, Sudbury quartz diorite offset dikes, *in* Pye, E.G., Naldrett A.J., Giblin, P.E. eds., The Geology and Ore Deposits of the Sudbury Structure, Special Volume 1: Ontario, Canada, Ontario Geological Survey, p. 275-300.

Grieve, R.A.F., Stöffler, D., and Deutsch, A., 1991, The Sudbury Structure: Controversial or Misunderstood?: Journal of Geophysical Research, v. 96, p. 22753-22764.

Guy-Bray, J. G. and Geological Staff, 1966, Shatter cones at Sudbury: Journal of Geology, v. 74, p. 243-45.

Hrouda, F., 1982, Magnetic anisotropy of rocks and its application in geology and geophysics: Geophysical Surveys, v. 5, p. 37-82.

Hunt, C.P., Moskowitz, B.M., and Banerjee, S.K., 1995, Magnetic properties of rocks and minerals, *in* Ahrens, T.J. ed., A Handbook of Physical Constants, Vol. 3: Washington, DC, American Geophysical Union, p. 189-204.

Jackson, M., 1991, Anisotropy of magnetic remanence: A brief review of mineralogical sources, physical origins and geological applications: Pure and Applied Geophysics, v. 136, p. 1-28.

Jackson, M., Gruber, W., Marvin, J., and Banerjee, S.K., 1988, Partial anhysteretic remanence and its anisotropy: applications and grainsize-dependence: Geophysical Research Letters, v. 15, p. 440-443.

Jelinek, V., 1978, Statistical processing of anisotropy of magnetic susceptibility measured on groups of specimens: Studia Geophyzika et Geodetika, v. 22, p. 50-62.

Kretz, R., 1983, Symbols for rock-forming minerals: American Mineralogist, v. 68, p. 277-279.

Krogh, T.E., Davis, D.W., and Corfu, F., 1984, Precise U-Pb zircon and baddeleyite ages for the Sudbury area, *in* Pye, E.G., Naldrett A.J., Giblin, P.E. eds., The Geology and Ore Deposits of the Sudbury Structure, Special Volume 1: Ontario, Canada, Ontario Geological Survey, p. 431-448.

Lightfoot, P.C. and Farrow, C.E.G., 2002, Geology, Geochemistry, and Mineralogy of the Worthington Offset Dike: A Genetic Model for Offset Dike Mineralization in the Sudbury Igneous Complex: Economic Geology, v. 97, p. 1419-1446.

Lightfoot, P.C., Keays, R.R., and Doherty, W., 2001, Chemical evolution and origin of nickel sulfide mineralization in the Sudbury igneous complex, Ontario, Canada: Economic Geology, v. 96, p. 1855-1875.

Lightfoot, P.C., Keays, R.R., Morrison, G.G., Bite, A., and Farrel, K.P., 1997, Geologic and Geochemical Relationships between the Contact Sublayer, Inclusions, and the Main Mass of the Sudbury Igneous Complex: A Case Study of the Whistle Mine Embayment: Economic Geology, v. 92, p. 647-673.

Masaitis, V.L., Shafranovsky, G.I., Grieve, R., Langenhorst, F., Peredery, W.V., Therriault, A.M., Balmasov, E.L., and Federova, I.G., 2000, Impact diamonds in the Suevitic Breccias of the Black Member of the Onaping Formation, Sudbury Structure, Ontario, Canada, *in* Dressler, B.O., Grieve, R.A.F. and Sharpton, V.L., eds., Meteorite impacts and planetary evolution II, Special Paper 339: Boulder, Colorado, Geological Society of America, p. 317-321.

McCabe, C., Jackson, M., and Ellwood, B.B., 1985, Magnetic anisotropy in the Trenton limestone: results of a new technique, anisotropy of anhysteretic susceptibility: Geophysical Research Letters, v. 12, 333-336.

Melosh, H.J., 1989, Impact Cratering: A Geologic Process. New York, Oxford University Press.

Murphy, A.J. and Spray, J.G., 2002, Geology, Mineralization, and Emplacement of the Whistle-Parkin Offset Dike, Sudbury: Economic Geology, v. 97, p. 1399-1418.

Naldrett, A.J. and Hewins, R.H., 1984, The Main Mass of the Sudbury Igneous Complex, *in* Pye, E.G., Naldrett A.J., Giblin, P.E. eds., The Geology and Ore Deposits of the Sudbury Structure, Special Volume 1: Ontario, Canada, Ontario Geological Survey, p. 235-251.

Ostermann, M., Scharer, U., and Deutsch, A., 1996, Impact melt dikes in the Sudbury multi-ring basin (Canada): Implications from uranium-lead geochronology on the Foy Offset Dike: Meteoritics and Planetary Science, v. 31, p. 494-501.

Pattison, E.F., 1979, The Sudbury Sublayer: Canadian Mineralogist, v. 17, p. 257-274.

Pignotta, G.S. and Benn, K., 1999, Magnetic fabric of the Barrington Passage pluton, Meguma Terrane, Nova Scotia: a two-stage fabric history of syntectonic emplacement: Tectonophysics, v. 307, p. 75-92.

Pilkington, M. and Grieve, R., 1992, The geophysical signature of terrestrial impact craters: Reviews of Geophysics, v. 30, p. 161-181.

Rochette, P., Aubourg, C., and Perrin, M., 1999, Is this magnetic fabric normal? A review and case studies in volcanic formations: Tectonophysics, v. 307, 219-234.

Rochette, P., Jackson, M., and Aubourg, C., 1992, Rock magnetism and the interpretation of anisotropy of magnetic susceptibility: Reviews of Geophysics, v. 30, p. 209-226.

Rochette, P., Jenatton, L., Dupuy, C., Boudier, F., and Reuber, I., 1991, Diabase dikes emplacement in the Oman Ophiolite: a magnetic fabric study with reference to geochemistry: Ophiolite Genesis and Evolution of the Oceanic Lithosphere, T.E.A. Peters. Mascate, Ministry of Petroleum and Minerals, Sultanate of Oman, p. 55-82

Roest, W.R., and Pilkington, M., 1994, Restoring post-impact deformation at Sudbury: A circular argument: Geophysical Research Letters, v. 21, p. 959-962.

Scott, R.G. and Benn, K., 2001, Peak-rim collapse accommodated by impact melt-filled transfer faults, Sudbury Impact Structure, Canada: Geology, v. 29, p. 747-750.

Scott, R.G. and Benn, K., 2002, Emplacement of sulfide deposits in the Copper Cliff Offset Dike during collapse of the Sudbury crater rim: implications for the origin of sulfide-rich melts: Economic Geology, v. 97, p. 1447-1458.

Scott, R.G. and Spray, J.G., 1999, Magnetic fabric constraints on friction melt flow regimes and ore emplacement direction within the South Range Breccia Belt, Sudbury Impact Structure: Tectonophysics, v. 307, p. 163-189.

Spray, J.G., 1997, Superfaults: Geology, v. 25, p. 579-582.

Spray, J.G. and Thompson, L.M., 1995, Friction melt distribution in a multi-ring impact basin: Nature, v. 373, p. 130-132.

Stephenson, A., Sadikun, S., and Potter, D.K., 1986, A theoretical and experimental comparison of the anisotropies of magnetic susceptibility and remanence in rocks and minerals: Geophysical Journal of the Royal Astronomical Society, v. 84, p. 185-200.

Tarling, D.H., and Hrouda, F., 1993, The Magnetic Anisotropy of Rocks, Chapman & Hall, London, 217 p.

Therriault, A.M., Fowler, A.D., and Grieve, R.A.F., 2002, The Sudbury Igneous Complex: A Differentiated Impact Melt Sheet: Economic Geology, v. 97, p. 1521-1540.

Thompson, L.M. and Spray, J.G., 1996, Pseudotachylyte petrogenesis: contraints from the Sudbury impact structure: Contributions to Mineralogy and Petrology, v. 125, p. 359-374.

Thompson, R., 1935, The 'Offset Dykes' of the Nickel Intrusive, Sudbury, Ontario: American Journal of Science, v. 30, p. 356-367.

Trinidade, R.I.F., Bouchez, J.L., Bolle, O., Nédélec, A., Peschler, A., and Poitrasson, F., 2001, Secondary fabrics revealed by remanence anisotropy: methodological study and examples from plutonic rocks: Geophysical Journal International, v. 147, p. 310-318.

Uyeda, S., Fuller, M.D., Belshé, J.C., and Girdler, R.W., 1963, Anisotropy of magnetic susceptibility of rocks and minerals: Journal of Geophysical Research, v. 68, p. 279-290.

Wood, C.R. and Spray, J.G., 1998, Origin and emplacement of Offset Dykes in the Sudbury impact structure: Constraints from Hess: Meteoritics and Planetary Science, v. 33, p. 337-347.